UNIVERSITY OF OKLAHOMA

GRADUATE COLLEGE

# HIGH-PRECISION MEASUREMENTS OF ALKANETHIOL SELF-ASSEMBLED MONOLAYER STRUCTURE WITH SCANNING TUNNELING MICROSCOPY

A DISSERTATION

SUBMITTED TO THE GRADUATE FACULTY

in partial fulfillment of the requirements for the

Degree of

DOCTOR OF PHILOSOPHY

By

MITCHELL P. YOTHERS
Norman, Oklahoma
2020

HIGH-PRECISION MEASUREMENTS OF ALKANETHIOL SELF-ASSEMBLED

MONOLAYER STRUCTURE WITH SCANNING TUNNELING MICROSCOPY

A DISSERTATION APPROVED FOR THE
HOMER L. DODGE DEPARTMENT OF PHYSICS AND ASTRONOMY

BY THE COMMITTEE CONSISTING OF

Dr. Lloyd A. Bumm, Chair

Dr. Daniel T. Glatzhofer

Dr. Liangliang Huang

Dr. Michael B. Santos

Dr. Ian R. Sellers

© Copyright by MITCHELL P. YOTHERS 2020

All Rights Reserved.

# Abstract

This thesis describes a measurement methodology and set of tools for measuring scanning tunneling microscope images of crystals at picometer length scales. We use the crystal structure present in high-quality scanning tunneling microscope images as an internal standard to measure distortion caused by thermal drift of the scanning tunneling microscope tip and piezoelectric actuator nonlinearities introduced during the scan. Using a model for these sources of distortion, we calculate an inverse distortion transform and apply it to the image. By taking advantage of spatial and temporal averaging of corrected images, we can make high-precision measurements of the surface structure and its aggregate noise. We applied this technique to images of graphite and alkanethiol self-assembled monolayers on Au(111). Our measurements of graphite were consistent with our expectations, with noise level as low as ±3.5 pm. Preliminary results for alkanethiol self-assembled monolayers show measurements of their tilt direction and twist structure, confirmation of the 4-molecule-basis lattice, and a strong dependence of image results on the condition of the probe tip.

# Acknowledgements

Thanks to all members of the Bumm group, especially my advisor Dr. Lloyd Bumm and my colleague Soumya Bhattacharya, for the constant advice and support from group meetings.

Thanks to all the members of the Sykes group from Tufts university, especially Dr. Charlie Sykes, Dr. Amanda Larson, Tedros Balema, and Dipna Patel, for access to their LT-STM and their help with operating it. Thanks to Dr. Liangliang Huang and Guobing Zhou for their discussions about SAMs and their collaboration on the NSF project. Thanks to all the people who have helped me operate the STM or analyze STM images over the years I've been running it, including Ryan Hood, Nafisa Amin, Muzzakir Amin, Rob Conwell, Juan Zuñiga, Seth Miller, Ian Timms, Julia Rusert, Bryan Boone, and Elizabeth Moffatt. Special thanks to Cody Ray for designing the sample vial we use to make alkanethiol SAMs, and to Aaron Browder for his preliminary work on the distortion correction project. Thanks to the rest of my committee, Dr. Daniel Glatzhofer, Dr. Michael Santos and Dr. Ian Sellers, for pushing me to be better and not allowing me to settle for good enough.

Thanks to NVIDIA, The Homer L. Dodge Department of Physics and Astronomy, The Carl T. Bush Fellowship, OU's College of Arts and Sciences, and the National Science Foundation for their funding supporting my research.

Thanks to my family, especially my parents Robbin and Greg Yothers and my sister Emily Yothers, for supporting me throughout my education.

I would not have made it to where I am today without the help of everyone listed here.

# Table of Contents

Abstract ..... iv
Acknowledgements ..... v
Table of Contents ..... vi
1. Introduction and Motivation ..... 1
1.1. DHCT Description ..... 2
1.2. In-Plane Image Analysis Tools ..... 3
1.3. Height Analysis Tools and Results ..... 4
1.4. Structure and Noise Measurements ..... 5
1.5. References ..... 7
2. Materials and Methods ..... 8
2.1. Scanning Tunneling Microscope ..... 8
2.2. Alkanethiol SAM Structure ..... 11
2.3. Sample Preparation ..... 14
2.4. References ..... 17
3. DHCT Description ..... 18
3.1. Raster Scan Description ..... 19
3.2. Time-independent Image Transformations ..... 24
3.2.1. Stretch ..... 25
3.2.2. Shear ..... 26
3.2.3. Tilt ..... 27
3.3. Mechanisms of Distortion in STM ..... 27
3.3.1. Thermal Drift ..... 28
3.3.2. Piezoelectric Actuator Hysteresis ..... 29
3.2.3. Piezoelectric Actuator Creep ..... 31
3.4. Internal Standard and Region Masks ..... 31
3.5. Measuring Linear Distortion ..... 32
3.6. Measuring Local Distortion ..... 33
3.7. Technique ..... 34
3.7.1. Pre-processing ..... 34
3.7.2. Initialization ..... 36
3.7.3. Feature Indexing ..... 37
3.7.4. Time Assignment ..... 38
3.7.5. Finding Nearest Neighbors ..... 39

3.7.6. Determining Local Distortion ..... 40
3.7.7. Determining Distortion Trends ..... 42
3.7.8. Applying Image Correction ..... 44
3.7.9. Expanding to Different Surface Lattice Structures ..... 45
3.8. Data Structure Description ..... 46
3.9. References ..... 51
4. In-Plane Image Analysis Tools ..... 53
4.1 DHCT Second Pass for Alkanethiols ..... 53
4.2. Lattice Fitting ..... 54
4.2. Averaged Unit Cell Images ..... 58
4.4. Feature Confidence Ellipsoids ..... 60
4.5. Symmetry-Averaged Unit Cell Images ..... 60
4.6. Time Series Lattice Alignment ..... 61
4.7. Data Visualization – 2D Correlation Plots ..... 63
4.8. Data Visualization – Reduced Close-Packed Coordinate Frame ..... 64
4.9. References ..... 69
5. Height Analysis: Tools and Results ..... 70
5.1. Height Measurement Methodology ..... 71
5.2. Height Measurement Results ..... 73
5.3. STM Image Simulation Model ..... 74
5.4. References ..... 80
6. Structure and Noise Measurements ..... 81
6.1. Noise in STM images ..... 81
6.2. STM Imaging Artifacts ..... 84
6.3. Graphite Noise Measurement ..... 85
6.4. Alkanethiol SAM Structure and Noise Measurements ..... 87
6.4.1 Single Images ..... 88
6.4.2. Multiple Similar Images ..... 92
6.4.3. Comparing Different Images ..... 95
6.5. Measuring Internal SAM Structure ..... 98
6.6. Conclusions ..... 103
6.7. References ..... 104
Appendix A: STM Image Analysis User Manual ..... 106
A.1. How to Use this Manual ..... 106
A.1.1. Finding the Scripts ..... 107
A.1.2. Script Hierarchy ..... 107

A.1.3. Script Workflow ..... 109
A.2. Setup ..... 110
A.2.1. Setup Requirements ..... 110
A.2.2. Setup Walkthrough ..... 111
A.3. DHCT and DHCT Multiple Passes ..... 118
A.4. Lattice Fitting and Polynomial Lattice Corrections ..... 119
A.5. Generating Plots: Averaged Unit Cell and Location Confidence ..... 122
A.6. Other Plot Generation Scripts ..... 126
A.6.1. Reduced Close Packed Coordinate Frame Analysis ..... 126
A.6.2. Aligned Image Set Movie ..... 127
A.6.3. 2D Correlation Plots ..... 128
A.6.4. Guest Molecule Analysis ..... 129
A.7. Two-Junction Tunneling Model ..... 130

# Chapter 1
# Introduction and Motivation

Scanning tunneling microscopy (STM) has been an important tool for measuring surface structure for nearly forty years.[1] In STM, a sharp, conductive probe is brought very close (approx. 1 nm) to a flat, conductive sample. The distance between the tip and the sample can be precisely measured by taking advantage of quantum tunneling of electrons. The probability of electron tunneling, and the directly related tunneling current, depend exponentially on the separation distance between the tip and the sample. Measuring the tunneling current quickly and accurately probes the height of the tip above the sample. By precisely controlling the tip using this height measurement, we can prevent surface contact and measure the surface underneath. At typical operating conditions, individual atoms can be routinely resolved with STM.[2, 3] The ability to resolve individual atoms has made the STM one of the most important tools for measurement at the nanoscale. It has been used to measure crystal structures,[4, 5] molecule structures,[6] and even manipulate single atoms.[7, 8]

Images taken by cameras have become commonplace ever since the development of photographic film over 130 years ago. Cameras use a system of lenses to focus an image at a different location, allowing it to be observed or recorded more conveniently. Typical cameras, light microscopes, and human eyes use light for this purpose, and the transmission electron microscope works with electrons using the same principle. Interpreting camera images is so culturally important that relevant skills (e.g. perspective) are taught in art classes rather than science classes. Camera images of objects look almost identical to the source object, with exceptions for some common-sense omissions, such as depth. Images produced by scanning probe microscopes like the STM differ in a few ways. Scanning probe images are not acquired all at

once, instead they are acquired one point at a time by the probe. In order to see a scanning probe microscope image, it must be reconstructed from the probe measurements. Images from color cameras display the luminance of red, blue and green light at each point to create a colored image. Even though scanning probe microscopes also acquire multiple data channels, their images are usually displayed one channel at a time with a monochromatic image. For the scanning tunneling microscope, topography is one of the most common data channels. In a topographic image, the brightness of each pixel represents the height of the probe tip. This is a small list of changes—it's easy to be convinced that interpreting scanning probe microscope images is simple and jump to the wrong conclusions. When analyzing STM images, it's best to keep these changes in mind and proceed cautiously with interpretation.

In this thesis, I will explain the work my group is doing to make precise measurements from scanning tunneling microscope images. Chapter 2, Materials and Methods, will discuss how our lab's scanning tunneling microscope works, standard praxis for analyzing STM images, the substrates we imaged with the microscope, and how we prepared those substrates. The other 4 chapters will describe our research progress so far.

### 1.1. DHCT Description

Chapter 3 is a full description of the DHCT software package, an image post-processing tool that reconstructs STM images of 2D crystals while registering their image features. An obvious application of the STM is to use it to make measurements of the surface it's imaging. STM images usually have a small but noticeable amount of distortion that makes measurements of them differ from what those measurements would be if they were made on the surface instead of the image. This is caused by slight differences in the position of the probe tip compared to the expected path during the scan. The differences accumulate over the image acquisition time, causing the

image to appear distorted. Since each pixel is still an accurate measurement of the place it recorded, we can remove the distortion by plotting the same pixels in a way that more accurately represents the true scan trajectory. This removes the distortion and makes image measurements comparable to surface measurements.

We start by describing the ways an image can be distorted, through stretch, shear and tilt. Next, we identify the sources of the distortion—thermal drift and piezoelectric actuator nonlinearities. We discuss the kinds of distortion they cause. We then describe how to use the lattice that is being imaged as an internal standard to determine the distortion at certain points in the image. Then, by calculating the distortion at many different points, we can find the trend of the distortion with time, which we can use to correct the coordinates of each pixel in the image. Finally, we describe the software implementation of this tool in Matlab, which is available for free under a public license on GitHub.

### 1.2. In-Plane Image Analysis Tools

Chapter 4 describes image analysis tools we developed that rely on DHCT. Distortion-corrected images of crystals should have their lattices restored. One of these tools takes DHCT-corrected images and calculates the best-fit lattice to the image feature locations. The best-fit lattice lets us assign lattice sites to image features, improve the image correction by including longer-range measurements of distortion, and apply techniques designed for studying lattices to our image data. Spatial averaging over the lattice vectors is one such technique, which we can apply to the image to generate average unit cell images or to the feature locations to generate feature location confidence ellipsoids. Symmetry averaging is a more in-depth application of spatial averaging that can be applied to symmetric unit cells, which we also demonstrate.

By taking multiple images of the same area, we can image the same features in multiple images in a row. By fitting a lattice to each image and aligning the lattices, we obtain an aligned image sequence. The aligned image sequence can be used to observe single image features evolve over time, or to time-average image data for increased signal-to-noise ratio. We also show some data visualizations. The alkanethiol surface that we commonly take images of has a surface unit cell that contains four molecules with the same chemical composition, with only slight differences in each molecule's orientation. Since the 4 molecules are quite similar, our visualizations amplify the differences between them. These visualizations help us to consider the differences between data sets, rather than the similarities that are much easier to see.

### 1.3. Height Analysis Tools and Results

Chapter 5 contains our progress so far towards making height measurements of STM images and understanding the measurements we make. Height measurements in STM images are typically extracted from a path drawn through the image, in a process known as an image cross-section. By using the averaged unit cells and feature locations from Chapters 3 and 4, we can generate height measurements that are similar in concept to the image cross section, but contain data sampled from the whole image rather than just a straight line. We show our measurement results, which include some images with much higher image corrugation than we expected. Image corrugation is the difference in height between the highest point of the unit cell and the lowest point.

We developed a model that allows us to generate simulated STM images of alkanethiol self-assembled monolayers (SAMs), based on what we know about the way the STM works and how electrons are transferred through the monolayer. We simulate the tunneling process that the STM would do for a given structure, but with full control of the structure and scan parameters. We

are investigating the model to try to understand the anomalous height measurement we observed. We hope to better understand how changes in scan parameters affect STM images to determine how reliable different measurements are.

### 1.4. Structure and Noise Measurements

Chapter 6 describes our progress on measuring structure and noise from STM images. One way we investigated the noise level of our microscope and technique was by measuring highly oriented pyrolytic graphite (HOPG) as precisely as possible. Graphite's structure is well-understood, so we can quite reliably predict that the motion of the C atoms in the graphite lattice will introduce a negligible amount of noise in our measurement of their position. By using graphite as a reference, we can determine the noise level of our measurement. We are currently attempting to uncover the unit cell structure at the surface of alkanethiol self-assembled monolayers (SAMs). Our goal is to accurately measure the basis of the surface unit cell, or each of the surface unit cells if there is more than one. This would help to solve some long-standing questions about SAMs, such as whether or not the surfaces of odd and even length SAMs are different. It would be helpful as a reference to better predict how changes to the SAM surface could modify it in useful ways. It could also be used to constrain models of the entire SAM, which can be used in simulations to determine how the SAM bonds to the surface.

We also developed an experiment that allows us to measure the twist and tilt direction of alkyl chains in an alkanethiol SAM by making measurements of the surface with STM. We do this by creating alkanethiol SAMs that are composed of two different alkanethiol chain lengths, called bi-component SAMs. The longer chains emerge from the surface created by the shorter chains. If the guest molecules in the SAM are not much longer than the host, they maintain their orientation while embedded in the SAM. By measuring the longer chains, we also get information about their

orientation in addition to their location on the surface. With two alkanethiols that differ by an even amount of carbon atoms, we can measure the tilt direction. With two alkanethiols that differ by an odd amount of carbon atoms, we uncover some information about the twist of each molecule.

### 1.5. References

1. G. Binnig and H. Rohrer, Surf. Sci. **126** (1), 236-244 (1983).
2. R. M. Feenstra, J. Vac. Sci. Technol. B **7** (4), 925-930 (1989).
3. B. Drake, R. Sonnenfeld, J. Schneir, P. K. Hansma, G. Slough and R. V. Coleman, Rev. Sci. Instrum. **57** (3), 441-445 (1986).
4. M. J. Lawler, K. Fujita, J. Lee, A. R. Schmidt, Y. Kohsaka, C. K. Kim, H. Eisaki, S. Uchida, J. C. Davis, J. P. Sethna and E. A. Kim, Nature **466** (7304), 347-351 (2010).
5. I. Zeljkovic, E. J. Main, T. L. Williams, M. C. Boyer, K. Chatterjee, W. D. Wise, Y. Yin, M. Zech, A. Pivonka, T. Kondo, T. Takeuchi, H. Ikuta, J. Wen, Z. Xu, G. D. Gu, E. W. Hudson and J. E. Hoffman, Nat. Mater. **11** (7), 585-589 (2012).
6. J. F. Jorgensen, L. L. Madsen, J. Garnaes, K. Carneiro and K. Schaumburg, J. Vac. Sci. Technol. B **12** (3), 1698-1701 (1994).
7. S. Tewari, K. M. Bastiaans, M. P. Allan and J. M. van Ruitenbeek, Beilstein J. Nanotechnol. **8**, 2389-2395 (2017).
8. J. A. Stroscio and D. M. Eigler, Science **254** (5036), 1319-1326 (1991).

# Chapter 2
# Materials and Methods

This section describes the two scanning tunneling microscopes used to acquire images shown in this work, an in-depth description of what is known about alkanethiol SAM structure, and preparation details about our alkanethiol SAM and HOPG samples.

## 2.1. Scanning Tunneling Microscope

The ambient pressure, room-temperature STM images used in this research were acquired using our lab's beetle-style STM. The scan controller is an SPM100 from RHK Technology, with tunneling current measured using an Axon CV4 current amplifier. XPM Pro software, also from RHK Technology, is used to monitor and modify the scan during acquisition and save the scan results. STM imaging is performed in dry $N_2$ at room temperature. The tip for our STM is a piece of mechanically cut 80/20 wt% Pt-Ir wire. Low temperature ultra-high vacuum (UHV) images were taken in collaboration with the Sykes group at Tufts. These images were acquired with a low-temperature Omicron NanoTechnology STM, using an etched W tip, in an ultrahigh vacuum (UHV) chamber with a base pressure of $< 1 \times 10^{-10}$ mbar. Images were taken at 77 K and 4 K using liquid $N_2$ and liquid He for cooling, respectively.

A schematic diagram of a typical STM can be found in Figure 2.1. The position of the STM probe tip is controlled by a piezoelectric tube scanner.[1] A DC bias voltage is put between the tip and the sample, and the tip is slowly approached towards the sample until a tunneling current is measured. Both positive and negative sample biases can be used. Positive sample biases cause electrons to tunnel from the tip to the sample, and negative sample biases cause electrons to tunnel from the sample to the tip. The STM controller uses the tunneling current measurement to drive a

negative feedback loop controlling the tip position. This keeps the tip in tunneling range without contacting the sample. In the constant-current mode that we use for the images in this work, a user-defined setpoint current is chosen, and the STM feedback loop uses the difference between the measured and setpoint currents to control the height of the tip. If the measured current is too low, then the tip will move forward; if it's too high, the tip will move back. This causes the STM tip to quickly reach the position where the measured and setpoint currents are equal and stay there. Once the feedback loop is established and set to run continuously, the tip height will automatically react to changes in the surface underneath it. STM image data is acquired by measuring the tip height as we move the tip over the surface with feedback engaged.

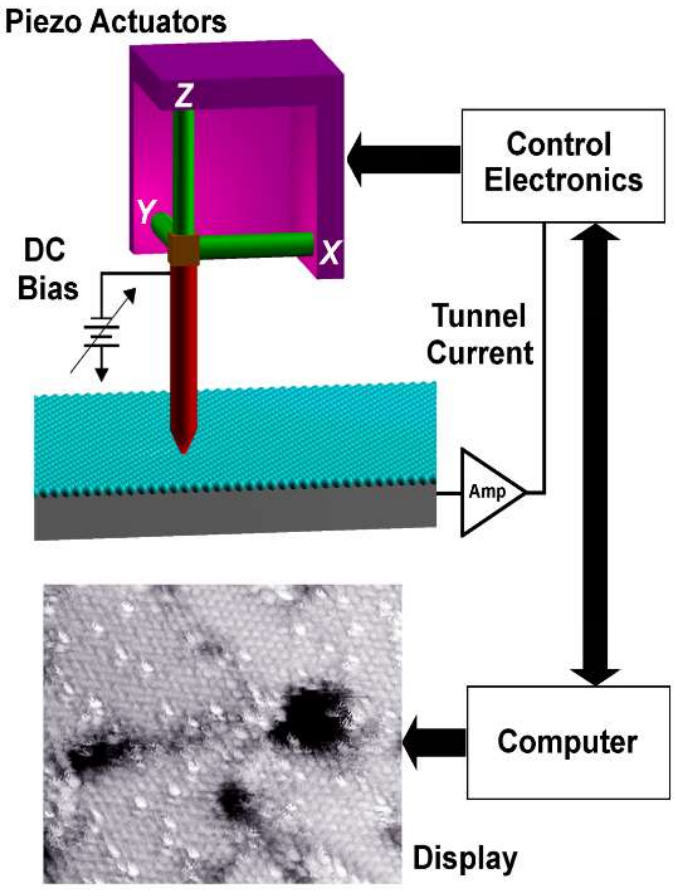


**FIG. 2.1.** A schematic diagram of a typical STM. The tip, sample, and STM controller are also represented.

We attempt to isolate our STM from external sources of noise. While scanning, our STM is placed on a passively damped massive platform which is isolated from the floor vibrations using a set of 3 air springs. The mass-spring system was chosen to attenuate ground vibrations above 2 Hz. The platform is in the basement in the back corner of Nielsen Hall. The location was chosen because it minimizes the ground vibrations caused by the motion of the building and nearby foot

traffic. The platform is contained within a medium density fiberboard box, approximately cubic with side length 48 inches. The box is lined with a double layer of lead sheet to create a Faraday cage for isolation from electromagnetic noise. The lead sheet is embedded in a several-cm-thick layer of acoustic foam to attenuate acoustic noise in the room. The box's access door is clamped tightly shut during operation. A slow feed of dry $N_2$ flows into the box to control for temperature and humidity while scanning. These measures greatly reduce the noise from external sources, such

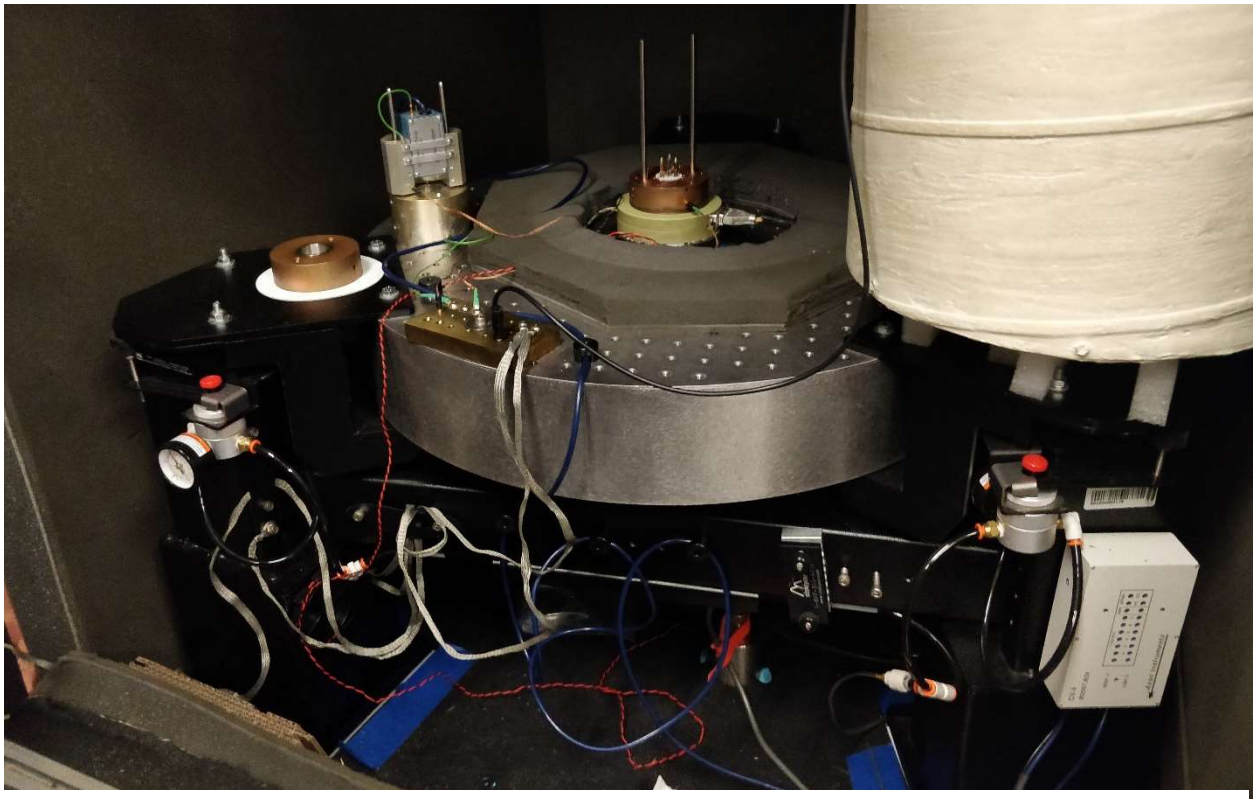

**FIG. 2.2.** A picture of our STM and isolation system. The STM (copper cylinder on green plastic base) is on a platform isolated from the ground with some pressurized air springs on its legs (left and right, the pressure gauges are part of this system). There is acoustic foam to dampen air vibrations as much as possible (Seen on the left wall and around the STM on the platform). Embedded in the foam on the walls are two layers of lead sheet to isolate from EM noise (can be seen bottom left). During operation, the STM would be engaged with the sample holder (Copper cylinder to the left) and the amplifier contact (the gray apparatus with the wires attached to it on the grounded platform to the left). The grounded white cylinder (right) would be covering the STM and resting on the acoustic foam on the platform to provide additional acoustic and electromagnetic isolation, and the door to the particle board box would be clamped shut.

as passing trains, talking in the lab, and electromagnetic interference. A picture of our STM and isolation setup can be seen in Figure 2.2.

### 2.2. Alkanethiol SAM Structure

Self-assembled monolayers are a spontaneously forming two-dimensional crystal that are frequently studied due to their reproducibility and ease of production. For alkanethiol SAMs on Au(111), the thiol headgroup bonds with the clean Au(111) surface. During this process, the S-H bond of the thiol is broken, the herringbone reconstruction from the gold surface is lifted, and gold atoms from the surface are incorporated into the monolayer structure.[2] At sub-monolayer coverages during the formation process, alkanethiols on the Au(111) surface form a two-dimensional liquid state characterized by surface mobility and disorder when compared to the monolayer structure.[3] The long alkane backbones crystallize with each other at higher surface densities, reaching an equilibrium where van der Waals interactions between the chains and maximal surface coverage of S-Au bonding are optimized. The ordered alkane backbones prevent additional molecules from bonding to the surface, keeping a well-ordered, one molecule thick, two-dimensional structure. When prepared using the conventional room temperature solution growth method, the size of the SAM crystallites usually ranges from 10-100 $nm^2$. The SAM overlayer has a larger surface unit cell and reduced rotational symmetry when compared to the underlying Au(111) surface. Two SAM crystal domains that are rotated from each other, or offset by a fraction of a SAM unit cell vector, can both be commensurate with the Au(111) surface. If these domains grow together but are large enough to maintain their registration with the Au surface, they form domain boundaries where they contact. STM images on SAMs prepared with the solution growth method show Au vacancy islands. Vacancy islands are the features that result when Au surface vacancies caused by the SAM growth process coalesce into visible single-atom-

deep, several-nm-wide holes in the surface. Our lab has developed a high-temperature vapor phase growth technique that minimizes vacancy islands and domain boundaries observed in SAMs, similar to other vapor phase growth techniques.[4] Our technique results in observed SAM crystallites as large as $10^4$ nm$^2$. At higher temperatures, the Au vacancies coalesce into much larger islands or migrate to gold atomic steps, significantly reducing or eliminating the occurrence of visible vacancy islands.

Despite the ease of making alkanethiol SAMs, they have proven quite difficult to fully characterize. A schematic model of a decanethiol self-assembled monolayer is shown in Figure 2.3. The exact nature of the bonding sites of the thiol headgroup to the Au(111) surface is still unknown despite many years of study.[5] Alkanethiol SAMs are known to incorporate gold adatoms into their structure.[6] One of the more promising structures for incorporating the gold adatom into the SAM structure is the RS-Au-SR structure, commonly known as the staple motif.[7] Bonding of sulfur to gold in methanethiol SAMs has been directly imaged,[8] but the surface unit cell changes for long-chain alkanethiols.[5] The alkanethiol chain prevents direct imaging of the Au-S interface with STM. Lattice vectors of high-coverage phases of long-chain alkanethiol SAMs have been measured with XRD, STM, and low-energy atom diffraction (LEAD). These measurements predict surface unit cell lattice vectors consistent with a $(2\sqrt{3} \times 3)$rect. unit cell, though it is very close to a $(\sqrt{3} \times \sqrt{3})R30°$ structure.[9-12] Both structures have exactly one alkanethiol molecule per three Au surface atoms. The $(2\sqrt{3} \times 3)$rect. structure is occasionally referred to as c(4 × 2) in the literature.

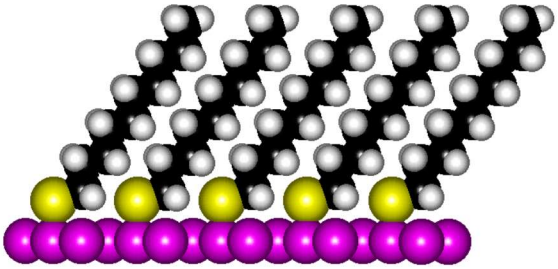

**FIG. 2.3.** 1-decanethiol self-assembled monolayer schematic diagram. The headgroup sulfur atoms (shown in yellow) bond to the Au(111) surface (purple). The alkane backbone (carbon in black, hydrogen white) tilts at 30° to the surface normal to optimize packing, which prevents more than one layer from forming.

The $(2\sqrt{3} \times 3)$rect. structure suggests a surface unit cell with a 4-molecule-basis lattice, where the surface bonding or configuration of the molecules in some way differentiates the molecules from each other, as compared with the $(\sqrt{3} \times \sqrt{3})R30°$ structure's 1-molecule-basis lattice. Of the techniques that have been used to measure the surface unit cell, only STM has been used to directly image individual alkanethiol terminal groups. Many structures with slightly differing appearances that share the $(2\sqrt{3} \times 3)$rect. lattice structure have been identified.[4, 12, 13] While visually distinct cells have been labeled as different structures in the literature, none of these structures have been rigorously measured. It is currently unknown whether the phases in the literature are fundamentally different from each other. Different appearances could be explained by variability in the STM tip, or a structure with multiple states that it is able to transition between. Though unlikely, it is also possible that many similar-energy structures on the surface coexist and appear quite similar in STM images. We cannot rule out any of these possibilities.

A schematic diagram showing definitions for the tilt and twist angles and tilt direction of alkanethiol molecules in a monolayer is shown in Figure 2.4. The tilt angle is the angle between the surface normal and the molecular axis (the line containing the midpoints of all of the C-C bonds). The twist angle is measured perpendicular to the molecular axis. It is the angle between the tilt plane (the plane containing the molecular backbone and the surface normal) and the molecular plane (the plane containing all of the C atoms). The tilt direction is measured in the plane of the surface as

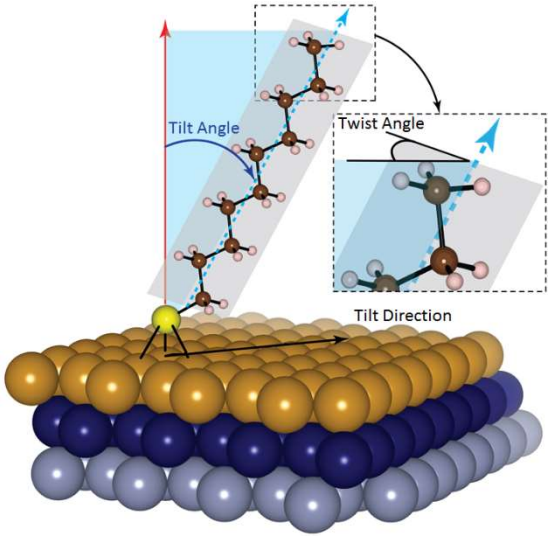


**FIG. 2.4.** 1-decanethiol molecule diagram showing definitions for tilt angle, twist angle and tilt direction.

the angle between the tilt plane and Au[110], one of the Au nearest neighbor directions. Long-chain alkanethiol SAMs are known to tilt with tilt angle of about 30° with respect to the surface normal, as measured by infrared spectroscopy.[14] Alkanethiol SAM surfaces are composed of alkanethiols with all-trans backbones that are contained within one of two orthogonal planes, also measured by infrared spectroscopy.[15] There are up to 4 twist angles that are consistent with this measurement. Each molecular plane describes two twists that differ from each other by a 180° rotation. This measurement is an ensemble over the whole surface, it is not yet known how many unique twists the surface unit cell contains, or the configuration of those twists. All molecules tilt along the tilt direction on the surface and maintain an all-trans configuration. How the tilt direction compares with the surface lattice vectors is not known with certainty.

### 2.3. Sample Preparation

Our alkanethiol samples were prepared in a stainless steel sample vial designed to minimize oxidation of the alkanethiols. Photos of the sample vial can be seen in Figure 2.5. A stainless steel body with a copper gasket was chosen to eliminate permeation of oxygen into the vial. To minimize oxidation on the stainless steel surface, the surface was passivated with SilcoNert® 2000 silicon oxynitride coating. The vial was designed in conjunction with a $N_2$ purging system so that the vial could be sealed under a $N_2$ purge.

Images in this work were taken on two kinds of substrates: self-assembled monolayers (SAMs) of long-chain alkanethiols on Au(111) and highly-oriented pyrolytic graphite (HOPG). Au(111) substrates deposited on mica obtained from Agilent Technologies were reused from previous experiments by hydrogen flame annealing.[16] After flame annealing, the sample was put into a small test tube located in one well of our sample vial. Another well was filled with a set of two nested test tubes. The inner nested test tube was filled with 2-5 μL of alkanethiol. The sample

**FIG. 2.5.** Photograph of our stainless steel sample vial designed for high-temperature vapor deposition of alkanethiol SAMs. (left) Inside of the sample vial, showing the copper gasket, wells for the sample and alkanethiol, and the silicon oxynitride coating. (right) The sample vial, with the lid partially engaged Dry $N_2$ comes in through a hole in the metallic base, through the vent holes in the bottom of the sample vial, into the center of the vial, before flowing out through some vent holes in the lid. Not shown is the baffle that engages with the o-ring on the base.

vial was purged with dry $N_2$ for 5-10 minutes before sealing it with a fresh copper gasket. The sealed vial was heated in an oven at 100-120 °C for 4-16 hours, then removed and allowed to cool to room temperature. The sample was then rinsed with toluene, then ethanol, and blown dry with $N_2$. The SAMs were imaged with the STM in constant current mode. The alkanethiol monolayers studied here were made with 1-decanethiol (called C10 for short due to having 10 carbons), 1-undecanethiol (C11) or 1-dodecanethiol (C12), and bi-component SAMs were made with two of these alkanethiols. 1-Decanethiol 99%, 1-undecanethiol 95%, and 1-dodecanethiol 95% were obtained from Sigma-Aldrich and used without further purification. For bi-component SAMs, a mixture of alkanethiols was calculated for our sample vial such that the equilibrium vapor pressure at the oven's temperature of both components resulted in a 5% mole fraction of longer-chain guests in the vapor phase.

Our sample of HOPG was a ZYB-grade sample obtained from NT-MDT. The graphite was imaged at −60 mV sample bias and 160 pA tunneling current in constant current mode. Before

imaging, the sample was freshly cleaved to expose a pristine surface by carefully removing layers from the top of the graphite with scotch tape.

### 2.4. References

1. C. J. Chen, Appl. Phys. Lett. **60** (1), 132-134 (1992).
2. N. A. Kautz and S. A. Kandel, J. Phys. Chem. C **113** (44), 19286-19291 (2009).
3. W. P. Fitts, J. M. White and G. E. Poirier, Langmuir **18** (6), 2096-2102 (2002).
4. B. Lussem, L. Muller-Meskamp, S. Karthauser and R. Waser, Langmuir **21** (12), 5256-5258 (2005).
5. Q. Guo and F. Li, Phys. Chem. Chem. Phys. **16** (36), 19074-19090 (2014).
6. N. A. Kautz and S. A. Kandel, J. Am. Chem. Soc. **130** (22), 6908-6909 (2008).
7. V. Rojas-Cervellera, E. Giralt and C. Rovira, Inorg. Chem. **51** (21), 11422-11429 (2012).
8. O. Voznyy, J. J. Dubowski, J. T. Yates and P. Maksymovych, J. Am. Chem. Soc. **131** (36), 12989-12993 (2009).
9. A. Cossaro, R. Mazzarello, R. Rousseau, L. Casalis, A. Verdini, A. Kohlmeyer, L. Floreano, S. Scandolo, A. Morgante, M. L. Klein and G. Scoles, Science **321** (5891), 943-946 (2008).
10. P. Fenter, P. Eisenberger and K. S. Liang, Phys. Rev. Lett. **70** (16), 2447 (1993).
11. N. Camillone III, C. E. D. Chidsey, P. Eisenberger, P. Fenter, J. Li, K. S. Liang, G. Y. Liu and G. Scoles, J. Chem. Phys. **99** (1), 744-747 (1993).
12. G. E. Poirier and M. J. Tarlov, Langmuir **10** (9), 2853-2856 (1994).
13. E. Delamarche, B. Michel, C. Gerber, D. Anselmetti, H. J. Guentherodt, H. Wolf and H. Ringsdorf, Langmuir **10** (9), 2869-2871 (1994).
14. R. G. Nuzzo, L. H. Dubois and D. L. Allara, J. Am. Chem. Soc. **112** (2), 558-569 (1990).
15. R. G. Nuzzo, E. M. Korenic and L. H. Dubois, J. Chem. Phys. **93** (1), 767-773 (1990).
16. M. H. Dishner, M. M. Ivey, S. Gorer, J. C. Hemminger and F. J. Feher, J. Vac. Sci. Technol. A **16** (6), 3295-3300 (1998).

# Chapter 3
# DHCT Description

In this chapter we provide a full description of a post-processing real-space image registration and correction technique. Because it corrects thermal drift, hysteresis, and creep, we call this method the thermal-drift, hysteresis, and creep transform (DHCT). DHCT uses the lattice structure in the image as an internal standard for correcting distortion caused by dynamic effects. Distortion corrected images from DHCT allow consistent and accurate real-space measurements from STM images, with precision enough to register large continuous domains to a lattice. Most of this work was previously published in our paper in the Review of Scientific Instruments.[1]

DHCT employs a four-step procedure to correct distortion. 1) Find the location of each image feature (molecule or atom) with sub-pixel accuracy by fitting a 2D Gaussian to the feature's image. 2) Determine the local distortion around each feature by measuring the deviations of that feature's nearest neighbors (NNs) from their expected position. 3) Fit the trend of the local distortion with time to models for thermal drift, hysteresis, and creep. 4) Apply the inverse of the distortion to transform the image and feature data from the controller frame to the sample frame. Distortion correction is thus a recalculation of the in-plane coordinates of each feature and image pixel. It does not alter the z data, thereby maintaining measurement integrity.

Lapshin showed a proof of concept for a similar image correction that compensates for all types of STM image distortion[2] that our technique improves upon in several ways. Lapshin uses feature triplets that form equilateral triangles on the graphite(0001) surface to measure distortion parameters, resulting in both fewer measurements and higher measurement uncertainty than our nearest neighbor based distortion measurement. To fit the distortion measurements, Lapshin fits parabolic surfaces in x and y to his data, where we fit to functions of time chosen based on the

motion expected from the STM system. Finally and most notably, we demonstrate the specifics of our implementation of the technique and describe how it can be extended to systems other than the graphite(0001) surface with appropriate modifications.

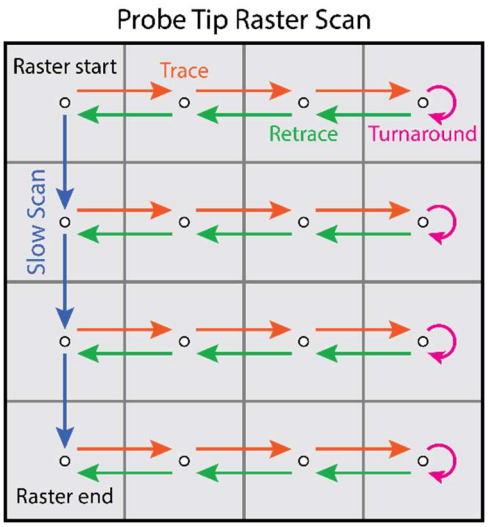


**FIG. 3.1.** An example STM image raster scan. Each pixel is acquired sequentially with approximately constant time delay between each acquired pixel (open circles). After data acquisition, the samples are displayed as a digital image, which is the grid of pixels arranged corresponding to their position in the raster scan. This example would produce a pair of 4 pixel × 4 pixel images, one from the trace (red arrows) and the second from the retrace (green arrows).

DHCT gives two primary results: a distortion-corrected and calibrated image of the sample surface and the indexed set of features used to determine the distortion. The indexed feature set includes positions, heights, and widths for each feature. Additional measurements on each feature can also be indexed for later analysis. Examples of applications for the DHCT software can be found in later chapters. Our tools and analyses in chapters 4 and 5 that measure, interpret, or visualize data from STM images require first processing the STM images with DHCT. Our implementation of DHCT in Matlab and sample STM data for testing are available online at GitHub. The method should work for any sample that fits the criteria discussed here, with some slight modifications to adapt it to different images.

### 3.1. Raster Scan Description

The tip is raster scanned over the surface by the STM controller to acquire images. An example raster scan is shown in Figure 3.1. Our STM system uses an open-loop controller, as is typical of most STM systems.[3, 4] The STM controller assumes a linear relationship between the

applied voltage of the tube scanner and the resulting motion of the tip. To generate the raster scan, the controller applies a series of constant voltage steps to the horizontal and/or vertical quadrants of the piezoelectric tube scanner. This causes the STM tip to move about the same distance over the surface on each step. The probe tip is scanned with constant-distance and constant-time steps along the first row of the scan window. When the tip reaches the end of the first line, after a brief turnaround time (magenta arrows), it is scanned in the opposite direction along the same row, taking measurements at the same rate. Because the probe tip moves fastest along these rows, this is called the fast-scan direction. We will refer to the initial scan line as the trace (red arrows), and the second scan back along the same line as the retrace (green arrows). After acquiring the entire row (trace and retrace), the tip is moved one pixel-width in the slow-scan direction (blue arrows), orthogonal to the fast-scan direction, and is scanned along another fast scan row. This process is repeated until the whole window is scanned. A pair of images is acquired this way, the trace image and the retrace image. The images are generated from the data by arranging the measurements into a square grid that matches the raster pattern generated by the STM controller.

Since the signal recorded by the STM is the height of the tip at a grid of points over the surface, STM images are essentially topographic images. They are not quite surface topography though—the STM does not touch the surface. The STM topography depends on the electronic properties and structure of both the surface and the tip, but for homogeneous samples and ideal tips the image closely approximates the surface topography of the sample.

In practice, the STM's absolute measurement accuracy is limited by the STM tip and the control systems that position it. Lattice structures of STM substrates and adsorbate overlayers are usually known very accurately via X-ray diffraction (XRD), low-energy electron diffraction (LEED), etc. These well-known measurements are frequently used to calibrate the STM controller

and can be used to calibrate short-range measurements on images. On close inspection, STM images often appear slightly warped, especially along the slow-scan direction. Drift due to thermal expansion (thermal drift), as well as piezoelectric actuator nonlinearities (hysteresis and creep), are not handled in real time by most STM controllers. Thermal drift causes the sample to move with respect to the tip over time, and piezoelectric actuator nonlinearities cause the constant-voltage steps to move the tip different distances. In addition, position sensors are not sensitive enough to facilitate closed-loop control for the STM at the atomic scale, in contrast to similar techniques like atomic force microscopy (AFM),[5, 6] where nanometer resolution and micron scan ranges are typical. The absolute measurement accuracy of STM images suffers unless these dynamic effects can be compensated. In principle it should be possible to post-correct any STM image that contains regions with known periodic structure, e.g. substrate atomic lattice or adsorbate overlayer.

Some image post-processing is common when analyzing STM images. Plane subtraction fitting for STM images is almost universal, since it is difficult to perfectly align the STM piezo scan plane and the sample. Since flat samples are necessary for good STM imaging, a plane subtraction can be performed by selecting a region of your image that looks flat and subtracting a plane with a matching slope from the whole image. This technique is simple and effective. In-plane corrections are becoming more common but are not yet as widespread. Commercial image processing software like Adobe's Photoshop, or SPM software packages like CRISP or Gwyddion, are used to do affine transformations of images to "touch up" distortion caused by the STM scan to match structures or make short-range measurements.[7, 8]

Some of the earliest work to correct for distortion in STM images involves measuring the average drift effect in an image and applying a voltage ramp to the scan piezoelectric actuators

that would compensate for that drift in future images.[9] Techniques like this one that modify the image as it is scanned are popular, as the images should not need post-processing if the scan control issues can be fixed in real time. Others have implemented real-time methods to correct distortion, e.g. by modifying the image raster scan in the controller frame using behavioral models for the piezoelectric actuators[4, 10-12] and the linearization of long-range hysteresis with software,[13] or by hardware linearization of the piezoelectric actuator response using charge control instead of voltage control.[14, 15] Recently, attempts have been made to change the scan trajectory based on measurements of distortion while the microscope is scanning.[16-18] Until STMs that can incorporate these real-time corrections into image acquisition become widely available, post-processing of STM images will be required to compensate for image distortion.

Most post-processing corrections in the literature tend to focus on only one of the sources of distortion in STM images. Post-processing hysteresis correction methods for STM images have been fairly successful,[19-23] usually not requiring more than a trace and retrace image. The trace-retrace image pair is only different due to their hysteresis, so a symmetric correction that maps both images onto the same image also undoes the hysteresis distortion in both images. Thermal drift correction techniques[21, 22, 24-28] often require additional information, e.g. a piece of the same image scanned with the fast-scan direction orthogonal to the original image[25] or multiple images acquired without moving the STM scan window.[21, 22, 28] Creep is commonly dealt with in STM images by waiting for a sufficient amount of time after the scan window is modified for the creep to reduce to a manageable level. Correcting for creep happens only in more general corrections, where it can be included at low additional computational cost. This kind of correction has started emerging only recently—for example, Lapshin's virtual mode technique can compensate for any kind of slow nonlinear STM image distortion.[2]

Techniques for correcting image distortion have been used successfully for other types of scanning microscopy. Digital image correlation (DIC) has been used to correct scanning electron microscopy (SEM)[29] and atomic force microscopy (AFM)[30, 31] images by determining image distortion caused by drift of the probe with respect to the sample. RevSTEM has been used in scanning transmission electron microscopy (STEM)[32] to correct problems caused by sample drift specific to STEM. Its creators also developed a per-feature post-processing analysis of their previously corrected STEM images.[33] Their methods have been applied to studies of crystallography with STEM.[34, 35] Crystallographic image processing (CIP), although not exactly a distortion correction technique, has been widely applied to electron microscope images[7] and recently expanded to a variety of other microscopies including STM.[36, 37] CIP creates unit cell images by enforcing an assumed symmetry using Fourier filtering and symmetry averaging. This can be advantageous in STM to smooth tip-profile effects which break the natural symmetry of the surface unit cell.

Fundamentally, image distortion in STM is caused by a discrepancy between the STM controller's model of the probe tip's location (the controller frame of reference) and the probe tip's true location over the surface (the sample frame of reference).[38] We will refer to these as the controller frame and the sample frame. Thermal drift of the sample with respect to the probe tip and nonlinearities of the piezoelectric actuator shift the probe tip position in the sample frame with respect to the controller frame. Shifts from thermal distortion and piezoelectric actuator nonlinearities are easily modeled by functions of time and voltage. A square data grid in the controller frame becomes a distorted grid in the sample frame due to the shift.[39] If this data were shown on the regular grid of the controller frame, the image would be distorted. This distortion disappears by transforming the data coordinates from the controller frame into the sample frame.

It is helpful to think of distortion as a time-dependent image transformation from the STM sample's frame of reference into the controller's frame of reference. This transformation must be undone to view the STM sample without the effect of distortion.

We use time as the independent variable to characterize how distortion varies across the image. This choice is convenient because thermal drift and piezoelectric actuator creep are inherently time dependent, and because time is invariant under the image transformation used to correct the image. The raster scan used to acquire the image provides a convenient mapping between time and position within the original image. In the controller frame, the time between any two image pixels can be easily calculated using the STM scan speed, the pixel size, and the raster pattern. In the following sections we will discuss the types of image distortion, the physical origin of the three types of distortions that effect STM images, and how distortion can be measured.

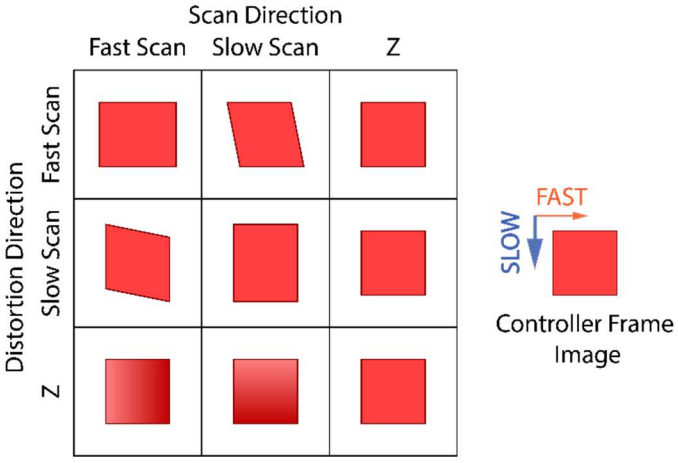


**FIG. 3.2.** Examples showing how each element of the transformation matrix modifies the scanned region in the sample frame. The controller-frame image is always a square. Displaying the non-square scanned region in a square causes it to appear distorted. The in-plane distortion elements cause stretch and shear, while the z distortion elements cause tilt. Shading (light to dark red) represents changes in z.

### 3.2. Time-independent Image Transformations

Time-independent affine image transformations can be described by a 3×3 transformation matrix **T** that transforms an image from one coordinate system to another (e.g., from the controller-frame image into the sample frame). For STM images, it is most natural to express **T** in terms of

the fast and slow-scan coordinates of the raster scan *f* and *s*, respectively, rather than the fixed coordinate frame of *x* and *y*. Each of the 9 matrix elements can be identified using a pair of indices from the set (*f*, *s*, *z*). To understand how the transformation matrix changes the image, we will explore how each transformation matrix element would modify a square image. These transformations are represented visually in Figure 3.2.

The simplest image transformation is the identity transformation, which leaves the image unchanged when applied to the image. In the identity transformation, the diagonal elements of the transformation matrix are 1, while the off-diagonal elements are 0.

$$\mathbf{T} = \begin{pmatrix} 1 & 0 & 0 \\ 0 & 1 & 0 \\ 0 & 0 & 1 \end{pmatrix} \tag{3.1}$$

### 3.2.1. Stretch

Stretching an image in a given direction causes distances in that direction to increase by an amount proportional to how much the image was stretched. Compression is a special case of stretching where the stretch amount is negative. The stretch transformation matrix is obtained from the identity transformation matrix by adding the stretch amount in each direction to the diagonal element of the transformation matrix for that direction.

$$\mathbf{T} = \begin{pmatrix} 1 + S_f & 0 & 0 \\ 0 & 1 + S_s & 0 \\ 0 & 0 & 1 + S_z \end{pmatrix} \tag{3.2}$$

$S_f$ and $S_s$ are the stretch amounts in the fast and slow-scan directions, respectively. If $S_f$ = 0.05 and $S_s$ = 0, the image will be stretched by 5% in the fast-scan direction. $S_z$ can be regarded as

a *z* calibration correction, which is most commonly accomplished in STM using images of an internal standard with known height, such as an atomic step.

### 3.2.2. Shear

Shearing an image in a given direction causes points to be offset in that direction by an amount proportional to their distance along a perpendicular direction. Shearing a square image in the plane transforms the square into a parallelogram, which changes the angular relationships between image features. Shear preserves the area of the image. The shear transformation matrix is obtained from the identity transformation matrix by adding the shear amount in direction *i* proportional to distance along perpendicular direction *j* to the transformation matrix element $\mathbf{T}_{ij}$.

$$\mathbf{T} = \begin{pmatrix} 1 & \mathbf{T}_{fs} & \mathbf{T}_{fz} \\ \mathbf{T}_{sf} & 1 & \mathbf{T}_{sz} \\ 0 & 0 & 1 \end{pmatrix} \tag{3.3}$$

To shear an image in the fast-scan direction by 2% of the distance in the slow-scan direction, simply set $\boldsymbol{T}_{fs}$ = 0.02 and the other shear matrix elements to zero, then apply that transformation to the image. The $\mathbf{T}_{fz}$ and $\mathbf{T}_{sz}$ matrix elements cause images to shear in proportion the *z* coordinate, e.g. the z axis is not orthogonal to the *x*-*y* plane. This introduces a lateral offset between the top of an image feature and the bottom of the feature. Ordinary atomic and molecular corrugation is very small, so the effect is usually insignificant. The most likely manifestation of $\mathbf{T}_{fz}$ and $\mathbf{T}_{sz}$ shear occurs through the larger *z* motion that results when sample tilt is present. The effect of this is simply an apparent change in the sample tilt.

### 3.2.3. Tilt

Image tilt is associated with distortion components with the same functional composition as the STM image, $z(x,y)$, which contribute to $\mathbf{T}_{zf}$ and $\mathbf{T}_{zs}$. STM practitioners commonly use plane subtraction to flatten STM images for analysis, a practice generally accepted for STM image processing because image tilt usually carries no useful information.[40] One cause of image tilt is sample tilt, the result of the sample surface and the image raster scan being non-coplanar. STM tunneling current feedback forces the raster scan to follow the sample surface, which causes sample tilt to shear the raster scan in the controller frame. Thermal drift and creep components in the $z$ direction also cause image tilt by shearing the raster scan in the controller frame. Piezoelectric tube scanners introduce a curvature to the images because they scan by bending—an effect that increases with increasing offset from the tube scanner's unbent origin.[41] First order effects of raster-scan curvature contribute to $\mathbf{T}_{zf}$ and $\mathbf{T}_{zs}$.

$$\mathbf{T} = \begin{pmatrix} 1 & 0 & 0 \\ 0 & 1 & 0 \\ \mathbf{T}_{zf} & \mathbf{T}_{zs} & 1 \end{pmatrix} \tag{3.4}$$

Plane subtraction of images with sample tilt causes the images to be foreshortened, compressing the image along the tilt gradient. Image tilt due to $z$ components of thermal drift and creep does not lead to image foreshortening and therefore can be fully corrected by plane and higher-order surface subtraction. The error caused by plane subtraction due to foreshortening will be captured in $\mathbf{T}_{ff}$, $\mathbf{T}_{fs}$, and $\mathbf{T}_{ss}$.

## 3.3. Mechanisms of Distortion in STM

Thermal drift and piezoelectric actuator nonlinearities cause the elements of the transformation matrix to vary with time. Our correction method solves for $\mathbf{T}_{ff}$, $\mathbf{T}_{fs}$, and $\mathbf{T}_{ss}$ as

functions of time using models for thermal drift and piezoelectric actuator nonlinearities. Based on these models, we expect the contribution from $\mathbf{T}_{sf}$ to be small compared to the other 3 elements due to the STM's much higher acquisition rate along the fast-scan direction. Simulated STM images in Figure 3.3 separate the effects of thermal drift, hysteresis, and creep and show how they manifest themselves differently depending on their direction with respect to the fast and slow scan directions.

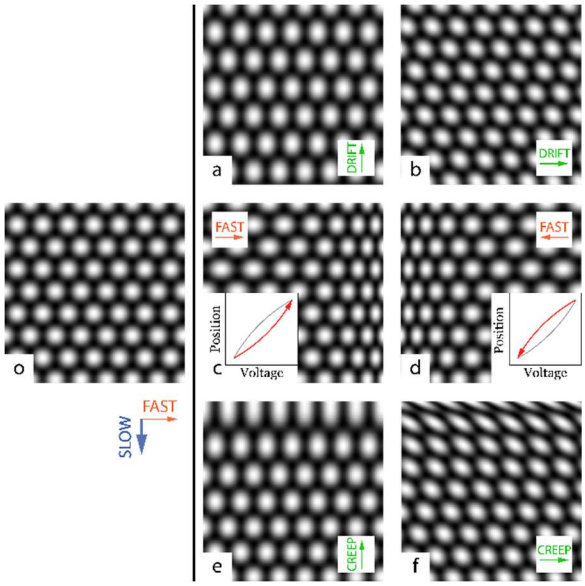


**FIG. 3.3.** Distortion effects on a simulated STM image of graphite 1 nm × 1 nm, scanned at 50 nm/s, 512 pixel × 512 pixel. (o) The undistorted image. Thermal drift, with a constant velocity of 10 pm/s opposite the slow-scan direction (a) and in the fast-scan direction (b). Hysteresis, the exaggerated effect of exponentially decaying hysteresis in the trace image (c) and the retrace image (d). Piezo creep opposite the slow-scan direction (e) and in the fast-scan direction (f).

### 3.3.1. Thermal Drift

Thermal drift describes the relative motion between the STM probe tip and the sample caused by thermal gradients and time-varying temperature. The mechanical framework of the STM thermally expands and contracts in response to these temperatures. The distance along physical connections between the tip and the sample is 3 to 4 orders of magnitude larger than a typical scan size,[39] so even a small change in temperature will cause noticeable displacement between the tip and sample.

In terms of its effect on the image, thermal drift causes the raster-scan window to move with respect to the sample during the image acquisition. The vector component of thermal drift parallel to the slow scan direction causes the scan lines to be farther apart or closer together in the sample frame, thus stretching or compressing the image features in the slow-scan direction in the

controller frame, as shown in Figure 3.3(a). The vector component of thermal drift parallel to the fast-scan direction causes the start of each subsequent scan line to be systematically and increasingly offset along the fast-scan direction in the sample frame, thus shearing the image features in the controller frame, as shown in Figure 3.3(b). The vector component of thermal drift parallel to the fast-scan direction also causes the data points in a scan line to be farther apart or closer together in the sample frame, thus stretching or compressing the image features in the fast-scan direction. This latter effect is insignificant in most usable images because its magnitude scales inversely with the fast-scan speed. In contrast, the first two effects scale inversely with the slow scan speed. For a 2048 pixel × 2048 pixel image, this causes the scan velocity along the slow-scan direction to be lower by a factor of about 4096. The magnitude of the $\mathbf{T}_{fs}$ and $\mathbf{T}_{ss}$ matrix elements are therefore the most important for determining the thermal drift.

### 3.3.2. Piezoelectric Actuator Hysteresis

Hysteresis is a property of piezoelectric actuators that causes them to trace out a different (non-linear) voltage-position curve depending on their history.[3, 42] The PZT piezoelectric material used in our lab's STM is a polycrystalline ceramic composed randomly oriented crystallites.[43] Each crystallite is composed of ferroelectric domains each contributing its dipole moment. The allowed orientations of the dipole axes are determined by the material's crystallography. Within that constraint, in the unpoled state the net dipole moment of the domains in each crystallite will be negligible. The random orientation of the crystallites produces a random distribution of allowed polarization axes throughout the material. Poling aligns the domain dipoles within each crystallite so they have a polarization component in the poling direction. The degree to which each domain contributes to the net polarization depends on the angle between each domain's dipole direction and the poling field. When the voltage applied to poled piezoelectric actuators is stepped, the

domains in the piezo become charged. This charge induces strain in the piezoelectric actuator which deforms it, thereby causing motion of the STM probe tip over the sample. The voltage step also brings additional domain dipoles into alignment with the electric field, which decreases the strain and the incremental motion.[44] At sufficiently large voltage, all of the domain dipoles would become aligned and further changes in applied voltage would cause only charging of the domains, resulting in an effectively linear position response to applied voltage. The hysteresis effect depends on the direction of the voltage step rather than the magnitude of the voltage at any given point. Hysteresis results from smaller mechanical displacement per volt when the voltage steps change direction from increasing to decreasing and vice versa, because the change initially drives more domain dipole realignment than charging.

Hysteresis manifests itself as stretching of the image features in the fast-scan direction at the start of each fast-scan line. Due to the STM's periodic motion, the effect of hysteresis in this direction quickly settles into a loop where hysteresis can be observed as a function of time since the scan-line start. An example with exaggerated hysteresis is shown in Figure 3.3(c) for the trace image (fast-scan direction left to right) and in Figure 3.3(d) for the retrace image (fast-scan direction right to left). The effect of hysteresis on each fast-scan line is the same even though each scan-line is acquired at a different time. This is advantageous, since each feature in the image can be used to correct each line, rather than only the features that appear on a single line. The fast-scan hysteresis information is contained in the $\mathbf{T}_{ff}$ matrix element. We do not model hysteresis in the slow-scan direction. Doing so would require information about the probe-tip motion occurring before the image was acquired, thus is not captured in a single image. Although slow-scan hysteresis modeling should be feasible for image sequences, its effect will be combined with

thermal drift and creep. Fortunately, the lowest-order components of the slow-scan hysteresis will appear identical to drift and creep and be captured in the $\mathbf{T}_{fs}$ and $\mathbf{T}_{ss}$ matrix elements.

### 3.2.3. Piezoelectric Actuator Creep

Piezoelectric actuator creep describes the dynamic property of piezoelectric actuator motion to approach the equilibrium position for their bias potential.[3, 42, 45] As explained in the hysteresis section, voltage applied to a piezoelectric actuator causes both strain and domain dipole alignment. Creep is caused by the slow relaxation of the voltage-induced domain dipole alignment to its new equilibrium state over time. As the domain dipoles relax to their equilibrium state, the domains gain additional charge, causing strain that further deforms the piezoelectric.[44] For a step-function voltage change on the piezoelectric actuator, most of the motion occurs as quickly as the mechanical resonance of the system allows. The remaining motion occurs logarithmically with time as the piezoelectric actuator relaxes to its ultimate position.[3, 42]

Large actuator motions, like those that occur during initial sample approach and when selecting a scan window, cause noticeable image distortion due to creep. The effect on the image appears like thermal drift, except with a decaying amplitude. As such, we consider only the $\mathbf{T}_{fs}$ and $\mathbf{T}_{ss}$ matrix elements, for the same reasons as thermal drift. Figure 3.3(e) shows the stretching caused by the creep vector component parallel to the slow-scan direction. Figure 3.3(f) shows the shear caused by the creep vector component parallel to the fast-scan direction.

## 3.4. Internal Standard and Region Masks

Typical samples imaged by STM consist of crystalline structures or commensurate overlayers. The deviation of the structure observed in the controller frame from the pristine crystal structures in the sample frame is likely due to the systematic distortion inherent in the controller

frame image. In this work, we use the NN distance as the reference value to correct distortion and to calibrate the image. If the exact NN distance is not known, a reasonable guess is sufficient to correct distortion. Strain in the sample also distorts the internal standard. In the case of soft materials, e.g. alkanethiol SAMs, this must be accounted for near defects, domain boundaries, and step edges. Using region masks to select data away from strained areas yields reliable distortion corrections that can then be applied to the whole image. Region masks facilitate correcting images from patches of the internal-standard structure, e.g. islands in multiphase systems. Performing distortion measurement in real space permits selection of any number of regions with any shape.

### 3.5. Measuring Linear Distortion

Henriksen and Stipp devised a method to determine linear drift parameters for scanning probe microscopy (SPM) images using the locations of the principle peaks of the Fourier transform.[27] Working with AFM images of graphite, they derived a set of equations that give distortion parameters related to the image transformation matrix elements $\mathbf{T}_{ff}$, $\mathbf{T}_{fs}$, and $\mathbf{T}_{ss}$ from the location of 3 unique peaks of the Fourier transform. Graphite exhibits a close-packed surface structure where each imaged carbon atom has 6 imaged NNs.[46] The Fourier transform of this regular trigonal lattice has six principle peaks. The peak locations depend on the NN distance and the distortion parameters. The authors characterized distortion in terms of the drift velocity components in the slow and fast-scan directions and a homogeneous scaling factor. The drift velocities are related to the matrix elements by the scan velocity in the slow-scan direction. The scaling factor is a constant multiplying **T** and refines the instrument calibration. After these parameters are obtained, they are used to apply a linear image transformation. Their method is applicable to determining and correcting time-independent distortion in any kind of raster-scan image, including STM. This method works for distortions that are uniform throughout the image,

but hysteresis, creep, and thermal drift vary with time, and therefore are not uniform across the image.

### 3.6. Measuring Local Distortion

By taking local measurements of linear distortion at many points throughout the image, we can determine the trend of the distortion with time. Initially we set out to do this by adapting the Henriksen-Stipp method using a sliding FFT. In this approach, a small window is moved across the image, using the FFT of each window to determine the local distortion at the center of the window. However, the sliding FFT approach has two drawbacks. First, distortion information is averaged over the FFT window. Reducing the window size to increase the spatial resolution comes at the expense of the k-space resolution, making it difficult to determine peak locations. Second, images with "interesting" features (like defects and boundaries) add additional Fourier components that make measurement of local distortion more difficult when the window contains those features.

As a solution to the problems with the sliding FFT method, we use the locations of image features in real space as the basis for DHCT. For graphite, since the imaged surface is a trigonal lattice of carbon atoms, the NNs should lie on a circle and be equidistant from each other and from the central atom, just like the peaks of the Fourier transform. By applying our method to each feature's NNs, we determine the local drift parameters at each feature location in the image. By performing the analysis in real space, we avoid the problems of the FFT and we add the ability to use region masks to select regions of the surface for analysis. The drift velocities are now determined as functions of time to account for creep and time-varying thermal drift, and the scale factor has been adapted to measure fast-scan hysteresis as a function of time since the beginning of the scan line. It should be noted that hysteresis depends on voltage rather than time. Voltage is

mapped to time for convenience, because the voltage is stepped at a constant rate in the fast scan direction.

### 3.7. Technique

The computations in this work were performed using Matlab 2016a on a Dell 7910 with dual 4-core Dual Intel Xeon processors (E5-2637), 128 GB RAM, and an NVIDIA Telsa K40 GPU.

#### 3.7.1. Pre-processing

Our analysis begins by reading the .sm3 or .sm4 STM image proprietary file format of RHK Technology into Matlab as a pair of matrices of *z* coordinates (the trace and retrace image) and the scan parameters from the file header. Once imported, analysis should be independent of the data acquisition software. Plane subtraction fitting is performed by selecting multiple continuous crystal domains with region masks, then the slope of the best-fit plane is found for all of the regions simultaneously and a plane with that slope is subtracted from the image. The tilt can also be manually adjusted to account for each individual sample, but corrections from the best-fit plane are usually small. Reduction of scan-line noise due to sudden tip changes is performed using the linear-regression fitting method from Fogarty et. al.[40] This method works by solving for and subtracting frequency noise in the slow-scan direction that is not correlated with image features.

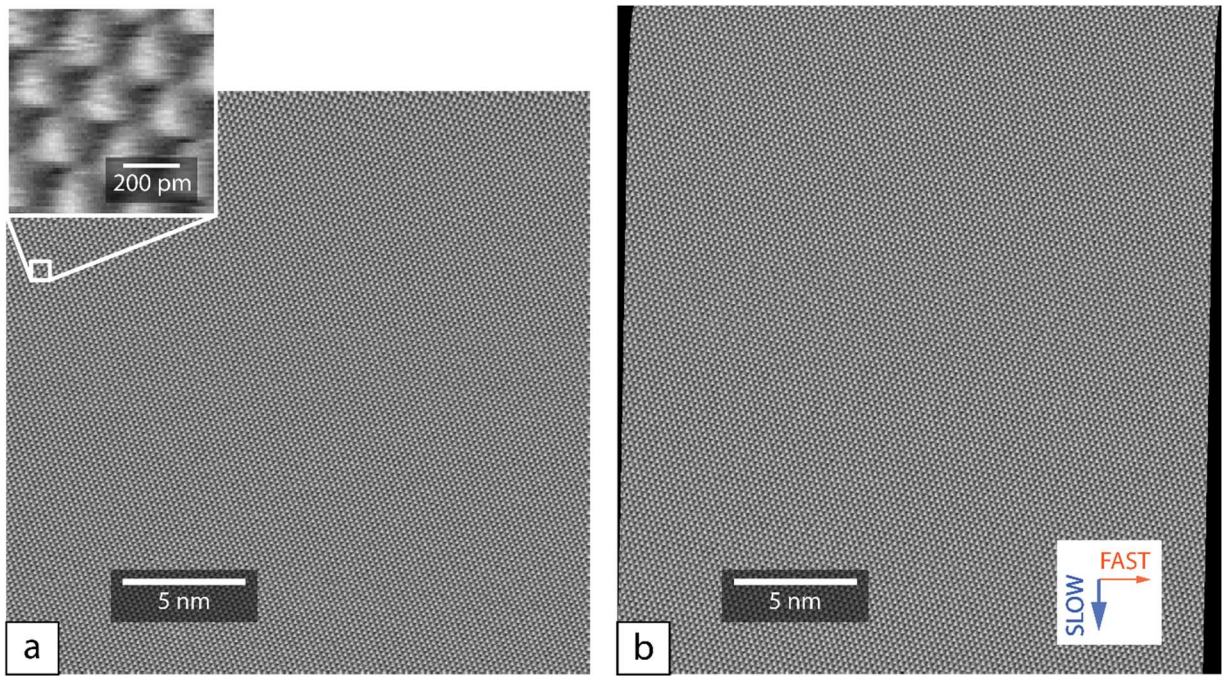


**FIG. 3.4.** (a) A 2048 pixel × 2048 pixel STM image of graphite after pre-processing, acquired at −60 mV sample bias and 160 pA tunneling current. The image is nominally 25 nm × 25 nm scanned at 100 nm/s. The inset is 800 pm × 800 pm section, outlined in white, is magnified in the inset to show the surface texture. (b) The same image with the total drift correction applied to it. Note that the image is no longer square, the region shown more accurately shows the shape of the region scanned on the surface.

Only images with high quality can be used. After this pre-processing, the *z* coordinates of the topographic image are no longer modified. Subsequent distortion correction modifies the fast and slow-scan coordinates of each pixel according to the determined distortion, which can be applied to the processed data or the raw data, whichever is more suitable for the application.

We chose to use graphite as the primary sample for this chapter, both because it is widely studied and due to the rigid nature of the surface structure, compared to soft systems such as alkanethiol SAM surfaces. An image processed as described above is shown in Figure 3.4(a) with its distortion-corrected image Figure 3.4(b). The image selected was free of large probe tip changes and the lattice was imaged coherently. As you can observe from the inset in Figure 3.4(a), the probe tip is not ideal, but nevertheless produced stable atomic-resolution images. The secondary example is a STM image of a decanethiol SAM on Au(111), which includes a substrate step edge,

two terraces, and two large SAM structural domains, Figure 6.3. Region masks are needed to limit the distortion measurement to regions of SAM domains away from the domain boundaries and step edge.

### 3.7.2. Initialization

Our implementation of DHCT begins with the image to be drift corrected as a 2D matrix of $z$ coordinates, and a few parameters describing the image. The distance between any two adjacent pixels (in meters), the time between two sequential pixel acquisitions (in seconds), a pair of strings indicating the slow and fast-scan directions, and the known NN feature distance (in meters). Except for the known NN distance (internal standard), the other values should be the image parameters recorded with the image. These parameters let us determine the scan controller frame of reference as accurately as possible. If a trace and retrace image are to be analyzed simultaneously, both images and the fast-scan direction for each image must be supplied, the other parameters are the same for both images. Optionally, a logical region mask the same size as each image can be included, which will make our software use only positively-masked features for the distortion analysis. An image consisting of multiple structural domains and atomic terraces, are shown in Figure 6.3. Masks should be chosen to exclude surface defects, domain boundaries, step edges, or regions with different or unknown structure. The unmasked areas will still be corrected for distortion, but those regions will not be used to calculate the distortion used in the correction. A good correction requires representative regions across the entire image, and the best corrections use as much of the image as possible. Images that can be corrected by the technique must also have spatially resolved features. Larger-scale studies for images with e.g. multiple step edges will often have pixel density too low to resolve individual features for this technique.

The equations in the following sections assume that $x$ is the fast-scan direction and $y$ is the slow-scan direction for the sake of using simplified coordinate nomenclature. The coordinates that correspond to the fast-scan and slow-scan directions are defined in the initial image parameters passed to the DHCT software.

### 3.7.3. Feature Indexing

We begin with a standard pixel-based cross-correlation. A kernel image of a feature that has the same approximate size and shape as the image features is generated. We have chosen a radially symmetric 2D Gaussian as a kernel for the two model systems discussed here, but the kernel could be any size or shape. Our kernel is a $(4\sigma + 1) \times (4\sigma + 1)$ square of pixels, where $\sigma$ is chosen to the nearest half-integer based on the size of the image features in pixels. Images with fewer than 10 pixels for each image feature (3 pixel diameter or less) will cause issues when determining feature locations because the kernel size will be too small. The image is cross-correlated with the kernel and a threshold is applied to select regions with a correlation > 0.1 (regions that look like the Gaussian). An example cross-correlation image for the inset from Figure 3.4 is shown in Figure 3.5. Each individual region, selected by the cross-correlation and isolated using a watershed function, is fit in the least-squares sense to a more accurate shape model. For this fitting we used this more general 2D Gaussian:

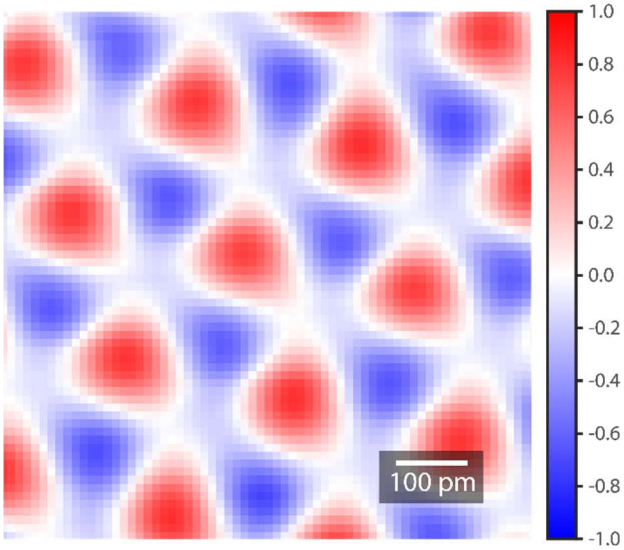


**FIG. 3.5.** The cross-correlation of the inset part of Figure 3.3 with the chosen Gaussian kernel. Red (blue) indicates positive (negative) correlation. A threshold at correlation +0.1 combined with a watershed function on the cross-correlation data selects pixel regions of the surface to analyze with Gaussian fitting.

$$g(x,y) = A\exp\left(\frac{-[(x-x_0)\cos\theta+(y-y_0)\sin\theta]^2}{{\sigma_1}^2} + \frac{-[(x-x_0)\sin\theta+(y-y_0)\cos\theta]^2}{{\sigma_2}^2}\right) + z_0, \quad (3.5)$$

where $x_0$, $y_0$, and, $z_0$ are coordinates of the center of the base of the Gaussian, $A$ is its amplitude, $\sigma_1$ and $\sigma_2$ are its standard deviations in 2 orthogonal directions, and $\theta$ is the rotation angle. The height of the center of the feature is $A + z_0$. This 2D cross-correlation and Gaussian fitting was inspired by a similar technique in STEM by Sang, Oni, and LeBeau.[33] We save all of these parameters for each feature in the image with an index to keep track of features for subsequent analysis.

### 3.7.4. Time Assignment

Time isn't recorded explicitly for the original image in our STM, but assigning a time to the image features is necessary for determining the distortion trends with time. Because the sampling rate of the STM is approximately constant, the software can assign a time to each image pixel based on their known chronological order from the raster scan and from the pixel acquisition rate determined by the scan velocity. In principle, the actual acquisition time of each image pixel in the original STM image could be recorded in a separated clock channel, but the approximate pixel time calculated from the scan speed is sufficient. Image features are not localized to individual pixels, they are imaged by many pixels over multiple raster-scan lines. For example, in Figure 3.4 each feature is imaged by approximately 111 pixels over 12 raster-scan lines. The location of each image feature is derived from the 2D-Gaussian fit to pixels across many raster-scan lines. For our analysis we assign a time to each feature based on the time of the image pixel nearest to its best-fit location.

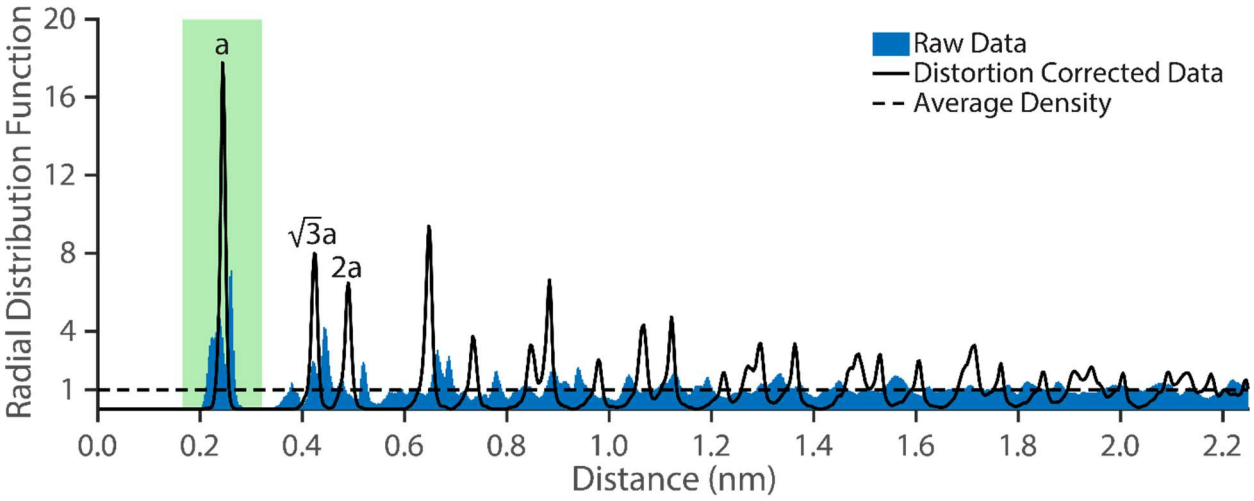


**FIG. 3.6.** The radial distribution function of image features is used to choose NNs. The NN distance for the imaged carbon atoms in graphite, $a$ = 2.46 Å, is used to classify the first 3 peaks of the density correlation (filled blue region). Gaussians centered at $a$, $\sqrt{3}a$, and $2a$ are fit to the unprocessed data to determine the NN distance. All of the features in the green shaded region are used as NNs in the analysis. After the correction, the peaks form the expected radial distribution function for a trigonal lattice (solid black line).

### 3.7.5. Finding Nearest Neighbors

The spatial relationship of the features is determined by first calculating the distance between every pair of features. The radial distribution function of the indexed features (Figure 3.6) shows the aggregate probability density of finding a feature a certain distance away from any other feature, normalized to unity at infinite separation. The first and highest maximum of the radial distribution function occurs at the NN distance, which we will call $a$. To determine $a$ as accurately as possible for the supplied image, Gaussians centered at $a$, $\sqrt{3}a$, and $2a$ (the nearest, next-nearest and next-next-nearest neighbor distances) are fit to the radial distribution function. The value of $a$ is determined accurately enough this way to pick each feature's NNs. The NNs of each feature fall within the shaded box in Figure 3.6, within ±35% of $a$. This technique works well for finding NNs,

but due to peak broadening at larger feature separations and overlapping peaks, more distant features cannot be reliably selected with the radial distribution function of the raw data. After identifying all of the NNs, we select only the features with the correct number of NNs, e.g. graphite's six imaged NNs.[46] This selection excludes features near defects, mask region edges, the edges of the image, and feature finding errors. Usually there are zero errors, but occasionally an image feature will be found twice (due to scan noise), causing both of those features and each of their NNs to have too many NNs.

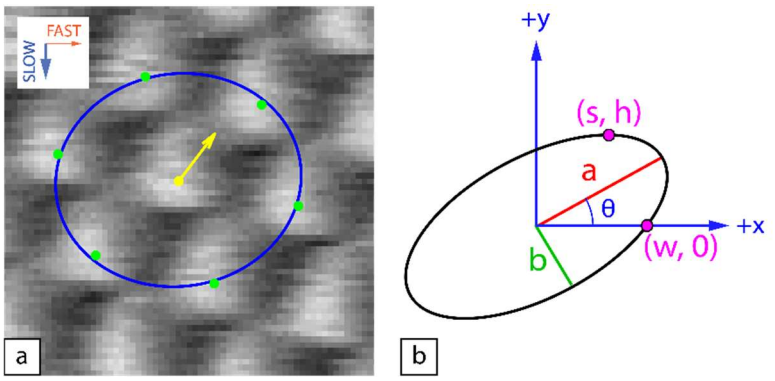


**FIG. 3.7.** (a) The inset from Figure 3.3(a), with the central feature's NNs (green), the best-fit ellipse to those NNs (blue), and the drift velocity vector that would cause a circle to be distorted to that ellipse (yellow) overlaid. We determine the drift velocity at each feature location on the surface, thus the velocity determination happens many times. (b) A diagram of an ellipse showing its semi-major axis $a$ and semi-minor axis $b$, with its semi-major axis at an angle $\theta$ from the +x axis, and the derived parameters $s$, $h$, and $w$.

### 3.7.6. Determining Local Distortion

DHCT uses each molecule's NNs to determine the local distortion using points chosen in real space. For each of the sets of NN locations, we determine the best-fit ellipse from the minimization of this sum:

$$\sum_{i=1}^{N}\left[\left(\frac{(x_i-x_0)\cos\theta-(y_i-y_0)\sin\theta}{a}\right)^2+\left(\frac{(x_i-x_0)\sin\theta+(y_i-y_0)\cos\theta}{b}\right)^2-1\right]^2, \qquad (3.6)$$

where $(x_i, y_i)$ are the coordinates of the $i$th of $N$ NNs (Figure 3.7(a)). The parameters of the best-fit ellipse are the center of the ellipse $(x_0, y_0)$, the semi-major axis $a$, the semi-minor axis $b$, and the angle to the semi-major axis $\theta$. I turn these measurements into three useful derived parameters: the shear offset and height of the highest point on the ellipse from the center ($s$, $h$), and the width

from the center of the ellipse to the *x* intercept *w*, Figure 3.7(b). The height *h*, determined from the ellipse equation by setting $\frac{dy}{dx} = 0$, solving for *y* and choosing the positive solution, is given by

$$h = \sqrt{(a\ \sin\theta)^2 + (b\ \cos\theta)^2}\ . \tag{3.7}$$

The shear offset *s* is related to *h* by solving the original ellipse equation for *x* and evaluating it at $y = h$,

$$s = \frac{h \sin\theta \cos\theta (a^2 - b^2)}{(a\ \sin\theta)^2 + (b\ \cos\theta)^2}\ . \tag{3.8}$$

The width *w* is one of the axes of the ellipse before undergoing the shear transformation. Since the shear transformation preserves the area of the ellipse, the area of the best-fit ellipse $\pi ab$ and the area of this un-sheared ellipse $\pi wh$ must be the same,

$$w = \frac{ab}{h}\ . \tag{3.9}$$

The scale correction, a ratio of input to output intermolecular distance, is a unitless constant derived from *w* and $r_0$,

$$S = \frac{w}{r_0}\ , \tag{3.10}$$

where $r_0$ is the user-supplied value of the NN distance. The shear offset is converted into a drift velocity by multiplying by the scan velocity in the slow-scan direction $v_0$

$$D_x = v_0 \frac{s}{h}\ . \tag{3.11}$$

The height is similarly converted into a drift velocity, but we subtract $v_0$ to remove the effect of the real net scan velocity in that direction

$$D_y = v_0 \left(\frac{r_0}{h} - 1\right)\ . \tag{3.12}$$

The software assigns the distortion parameters $D_x$, $D_y$, and $S$ determined from each feature's NNs to that feature for determining the distortion trend with time from the distortion models. An example showing the location of features, their best-fit ellipse, and the resultant drift vector are shown in Figure 3.7(a). Our model of the NN structure does not assume the NNs should be uniformly spaced around the central feature—only that they are at a uniform distance (fall on a circle). This model should work for disordered systems as well, provided that identifiable features can be resolved and have a well-defined mean NN distance.

### 3.7.7. Determining Distortion Trends

To visualize the trend for hysteresis in the fast-scan direction, we plot $S$ as a function of time since the beginning of the scan line (Figure 3.8). We find the best-fit curve to the data that obeys the power law function:

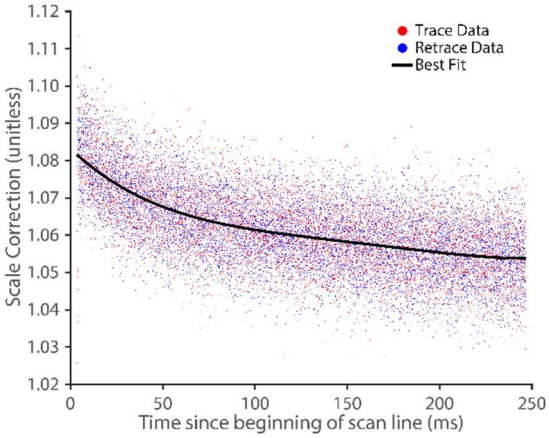


**FIG. 3.8.** Curve of best fit following our hysteresis model to a plot of scale correction vs time since the beginning of the fast-scan line.

$$S(t) = at^k \,, \tag{3.13}$$

where $a$ is the amplitude of the power law function and $k$ is the exponent. A power law function was chosen for its simplicity, since fully modeling the hysteresis curve requires many free parameters. We have also explored using the exponential and polynomials as a fitting function but find they do not capture the trend of the data as well. Liu, et. al. were able to fully model a hysteresis loop using a fractional-order Maxwell resistive capacitor model with 21 free parameters,[44] where the power law model uses only 2. A best-fit curve to the hysteresis data for one of our images is shown in Figure 3.8.

To visualize the trends of drift and creep, we plot the drift velocity in both the slow and fast-scan directions as a function of time (Figure 3.9). We find the best-fit curve to the drift velocity[42] that obeys the function

$$D_{x,y}(t) = v_{x,y} + a_{x,y}t + \frac{C_{x,y}}{(t + t_0)}, \tag{3.14}$$

where $v_{x,y}$ is the drift velocity from thermal drift, $a_{x,y}$ is the drift acceleration from thermal drift, and $C_{x,y}$ is the creep function amplitude. The effective time since the impulse that caused the creep, $t_0$, is the only fitting parameter shared by both the $D_x$ and $D_y$ fits. The *x, y* subscripts indicate orthogonal components of the drift vector in the *x* and *y* direction. Including the drift acceleration term significantly improves the image correction. Note that most of the published thermal drift corrections assume a constant velocity thermal drift, which results in a simple linear image correction (affine transformation).[9, 24-27] This can be attributed to the added complexity of measuring and applying a nonlinear correction, which we are already obliged to do because of the piezoelectric actuator nonlinearities. We are using the log($t$) style creep model where the position offset is related to log($t/t_0$), so the creep velocity depends on its derivative, or $(t + t_0)^{-1}$. Figure 3.9

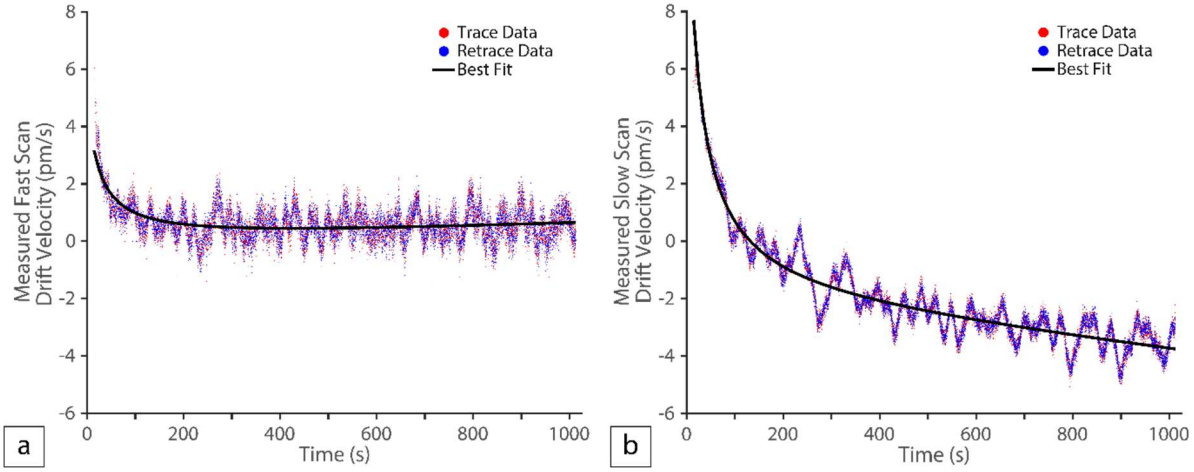


**FIG. 3.9.** Curves of best fit following our thermal drift and creep model to a plot of measured drift velocity vs time since the beginning of the raster scan. Measured drift velocity is proportional to image distortion matrix elements. Fluctuations around the best-fit curves are likely due to changing tip conditions over the scan time.

shows a plot of measured local drift velocities in both scan directions with their best-fit drift velocity curve according to this model.

In this procedure we simultaneously fit distortion around each feature in the feature sets from the trace and retrace images to the 9 parameters of our distortion model. Considering that this image pair is composed of $2^{23}$ pixels containing a combined total of 22,744 features, 9 parameters should not over fit the data. The deviations about the best-fit curve in Figure 3.8 are uniform across the line because the time scale is short. In contrast the scatter about the best-fit curves in Figures 3.9(a) and (b) vary on a time scale of minutes and are correlated in time. We attribute the residual scatter to changes in the probe-tip.

### 3.7.8. Applying Image Correction

Combining the systematic distortions of the STM image, the *x*-*y* coordinates of the features and image pixels can be mapped from the controller frame into the sample frame. We integrate the best-fit curves for the distortion model (eqs. 3.13 and 3.14, Figures 3.8 and 3.9) to determine displacement from effective drift velocity and evaluate the integral at each time point to find the controller-frame-to-sample-frame displacement at that point. By adding this to its location we obtain the corrected coordinates. The original image is composed of square pixels on a regularly spaced grid, while the corrected image is just a set of (*x, y, z*) data. It is important to understand that this distortion correction does not alter the measured topography (*z* coordinate), so the STM data integrity is preserved. However, display of the corrected image as a standard raster graphic does require resampling the corrected image onto a regularly spaced array. This can be accomplished using the Matlab griddata() function. Black bars on the side of these new images fill

the image rectangle where no data are available rather than cropping data out of the image. The results of DHCT can be seen in Figure 3.4(b) for graphite and in Figure 6.3 for a SAM on Au(111).

### 3.7.9. Expanding to Different Surface Lattice Structures

The implementation of the software described above applies only to a trigonal lattice, which was applicable to the surface structures we commonly encountered in our experiments. It can be expanded to other surface structure symmetries with a few modifications. The number of nearest neighbors will be lower for other surface lattice structures, so an appropriate set of nearby features must be selected and characterized somehow. At least five features must be characterized in order to uniquely parametrize an ellipse, though six or more features are not problematic. Additional features would give the ellipse fit higher noise tolerance. If the features are not the same distance from the central feature, the ellipse fit to neighboring features must be modified to a set of similar concentric ellipses by minimizing

$$\sum_{i=1}^{N}\left[\left(\frac{(x_i-x_0)\cos\theta-(y_i-y_0)\sin\theta}{a}\right)^2+\left(\frac{(x_i-x_0)\sin\theta+(y_i-y_0)\cos\theta}{b}\right)^2-\left(\frac{r_i}{r_0}\right)^2\right]^2. \qquad (3.15)$$

Here, $(x_i, y_i)$ are the coordinates of the *i*th nearest neighbor. The center of the ellipses ($x_0$, $y_0$), the semimajor and semiminor axes of the smallest ellipse $a$ and $b$, and the angle to the semimajor axis $\theta$ are analogous to the single ellipse case from the trigonal lattice. $r_0$ is the user-supplied value of the nearest neighbor spacing, while $r_i$ is the expected distance from the center feature to the *i*th feature from the lattice structure. If the *i*th molecule is e.g. a next nearest neighbor molecule, then $r_i$ would be the next nearest neighbor distance. Thus $\frac{r_i}{r_0}$ is thus the distance to the central feature in nearest neighbor distances. These should be easy to calculate for a given lattice structure. This set of changes to my software should handle any surface lattice structure.

### 3.8. Data Structure Description

DHCT outputs a data structure that contains all calculation results—indexed arrays of feature properties, corrected and uncorrected images, the parameters calculated to generate the image correction, accurate x and y coordinates of pixel locations, and more. For example, if you run

Data_Out = DHCT(XScale, Period, SlowScanDirection, FastScanDirection, NNdist, Img1, Img2);

The output data structure will be named Data_Out. You can access the subfields of data structures with a period. For example, to access the corrected Img1 from the data structure Data_Out, use this command:

Data_Out.ReshapedImage{1}

Note all variable names described in this file are case sensitive. The variables in this section do not depend on whether a single image or a trace-retrace pair were analyzed:

SlowPixels - 1×1 double. Original size of input image(s), in pixels, along the slow scan direction.

solution_vector - 1×9 double by default. Contains the parameters of the best-fit hysteresis, creep and thermal drift functions. If you modify the fitting functions, the length of solution_vector will be equal to the number of free parameters of your fit.

The variables in this section depend on whether a single image or a trace-retrace pair were analyzed. n is number of images, 1 for single, 2 for trace-retrace pair:

fit_data - 1×n cell. Each cell contains a "fitresult" data structure containing the following vectors. The vectors have size 1×(number of features). If there are 12047 features, each vector is 1×12047.

Amplitude - double vector of best-fit Gaussian amplitude for a given feature

Angle - double vector of best-fit angle between SigmaX axis of the Gaussian and the +x axis for a given feature

SigmaX - double vector of best-fit Gaussian standard deviation in the SigmaX direction for a given feature

SigmaY - double vector of best-fit Gaussian standard deviation perpendicular to the SigmaX direction for a given feature

X - double vector of X coordinates of base of best-fit Gaussian for a given feature

Y - double vector of Y coordinates of base of best-fit Gaussian for a given feature

Z - double vector of Z coordinates of base of best-fit Gaussian for a given feature

Index - double vector of unique indices of features. These are not changed and can therefore be used to keep track of image features between data structures.

Time - double vector of feature approximate acquisition times, assigned by the acquisition time of the nearest pixel to the center of the Gaussian.

Fast_Time - double vector of feature approximate acquisition times along the fast scan direction. Remainder of time after dividing by amount of time it takes to acquire one fast scan line.

mask_fit_data - 1×n cell. Each cell contains a "fitresult" data structure (Described in the description for fit_data) with the following additions. Each of these are 1×(number of features within masked regions) vectors.

:

Num_NN - sparse double vector of number of nearest neighbors of a given feature.

NN_Index - cell vector. Each cell contains a 1×(Num_NN) vector of the Index value of each of its nearest neighbors.

In addition, only features which lie in the positively-masked regions of a supplied region mask will be included. However, if no mask is supplied, all features will be included.

mask_drift_data - 1×n cell. The data structure is identical to mask_fit_data, except that X and Y have been modified to line up with the drift-corrected image.

feat_pos_nn - 1×n cell. Each cell contains a data structure with these elements:

feat_set - double vector. feat_set lists the vector element locations where Num_NN == 6 (from mask_fit_data). The length corresponds with how many features have six NNs.

Index - double vector. The value of Index from mask_fit_data corresponding to each element of feat_set.

cen_x - double vector. The value of X from mask_fit_data corresponding to each element of feat_set.

cen_y - double vector. The value of Y from mask_fit_data corresponding to each element of feat_set.

nn_x - double matrix. The value of X from mask_fit_data corresponding to the nearest neighbors of each element of feat_set.

nn_y - double matrix. The value of Y from mask_fit_data corresponding to the nearest neighbors of each element of feat_set.

Since each feature has 6 nearest neighbors, nn_x and nn_y each have 6 rows.

driftX - 1×n cell. Each cell contains a vector of measured drift velocities along the fast scan direction. The vector has size 1×length(feat_set) (from feat_pos_nn)

driftY - 1×n cell. Each cell contains a vector of measured drift velocities along the slow scan direction. The vector has size 1×length(feat_set) (from feat_pos_nn)

scaleFactor - 1×n cell. Each cell contains a vector of measured scale factors along the fast scan direction. The vector has size 1×length(feat_set) (from feat_pos_nn)

xCoords - 1×n cell. Each cell contains the modified x coordinates for each pixel in the original image and an additional pixel at the beginning and the end of each fast scan direction row.

yCoords - 1×n cell. Each cell contains the modified y coordinates for each pixel in the original image and an additional pixel at the beginning and the end of each fast scan direction row.

xOffset - 1×n double vector. Horizontal offset between input image and output corrected image.

yOffset - 1×n double vector. vertical offset between input image and output corrected image.

ReshapedImage - 1×n cell. Each cell contains a drift-corrected image. The image's size depends on the measured distortion parameters, but both images from a trace-retrace pair should be nearly the same size.

### 3.9. References


1. M. P. Yothers, A. E. Browder and L. A. Bumm, Rev. Sci. Instrum. **88** (1), 013708 (2017).
2. R. V. Lapshin, Appl. Surf. Sci. **378**, 530-539 (2016).
3. S. Devasia, E. Eleftheriou and S. O. R. Moheimani, IEEE Trans. Contr. Syst. Technol. **15** (5), 802-823 (2007).
4. S. O. R. Moheimani, Rev. Sci. Instrum. **79** (7), 071101 (2008).
5. A. J. Fleming, Sens. Actuators A: Phys. **190**, 106-126 (2013).
6. M. A. Cullinan, R. M. Panas, C. M. DiBiasio and M. L. Culpepper, Sens. Actuators A: Phys. **187**, 162-173 (2012).
7. S. Hovmöller, Ultramicroscopy **41** (1), 121-135 (1992).
8. D. Nečas and P. Klapetek, Open Physics **10** (1), 181-188 (2012).
9. R. M. Feenstra, J. Vac. Sci. Technol. B **7** (4), 925-930 (1989).
10. C. J. Chen, Appl. Phys. Lett. **60** (1), 132-134 (1992).
11. M. E. Taylor, Rev. Sci. Instrum. **64** (1), 154-158 (1993).
12. G. Aloisi, A. Santucci, M. Carla, D. Dolci and L. Lanzi, Rev. Sci. Instrum. **77** (7), 073701 (2006).
13. J. Akila and S. S. Wadhwa, Rev. Sci. Instrum. **66** (3), 2517-2519 (1995).
14. R. C. Munoz, P. Villagra, G. Kremer, L. Moraga and G. Vidal, Rev. Sci. Instrum. **69** (9), 3259-3267 (1998).
15. H. Kaizuka, Rev. Sci. Instrum. **60** (10), 3119-3122 (1989).
16. L. Zhang, Q. Long, Y. Liu, J. Zhang and Z. Feng, Ultramicroscopy **166**, 16-26 (2016).
17. R. V. Lapshin, Appl. Surf. Sci. **359**, 629-636 (2015).
18. R. V. Lapshin, Appl. Surf. Sci. **470**, 1122-1129 (2019).
19. J. F. Jorgensen, K. Carneiro, L. L. Madsen and K. Conradsen, J. Vac. Sci. Technol. B **12** (3), 1702-1704 (1994).
20. E. P. Stoll, Rev. Sci. Instrum. **65** (9), 2864-2869 (1994).
21. R. V. Lapshin, J. Surf. Invest. **1** (6), 630-636 (2007).
22. R. V. Lapshin, Meas. Sci. Technol. **18** (3), 907-927 (2007).
23. J. F. Jorgensen, K. Carneiro and L. L. Madsen, Nanotechnol. **4** (3), 152-158 (1993).
24. B. S. Salmons, D. R. Katz and M. L. Trawick, Ultramicroscopy **110** (4), 339-349 (2010).
25. N. D. Follin, K. D. Taylor, C. J. Musalo and M. L. Trawick, Rev. Sci. Instrum. **83** (8), 083711 (2012).
26. J. F. Jorgensen, L. L. Madsen, J. Garnaes, K. Carneiro and K. Schaumburg, J. Vac. Sci. Technol. B **12** (3), 1698-1701 (1994).
27. K. Henriksen and S. L. S. Stipp, Am. Mineral. **87** (1), 5-16 (2002).
28. P. Rahe, R. Bechstein and A. Kühnle, J. Vac. Sci. Technol. B **28** (3), C4E31-C34E38 (2010).
29. A. S. Michael, L. Ning, G. Dorian, C. Nicolas, O. Jean Jose, R. M. Stephen, W. S. Hubert and L. Xiaodong, Meas. Sci. Technol. **17** (10), 2613 (2006).
30. Y. Sun and J. H. L. Pang, Nanotechnol. **17** (4), 933 (2006).
31. Z. H. Xu, X. D. Li, M. A. Sutton and N. Li, J. Strain Anal. Eng. Des. **43** (8), 729-743 (2008).
32. X. Sang and J. M. LeBeau, Ultramicroscopy **138**, 28-35 (2014).
33. X. Sang, A. A. Oni and J. M. LeBeau, Microsc. Microanal. **20** (6), 1764-1771 (2014).

34. J. H. Dycus, J. S. Harris, X. Sang, C. M. Fancher, S. D. Findlay, A. A. Oni, T.-t. E. Chan, C. C. Koch, J. L. Jones, L. J. Allen, D. L. Irving and J. M. LeBeau, Microsc. Microanal. **21** (4), 946-952 (2015).
35. A. Belianinov, Q. He, M. Kravchenko, S. Jesse, A. Borisevich and S. V. Kalinin, Nat. Comm. **6**, 7801 (2015).
36. P. Moeck, in *Microscopy: Science, Technology, Applications and Education*, edited by A. Méndez-Vilas and J. Díaz (FORMATEX, Badajoz, Spain 2010), Vol. 3, pp. 1952-1962.
37. B. Moon, Masters, Portland State University, 2011.
38. L. Libioulle, A. Ronda, M. Taborelli and J. M. Gilles, J. Vac. Sci. Technol. B **9** (2), 655-658 (1991).
39. D. W. Pohl, IBM J. Res. Dev. **30** (4), 417-427 (1986).
40. D. P. Fogarty, A. L. Deering, S. Guo, Z. Wei, N. A. Kautz and S. A. Kandel, Rev. Sci. Instrum. **77** (12), 126104-126103 (2006).
41. S. Yang and W. Huang, Rev. Sci. Instrum. **69** (1), 226-229 (1998).
42. J. Peng and X. Chen, Mod. Mech. Eng. **3** (1), 1-20 (2013).
43. A. R. von Hippel, *Dielectrics and waves*. (Wiley, 1954).
44. Y. Liu, J. Shan, U. Gabbert and N. Qi, Smart Mater. Struct. **22** (11), 115020 (2013).
45. K. R. Koops, P. M. L. O. Scholte and W. L. de Koning, Appl. Phys. A **68** (6), 691-697 (1999).
46. S. Hembacher, F. J. Giessibl, J. Mannhart and C. F. Quate, Proc. Natl. Acad. Sci. **100** (22), 12539-12542 (2003).

# Chapter 4
# In-Plane Image Analysis Tools

We have shown in chapter 3 how to measure and correct the distortion due to thermal drift, hysteresis, and creep of STM images using NN image features. This process also allows assignment of feature indices to each surface feature that we use in future analysis, such as their relative position in *x*, *y,* and *z*; information about their shape; and which features are NNs. This NN-based correction is remarkable in its ability to restore long-range order well enough to determine a best-fit lattice to the data.

In this chapter we will show several tools that take advantage of the in-plane image corrections applied by DHCT. Lattice fitting allows further improvement of the lattice registration and simpler application of lattice techniques to image data. Averaged unit cell images and feature confidence ellipses are measurements that take advantage of the lattice fit to spatially average our results to increase our signal-to-noise ratio. Symmetry averaging is demonstrated to further increase averaging for symmetric surfaces. We show a time series lattice alignment, which allows for temporal averaging in addition to or in place of spatial averaging. We also show some data visualizations for the $(2\sqrt{3} \times 3)$rect. unit cells that de-emphasize the $(\sqrt{3} \times \sqrt{3})R30°$ sublattice that alkanethiol surface unit cells appear to have at first glance.

## 4.1 DHCT Second Pass for Alkanethiols

In chapter 3 we described how DHCT corrects STM images of a trigonal one-molecule lattice. This method works excellently for images of graphite, but images of alkanethiol SAMs deviate slightly from a trigonal lattice. We use a two-pass DHCT correction to account for the differences between the alkanethiol SAM 4-molecule-basis unit cell and the trigonal lattice

assumed by DHCT. The first pass of DHCT is exactly as it was described in chapter 3. We then use the first-pass corrected image to identify the 6 features that are exactly four nearest neighbor distances away in the nearest-neighbor directions of the lattice. The set of six features collected this way are guaranteed to be symmetry-equivalent lattice sites for any rotation of the alkanethiol unit cell, and they also all fall on a circle in the sample frame of reference, so we can use this set of six features in the second pass of DHCT for each feature instead of that feature's nearest neighbors. The only other change in the second-pass correction is that we use four times $r_0$ for the radius of the circle in the sample frame. With this small change, the second pass of DHCT corrects for the alkanethiol SAM lattice. We use this two-pass method as the foundation for lattice fitting of alkanethiol SAM images, while graphite images use only one pass of DHCT before lattice fitting.

### 4.2. Lattice Fitting

Determining the best-fit lattice to the surface structure is required for many subsequent analyses of the image. We have considered two different approaches to calculating a best-fit lattice. We will refer to these two approaches as top-down and bottom-up. The top-down approach begins with a guess of the lattice parameters. Using the parameter guess, a corresponding lattice is generated and then compared to the image feature locations. The comparison result is used to improve the guess, then the whole process is repeated until the guess has converged to the best-fit lattice to the data. The bottom-up approach starts by assigning a lattice site to one feature. The lattice is then grown from the single assigned site by searching for unassigned features that are within one nearest neighbor distance of the feature(s) assigned in the previous step. Each newly-found feature is assigned to a lattice site based on its relative location to the assigned feature that was used to find it.

Compared with the top-down approach, this bottom-up approach is much more robust to small systematic errors in the lattice, like those from piezoelectric actuator nonlinearities, thermal drift, or strain. This advantage is less useful in images that have DHCT applied to them, since DHCT compensates for these errors by correcting the distortion. The bottom-up approach was ultimately decided against because it was more susceptible to larger random errors. If a point defect in an image (e.g. a missing or substituted feature) causes the software to assign even one feature incorrectly, each feature assigned by comparing to that feature was also incorrect. The top-down approach is insensitive to these point defects. We have decided to use the top-down approach for the lattice fitting in this work. A promising direction for future improvement would be to somehow consider both techniques simultaneously, using each technique's strength to compensate for the other's weakness.

We use continuous regions of the masks defined earlier that cover one crystal domain and fit the feature locations selected by that mask to 5 parameters: the origin of the lattice ($x_0$, $y_0$); the angle of the first lattice vector from the $x$ axis $\theta$; and a scaling factor in the $x$ and $y$ directions that allows the lattice to fit. If two images were supplied, e.g. a trace-retrace pair, a small offset ($\Delta x$, $\Delta y$) is needed between images to allow the identical features to line up. To avoid becoming trapped in a local minimum, our lattice fitting procedure requires the fit region of the image to agree with the initial-guess lattice to better than one half of the lattice constant over the whole region before fitting. For a 25 nm × 25 nm image of graphite, the accuracy needs to be better than 0.5 × 246 pm (better than 0.5%).

To perform the top-down lattice fit, we start by calculating guesses for the 5 parameters described above. The lattice angle is guessed by finding the peaks of the angular distribution function of NNs (Figure 4.1). A correction factor in x and y calculated from the average of the residual distortion parameters is generated and used as the x and y scaling factor guesses. The (x, y) pixel location of the maximum of the cross-correlation between the trace and retrace image is used for the (x, y) offset guess. (0, 0) is used as the guess for the lattice origin. Next, the lattice parameters are optimized. A lattice is generated from the lattice parameter guess. Each image feature is assigned to the nearest lattice site, and the lattice parameters are tuned to minimize the

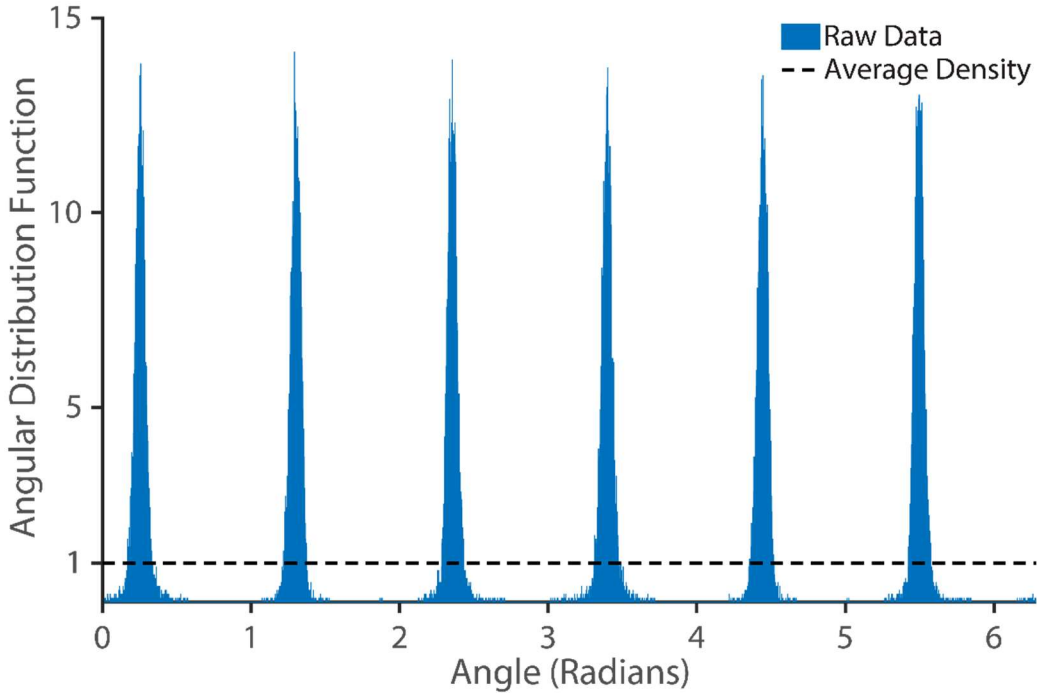


**FIG. 4.1.** Angular distribution function of the nearest neighbors in distortion corrected STM image of graphite.

rms distance between the image features and the lattice. The tuned lattice parameters are saved as a new, better guess. More features should be assigned to the correct lattice sites on the next pass. The process of generating a lattice and improving the guess is repeated until the success condition is met, which happens when the lattice parameters don't change by more than one part in $10^4$

between optimizations. Once the lattice fit converges, each feature is assigned two lattice parameters from the fit; integers that indicate how many lattice vectors the feature is away from the origin. This technique works well when a majority of the features are assigned to the correct lattice site on the initial lattice guess. If the fit does not converge, manually tuning the lattice parameter guesses can usually improve the guess quality enough that the fit converges.

For analysis of unit cell structure instead of surface structure, we use a lattice enforcement rather than a simple fitting. The lattice fit from above is used as a starting point to generate the lattice sites corresponding with each image feature. A least-squares fitting of the data to the lattice is then performed, but the lattice generated by the previous lattice fit is assumed instead of generating the lattice from the parameter guess. Both the $x$ and $y$ coordinates of the data are simultaneously modified to fit the lattice. ($x'$, $y'$) are calculated using the following two-dimensional third-order polynomials:

$$x' = a_x + b_x x + c_x y + d_x x^2 + e_x xy + f_x y^2 + g_x x^3 + h_x x^2 y + i_x xy^2 + j_x y^3 \qquad (4.1)$$

$$y' = a_y + b_y x + c_y y + d_y x^2 + e_y xy + f_y y^2 + g_y x^3 + h_y x^2 y + i_y xy^2 + j_y y^3 \qquad (4.2)$$

The coefficients *a-j* for both $x'$ and $y'$ minimize the rms distance between ($x'$, $y'$) and the location of the assigned lattice site for all features simultaneously. This enforcement step takes advantage of the whole lattice, which dramatically improves long-range order of the image. This

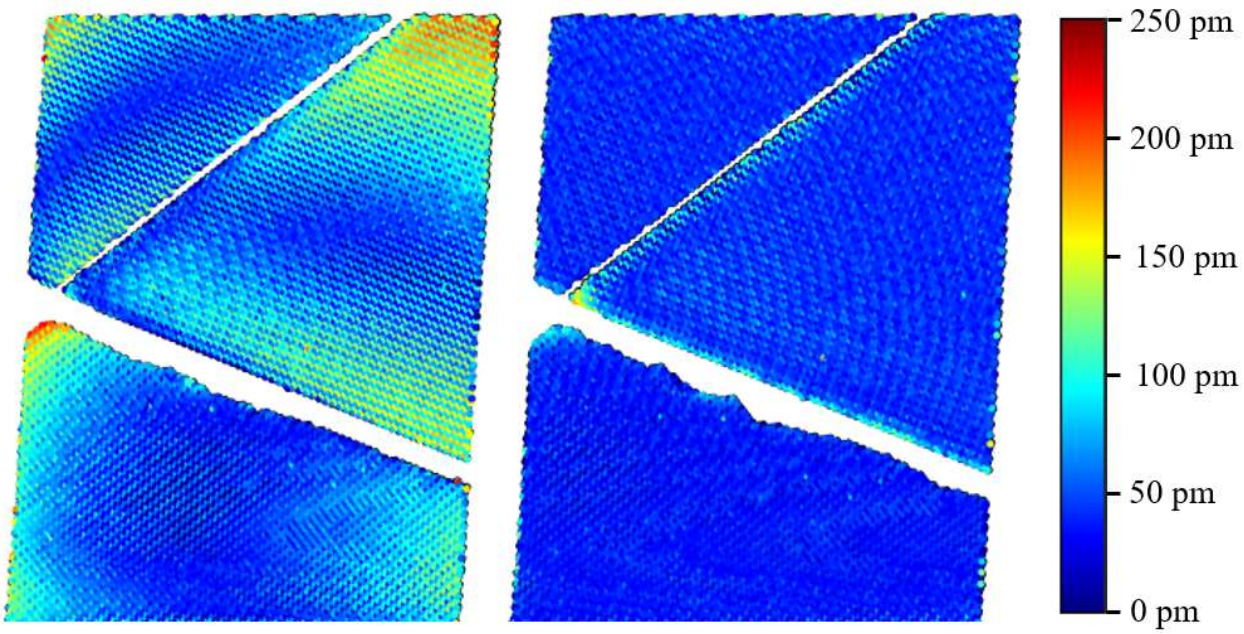


**FIG. 4.2.** Heat map of the deviation of features from their whole-image best-fit lattice sites to the 50 nm × 50 nm distortion corrected STM image of alkanethiol SAM shown in Figure 6.4. (left) DHCT applied and additional linear correction. (right) DHCT applied and additional third-order polynomial lattice enforcement.

is ideal for measuring properties of the surface unit cell. When impeccable long-range order is not required, this step can be simply skipped.

Now registered to a lattice, we can determine how each feature's location is related to each other feature's location, how well each feature's location agrees with the whole-image best-fit lattice, and a variety of other useful measurements. Figure 4.2 shows a heat map of the magnitude of the deviation of each feature's location from its whole-image best-fit lattice site.

### 4.2. Averaged Unit Cell Images

The profiles of atoms and molecules in samples imaged by STM can be obscured by probe-tip fluctuations and by electronic noise. This is particularly true with room-temperature STM imaging, where smaller raster-scan sizes with high-pixel density are not practical, in contrast to imaging with low-temperature ultra-stable STMs. Images that are simultaneously small, slow, and

high-resolution are severely impacted by thermal drift and creep in a way that is likely too dramatic to correct. Instead, imaging many unit cells at low resolution affords the opportunity to combine the measurements from each unit cell into to an averaged unit cell image. The room temperature graphite image in Figure 3.3 contains 11,372 unit cells, with ~350 pixels per unit cell in the original image. The large number of low-pixel density unit cell images can be averaged together to create a high-resolution translationally averaged unit cell image. This is possible after accurate distortion correction using DHCT and lattice fitting to identify the boundaries of each unit cell in the image. Subsets of the unit cells can also be selected. The location, height, and shape characteristics of each image feature can be used to select the unit cells that are averaged, e.g. the average of unit cells with presence or absence of a certain defect. Averaged unit cell images have proven useful for analysis of STM images of a variety of materials.[1-3]

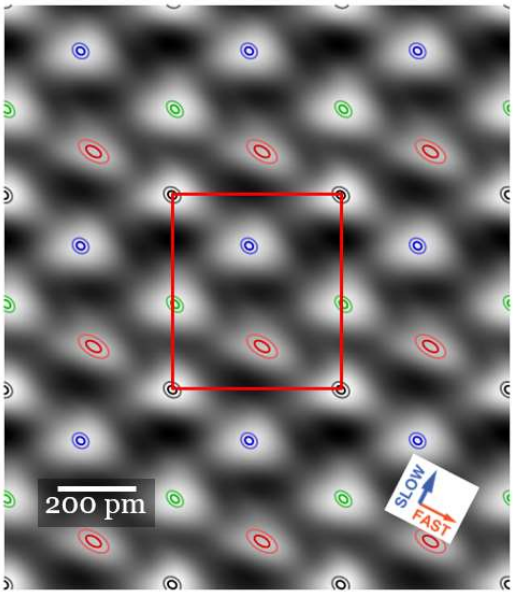


**FIG. 4.3.** Translationally averaged unit cell image for terminal methyl groups on the alkanethiol SAM surface from Figure 6.2 (grayscale image) with the surface unit cell (outlined in red) and 1σ and 2σ confidence intervals of atom locations (outlined in 4 colors, one per basis) overlaid.

An example of an averaged unit cell image of an alkanethiol SAM is displayed in Figure 4.3 as the grayscale image. Several averaged unit cell images are tiled in Figure 4.3 for ease of visualization and to demonstrate that the boundaries stitch together without discontinuities. One of the unit cells is outlined. After choosing a set of surface unit cells to average, the unit cells are sampled into an appropriately sized grid via a linear transformation of the part of the image that contains the unit cell. The cells are then simply averaged together.

### 4.4. Feature Confidence Ellipsoids

The image features do not fall perfectly on their best-fit lattice site but are instead distributed around that site. This is the aggregate effect of intrinsic disorder in the molecules along with residual distortion left after DHCT due to higher-order thermal-drift, hysteresis, and creep effects or lattice fitting mismatch; noise in the STM due to the current amplifier, control electronics, and analog to digital converter; noise due to probe-tip fluctuations; and environmental noise from vibration. The 1σ and 2σ in-plane confidence ellipses are overlaid on the averaged unit cell image in Figure 4.3. The corresponding uncertainties vary from ±7.5 pm for the short axis of the molecule colored in green to ±20 pm for the long axis of the molecule colored in red.

### 4.5. Symmetry-Averaged Unit Cell Images

In addition to the translational symmetry that defines the surface unit cell, many structures have additional symmetry. Graphite(0001)'s surface unit cell has p3m1 symmetry. The

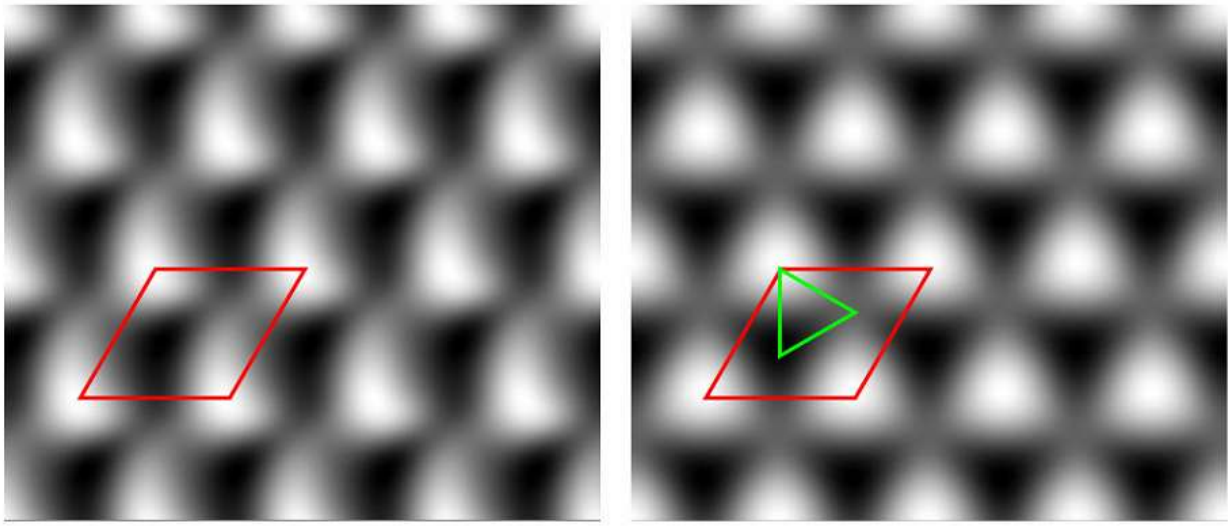

**FIG. 4.4.** (left) Translationally averaged unit cell of the graphite image from Figure 3.4 with the surface unit cell (outlined in red) overlaid. (right) Symmetry-averaged unit cell from the same image with the surface unit cell (outlined in red) and asymmetric unit (outlined in green) overlaid. In addition to translational averaging, this unit cell was also averaged over rotations by 120° about the 3-fold rotation axes and reflection about the mirror plane. Averaging the image this way ensures that the unit cell has the same symmetry as the lattice that generated it.

translationally averaged images exhibit a lower symmetry than expected for graphite due to convolution with a probe-tip profile that has a different symmetry. The additional step of averaging over the unit cell's symmetry (e.g. rotations and reflections), enforces the symmetry of the surface unit cell (Figure 4.4). Symmetry averaging also smooths over image artifacts with different symmetry, e.g. the probe-tip profile.

### 4.6. Time Series Lattice Alignment

Spatially averaged unit cells work very well for large, pure crystals, where a spatial translation gives a very high likelihood of reaching a symmetry-equivalent point in the structure. For studying other things, like surface defects, boundaries, adsorbed molecules, and other non-crystalline features of the surface, the best way to get more measurements of them is to watch them evolve with time. The drift rate of STM is low enough to image the same area for hours or days at a time, given that the tip is sufficiently stable. Even with relatively high sample drift, repeated images of the same area can be taken using e.g. a cross-correlation of a notable image defect, or even manual image realignment by the STM operator. After image correction, images of the same area can have their lattices matched. The first image in the time series is used as the reference, with the other images aligned to its lattice.

DHCT can introduce small rotations due to neglecting the fast-scan component of the image correction. We assume that the local affine transformations have a vertical shear component of exactly 0, despite acknowledging that there is a small effect of thermal drift and piezoelectric actuator creep in that direction. It is always possible to choose a rotation of an affine transformation that makes the vertical shear component 0. Consider an arbitrary 2D affine transformation transforming a set of coordinates $(x, y)$ to a different set $(x', y')$:

$$\begin{pmatrix} x' \\ y' \end{pmatrix} = \begin{pmatrix} 1+S_x & T_{xy} \\ T_{yx} & 1+S_y \end{pmatrix} \begin{pmatrix} x \\ y \end{pmatrix} \tag{4.3}$$

We can rotate the primed coordinates to get ($x''$, $y''$):

$$\begin{pmatrix} x'' \\ y'' \end{pmatrix} = \begin{pmatrix} \cos\theta & -\sin\theta \\ \sin\theta & \cos\theta \end{pmatrix} \begin{pmatrix} x' \\ y' \end{pmatrix} = \begin{pmatrix} \cos\theta & -\sin\theta \\ \sin\theta & \cos\theta \end{pmatrix} \begin{pmatrix} 1+S_x & T_{xy} \\ T_{yx} & 1+S_y \end{pmatrix} \begin{pmatrix} x \\ y \end{pmatrix} \tag{4.4}$$

Expanding:

$$\begin{pmatrix} x'' \\ y'' \end{pmatrix} = \begin{pmatrix} (1+S_x)\cos\theta - T_{yx}\sin\theta & T_{xy}\cos\theta - (1+S_y)\sin\theta \\ (1+S_x)\sin\theta + T_{yx}\cos\theta & T_{xy}\sin\theta + (1+S_y)\cos\theta \end{pmatrix} \begin{pmatrix} x \\ y \end{pmatrix} \tag{4.5}$$

This is a different affine transformation.

$$\begin{pmatrix} (1+S_x)\cos\theta - T_{yx}\sin\theta & T_{xy}\cos\theta - (1+S_y)\sin\theta \\ (1+S_x)\sin\theta + T_{yx}\cos\theta & T_{xy}\sin\theta + (1+S_y)\cos\theta \end{pmatrix} = \begin{pmatrix} 1+S_x' & T_{xy}' \\ T_{yx}' & 1+S_y' \end{pmatrix} \tag{4.6}$$

We choose $\theta$ such that $T_{yx}' = 0$:

$$(1+S_x)\sin\theta + T_{yx}\cos\theta = 0 \tag{4.7}$$

Solving for $\theta$:

$$\theta = \tan^{-1}\left(\frac{-T_{yx}}{1+S_x}\right) \tag{4.8}$$

$\theta$ is well-defined for all values of $T_{yx}$ and $S_x$. Choosing a vertical shear component of 0 in DHCT is equivalent to finding the affine transformation that corrects everything including the vertical shear, and then rotating the resulting image so that there is no longer a vertical shear. Since there is no absolute rotational reference in a STM image, this also solves the degeneracy of choosing an arbitrary rotation when solving for the general affine distortion. When comparing multiple images in a sequence, DHCT is unlikely to rotate all images the same way, so we must rotate the images such that their lattices align. All images, after the first one, are rotated by the difference in lattice

angles between the first image and the current image. The rotation is expected to be small because the scan window was not intentionally rotated in between frames and the vertical distortion components are much smaller than the horizontal ones.

After rotations, the images are aligned to the nearest pixel by using a cross-correlation to find the offset between the first image and each other image. The lattice is then matched to the first image by relabeling all the lattice sites using the first lattice's origin. With a lattice matching, a more accurate subpixel lattice matching can be attained by translating the lattices in each image on top of one another. The final rotation and translation can be applied to the images and data calculated from them for future processing. One obvious use of aligned images that we implemented is showing the images in a movie. A movie generated from 22 images acquired over 8 hours can be seen at https://shareok.org/handle/11244/325371.

### 4.7. Data Visualization – 2D Correlation Plots

The alkanethiol SAM surface unit cell has 4 molecules in different basis sites, but the structure is close to a one-molecule-basis lattice.[4-7] The 2D correlation plot demonstrated in Figure 4.5 allows us to easily visualize the SAM's 4-molecule-basis lattice from STM image data. In the 2D correlation plot, distances between pairs of features

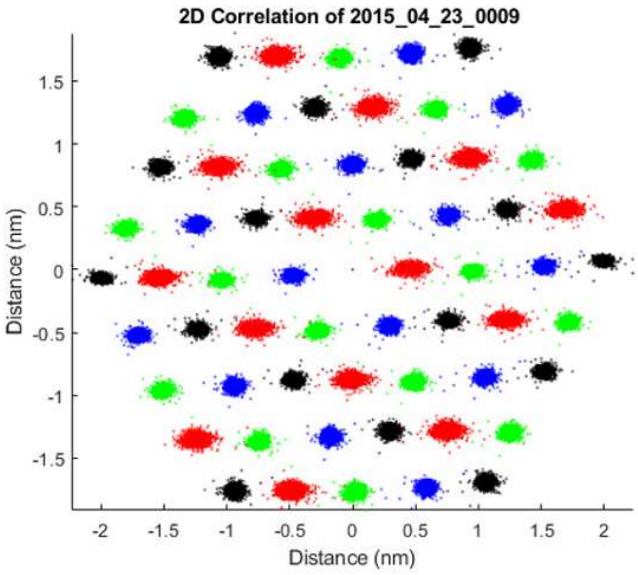


**FIG. 4.5.** 2D correlation plot (cloud plot), generated from the image shown in Figure 6.2, of distances from each feature from one basis site (black-colored molecules) to each other feature. The 4 basis sites are colored in 4 different colors. Each of the clouds has a distinctly different shape, which demonstrates the 4-molecule-basis of the surface structure.

are plotted. Figure 4.5 shows the spacing in an alkanethiol SAM image between every molecule at the corner of the unit cell (colored black in Figure 4.3) and every other molecule within 4 nearest neighbor spacings of it. These spacings tend to form clusters in the plot by basis type. The clusters have been colored differently by basis for clarity, but the shape formed by the cloud is distinctly different for each of the 4 basis sites. If the wrong basis is chosen (e.g. incorrect rotation), the basis clustering will appear multimodal, since each basis contributes its own cloud shape.

### 4.8. Data Visualization – Reduced Close-Packed Coordinate Frame

Comparing alkanethiol SAM surface structures was more difficult than we expected. While each of the alkanethiol SAM images we acquired had a $(2\sqrt{3} \times 3)$rect. unit cell, the positions of the features within the cells rarely aligned between different sets of images. Here, two structures are said to be aligned if both structures have their molecules in the same locations in the surface unit cell. It is possible that structures would not align due to fundamental differences between the images we're comparing (e.g. each image contains a different structural phase), but it is also possible that the images differed only by a rotation or translation. Dealing with each of these problems separately is simple. For multiple different structural phases, carefully comparing the images would let us classify each phase and analyze the phases independently. For images of identical structures that could be aligned with a simple lattice transformation, comparing the images would let us determine and apply the transformation that aligns them. Because our images had unknown structure, we needed a more robust solution that could solve both problems. Our goal was to design a method that would be able to simultaneously align and classify structures so that they can be appropriately compared.

The alkanethiol SAM unit cell is quite nonsymmetric. Its only symmetries are the translational symmetries of its lattice vectors and c1 symmetry (rotation by 360 degrees), the minimum possible set of symmetries for a lattice. There are several operations that preserve the unit cell shape and approximate basis site locations of the alkanethiol SAM 4-molecule-basis lattice, but not it's structure. We will refer to these operations as near-miss symmetry operations. The near-miss symmetry operations of the 4-molecule-basis unit cell are rotation by 180° and translation by the lattice vectors of the $(\sqrt{3} \times \sqrt{3})R30°$ sublattice. Two identical structures that differ by a near-miss symmetry operation would not align when compared, but the alignment can

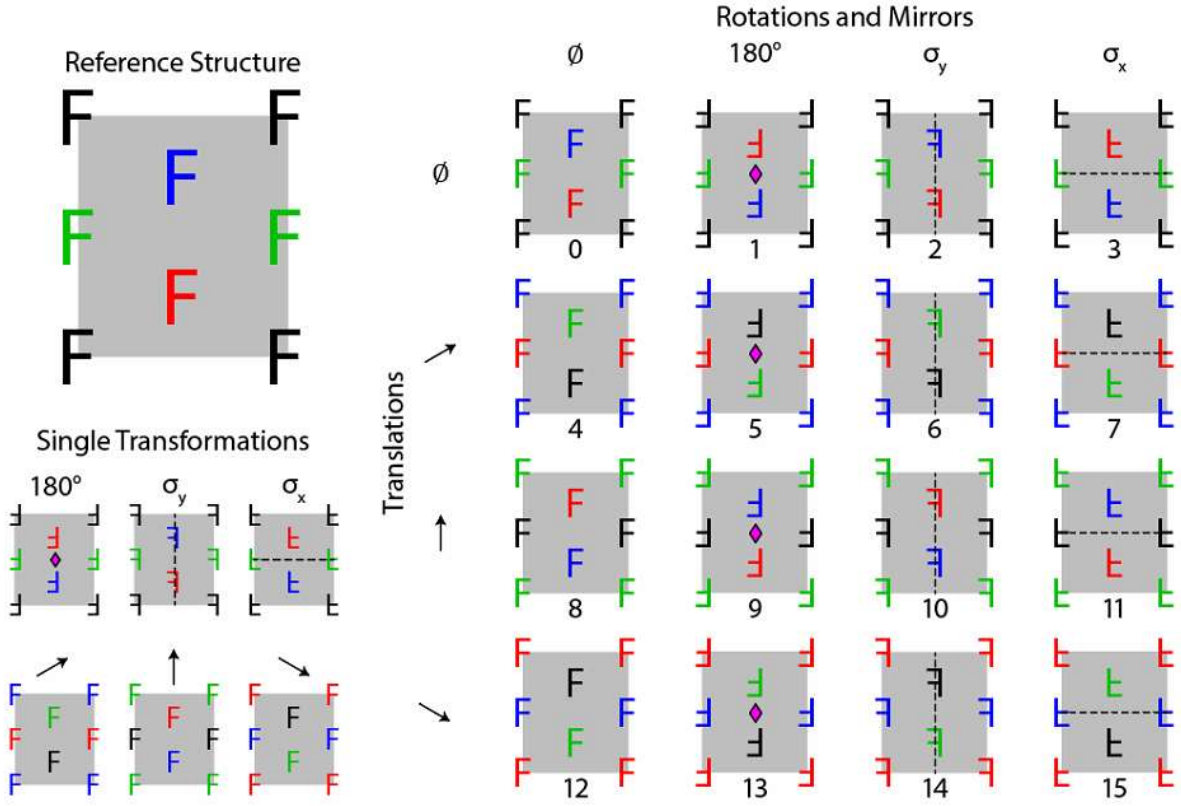


**FIG. 4.6.** (top left) An asymmetric reference $(2\sqrt{3} \times 3)$rect. unit cell. Features colored by basis type and labeled with the letter F due to its lack of point-group symmetries other than c1. (bottom left) Definitions for the six single transformations that compose the near-miss symmetry operations. The transformations are rotation by 180° (about the rotation center indicated with the diamond), $\sigma_y$ and $\sigma_x$ (mirroring about the mirror plane indicated with the dashed line), and 3 translations by $\sqrt{3}$ a = 4.99 Å (along the direction indicated by the arrow). (right) Table of all possible compositions of transformations that result in unique near-miss symmetry operations. The operations are labeled 0-15.

be restored by application of a correctly chosen operation to one of the images. By contrast, there is no symmetry operation that will align two different structures – if there was, they would not be different structures. $\sigma_x$ and $\sigma_y$ behave similarly to a near-miss symmetry, with one important difference – two structures that differ by only a mirror plane are known as enantiomers, which are different structures. We are interested in finding these if they exist, so we have included $\sigma_x$ and $\sigma_y$ in our list of near-miss symmetries. Note that $\sigma_x$ is simply a composition of $\sigma_y$ and a rotation by 180 degrees. Figure 4.6 shows all 16 of the possible combinations of near-miss symmetry operations for an asymmetric $(2\sqrt{3} \times 3)$rect. unit cell. Applying these operations to a structure can change how it aligns with other structures, but leaves the structure intact up to a mirror plane.

We use the reduced close-packed (RCP) coordinate frame to visualize the differences between $(2\sqrt{3} \times 3)$rect. unit cells. The RCP coordinate frame was described by Bhattacharya, et al. in their molecular dynamics study of alkanethiol SAMs.[8] Plots in the RCP coordinate frame

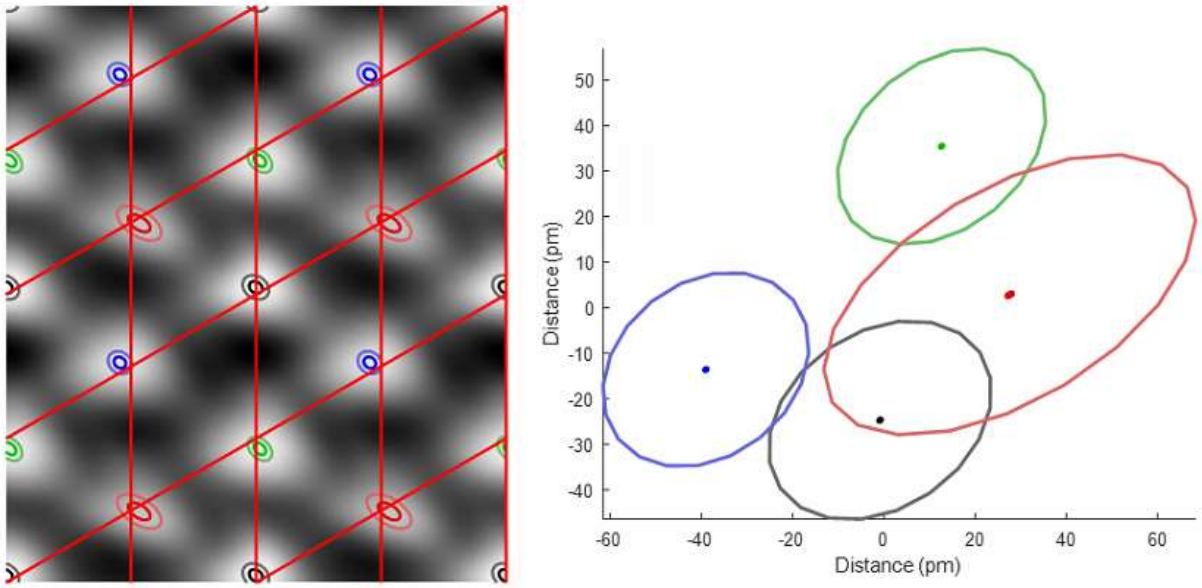


**FIG. 4.7.** (left) Surface average unit cell and 2D location confidence intervals generated from the corrected STM image of a decanethiol SAM shown in Figure 6.2. A one-molecule lattice is overlaid. (right) the RCP coordinate frame plot generated from the figure on the left. The large ellipse is the $1\sigma$ ellipse from the left figure, the smaller ellipse is $1\sigma_m$. Their position is the offset from the one molecule lattice sites, indicated by the crossing of the red lines in the left figure.

can be generated by subtracting a $(\sqrt{3} \times \sqrt{3})R30°$ sublattice from the $(2\sqrt{3} \times 3)$rect. unit cell. An example is shown in Figure 4.7. The large ellipses in the RCP coordinate frame plot are the 1σ location confidence ellipses, and the small ellipses are $1\sigma_m$ from the same measurement. RCP coordinate frame plots of the 4 molecule location confidence ellipses can be more easily distinguished than the full unit cell under near-miss symmetry operations.

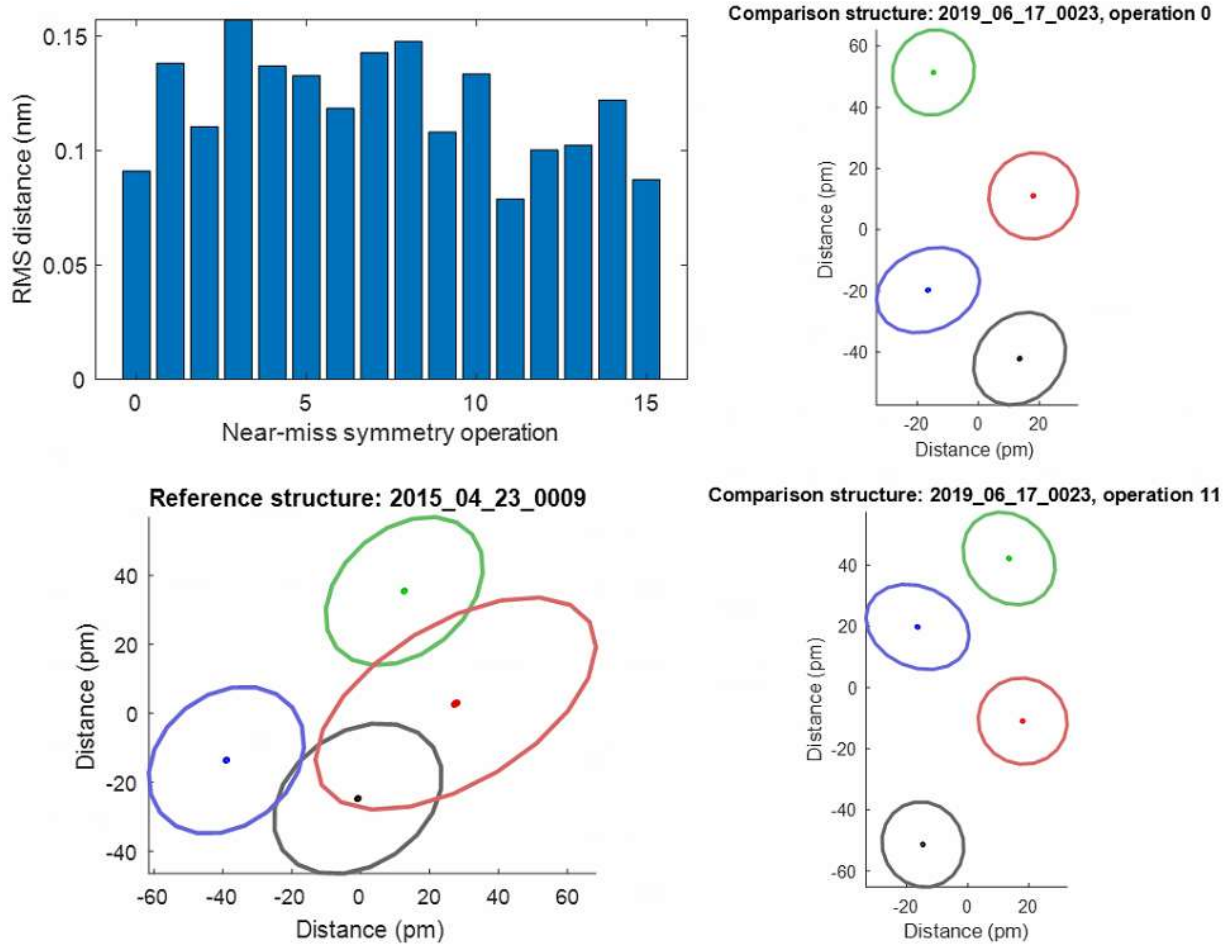


**FIG. 4.8.** (top left) Bar chart of RMS distance between the reference structure and the structures that result from applying each of the near-miss symmetry operations (labeled 0 through 15 in Figure 4.6) to the comparison structure. (bottom left) RCP coordinate frame plot from 2015_04_23_0009, chosen as the reference structure. (top right) RCP coordinate frame plot for 2019_06_17_0023, the comparison structure. (bottom right) The structure closest to the reference structure, obtained by applying operation 11 to the comparison structure. This structure is still not very close to the reference structure.

Our method for comparing RCP coordinate frame plots uses one of the plot's mean ($x$, $y$, $z$) feature locations as the reference structure. Before generating the next plot, all 16 near-miss symmetries are applied to the mean ($x$, $y$, $z$) feature locations for the next data set, generating 16 structures to test against. We calculate the rms distance between the reference structure and each of the 16 calculated structures, calculating a score for each. Lower scores indicate two structures being more similar. A pair of aligned RCP coordinate frame plots and the score bar chart used to align them can be seen in Figure 4.8. Two structures that are the same, or an enantiomeric pair of structures, will be very close to each other when the near-miss symmetry that correctly aligns them is applied, while different structures will not be particularly close under any of the near-miss symmetry operations and can be classified as different.. The results of the RCP coordinate frame comparisons we have done so far can be found in Section 6.4.

### 4.9. References

1. J. F. Jorgensen, L. L. Madsen, J. Garnaes, K. Carneiro and K. Schaumburg, J. Vac. Sci. Technol. B **12** (3), 1698-1701 (1994).
2. I. Zeljkovic, E. J. Main, T. L. Williams, M. C. Boyer, K. Chatterjee, W. D. Wise, Y. Yin, M. Zech, A. Pivonka, T. Kondo, T. Takeuchi, H. Ikuta, J. Wen, Z. Xu, G. D. Gu, E. W. Hudson and J. E. Hoffman, Nat. Mater. **11** (7), 585-589 (2012).
3. M. J. Lawler, K. Fujita, J. Lee, A. R. Schmidt, Y. Kohsaka, C. K. Kim, H. Eisaki, S. Uchida, J. C. Davis, J. P. Sethna and E. A. Kim, Nature **466** (7304), 347-351 (2010).
4. A. Cossaro, R. Mazzarello, R. Rousseau, L. Casalis, A. Verdini, A. Kohlmeyer, L. Floreano, S. Scandolo, A. Morgante, M. L. Klein and G. Scoles, Science **321** (5891), 943-946 (2008).
5. P. Fenter, P. Eisenberger and K. S. Liang, Phys. Rev. Lett. **70** (16), 2447 (1993).
6. N. Camillone III, C. E. D. Chidsey, P. Eisenberger, P. Fenter, J. Li, K. S. Liang, G. Y. Liu and G. Scoles, J. Chem. Phys. **99** (1), 744-747 (1993).
7. G. E. Poirier and M. J. Tarlov, Langmuir **10** (9), 2853-2856 (1994).
8. S. Bhattacharya, M. P. Yothers, L. Huang and L. A. Bumm, ACS Omega **5** (23), 13802-13812 (2020).

# Chapter 5
# Height Analysis: Tools and Results

Height measurements with the STM are intrinsically more accurate than in-plane measurements. The negative feedback loop that controls the STM tip's height allows closed-loop control, which allows more accurate positioning than the open-loop system that controls the STM tip's horizontal position. However, the STM is used almost exclusively to measure atomically flat surfaces, because they introduce the minimum amount of additional constraints on the feedback loop response and tip sharpness. Our STM uses a state-of-the-art amplifier to measure pA tunneling currents at kHz frequencies, and we use atomically sharp tips already – measuring rougher samples puts even higher constraints on these already highly constrained parts of the instrument. The biggest limitations on height measurement of atomically flat STM samples are calibration and plane subtraction. Fogarty, et al. describe the technique of plane subtraction well, and their tool for plane subtraction is effective.[1] We have used their tool as a prerequisite for DHCT. Calibration can be easily performed using substrate features with well-known heights. We use gold atomic steps from the Au(111) surface to calibrate the height in our STM images, which is known to be 2.35 Å.[2] This height is derived from the geometry of the Au face centered cubic (fcc) unit cell. Once plane subtracted and calibrated, height measurements can be made using image cross-sections.[3, 4] In a cross-section, a line is plotted on a STM image and the height of the image vs. distance along the line is plotted in a chart. The cross-section method has been applied to images of alkanethiol SAMs to determine their properties.[5] There are two ways of acquiring data for a cross-section plot. The simpler way is to use the measurements already recorded in the STM image—simply sample the nearest points to the line from the image data to generate any cross-section plot. Alternately, new data can be acquired by the STM itself by collecting data as it

scans along a desired line. Both methods are prone to error in different ways, but generally allow for high quality measurements of data along the line.

In this section, we show our height measurement methodology, which we believe is an improvement to the traditional measurement from image cross sections. We then show some height measurement results we have obtained, which include some results that seem to be high quality but have anomalously high corrugation. Finally, we introduce a model for generating STM images of SAMs that we have been using to try to understand the height measurements we have observed in our experiments.

### 5.1. Height Measurement Methodology

While DHCT does not correct STM image feature's heights, the technique allows for measurements that sample from the whole surface. When compared with cross-section plots, the much higher sampling rate allows us to use averaging to reduce the noise floor of our measurement.

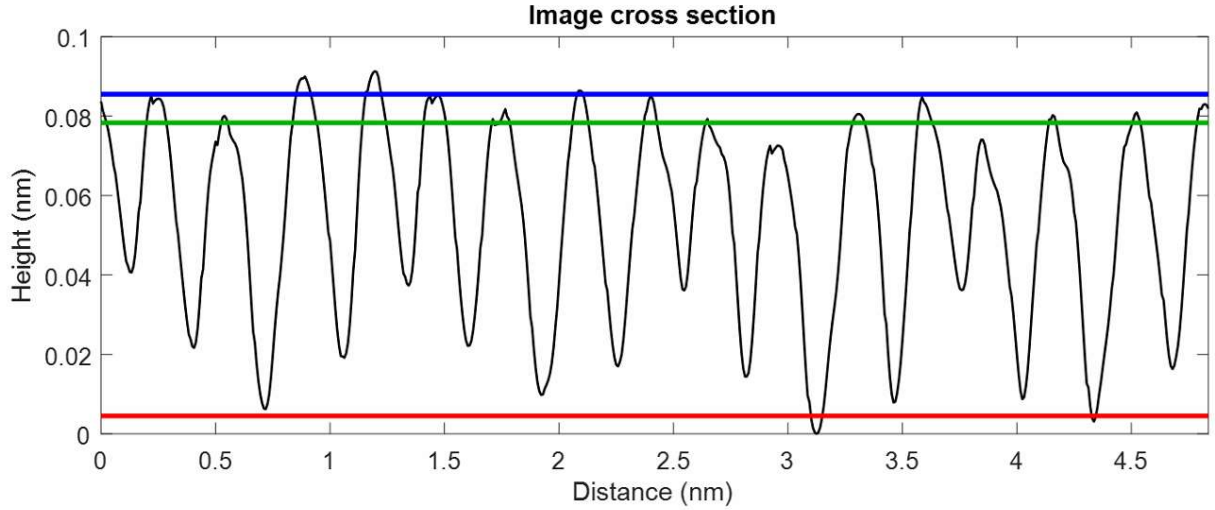


**FIG. 5.1.** Plot of molecular corrugation along a cross-section of Figure 6.4 (in black). Plotted as horizontal lines are the average height of the lowest point (in red), the average height of the top of the lowest feature (in green), and the average height of the top of the highest feature (in blue). The image corrugation is the difference in height between the red and blue lines, while the feature height difference is the difference in height between the green and blue lines.

One method of measuring height is to calculate the height difference between the high point and low point of the spatially averaged data. We will refer to this kind of measurement in this work as image corrugation. With averaged unit cells created by DHCT, we can quickly calculate an image corrugation from the averaged unit cell by measuring the height difference between the high and low points. Another way of measuring the height from the surface is to calculate the height difference between the tops of the highest and lowest features within the spatially averaged data. We call this kind of measurement the feature height difference. This measurement can be calculated from an image cross-section, but it is not guaranteed to be possible to draw a line that contains the peak locations for a 4-molecule-basis lattice. While we have observed that the 4-molecule-basis peaks are not colinear, this has not stopped researchers from using cross-section plots to study SAMs. By using the feature heights calculated from DHCT, this concern is completely avoided.

An example of how the image corrugation and feature height difference are calculated for an image cross section can be seen in Figure 5.1. Our technique for measuring image corrugation and feature height difference are analogous to this, they are only different by considering the whole image rather than only a cross-section.

For the feature height difference, the tops of the features were chosen because we believe the tops of the image features are the least sensitive to tip artifacts. STM images are convolutions of the physical and electronic properties of both the tip and the sample.[6] Models for calculating a STM image for a given surface topography are well understood and thoroughly tested, but the reverse problem is quite difficult. The STM is known to be excellent at imaging flat, homogeneous samples. This made us theorize that the most accurate image of the surface occurs where the STM

image gradient is minimized, which would occur when the surface is maximally flat and homogeneous, directly above the top of a molecule.

### 5.2. Height Measurement Results

While compiling these results, we noticed a surprising change in the molecular height difference of the alkanethiol SAM images we analyzed. A plot of molecular height difference vs. image corrugation for 37 of our best C10 images can be seen in Figure 5.2. The cluster of 9 images acquired on June 17, 2019 (blue in the figure) have anomalously high image corrugation and molecular height difference. We had predicted that the molecule height difference would not be affected by tip artifacts for well-resolved images. Because we were not able to justify the observed differences, we set out to create a model that would help us to better understand the system. Our goal for the model was to better understand how tip artifacts affect STM images. We hope to determine whether this plot is consistent with different tip artifacts on a single structure or if it requires multiple structures to explain.

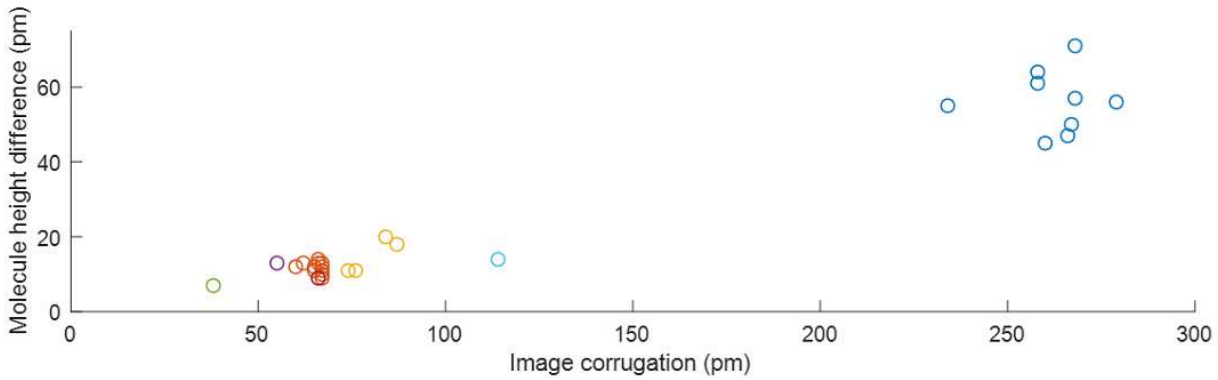


**FIG. 5.2.** Plot of molecular height difference vs. image corrugation for 37 of our best 300 K, –1 V sample bias, 1 pA tunneling current, C10 SAM images. Images acquired on the same day are plotted with the same color. Purple: 2015_03_03, Green: 2015_04_15, Orange: 2015_04_23, Cyan: 2018_04_02, Magenta: 2019_06_12, Blue: 2019_06_17, Yellow: 2019_10_10.

### 5.3. STM Image Simulation Model

The model we chose to implement is an extension of the Bumm, et al. two-layer tunneling model for STM imaging of organic molecules.[3] Recent studies of the mechanism of charge transport through alkanethiol SAMs show evidence that the tunneling path through the SAM follows the bonding in the SAM backbone.[7, 8] Our new model considers this fact by considering the different paths through the vacuum gap to the tops of molecules rather than considering the shortest path to the film as a whole. A schematic diagram of the concept of the two-layer tunnel junction model is shown in Figure 5.3. The STM images we want to model were taken in constant current mode, which is included in the model as a constant total conductance $G_{total}$. The total conductance is the sum of many parallel conductances:

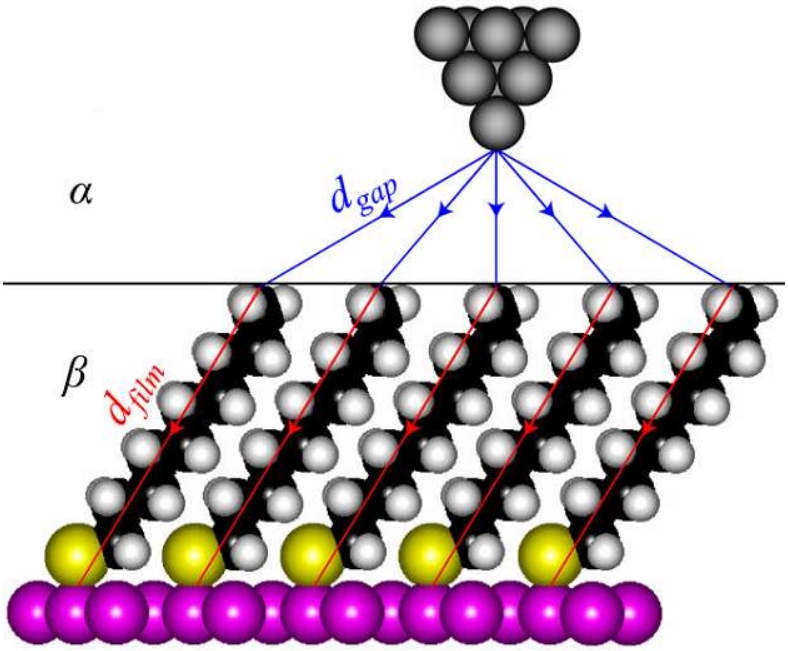


**FIG. 5.3.** Schematic diagram showing how the two-layer tunnel junction model works. Electrons tunnel along a path from the tip of the molecule to the surface. The path goes from the tip to the top of a molecule through a distance $d_{gap}$ with tunneling decay constant $\alpha$, then travels along the bonds of the molecule a distance $d_{film}$ with tunneling decay constant $\beta$.

$$G_{total} = \sum_{paths} G_{contact} P_{tunnel}. \quad (5.1)$$

In this model, $G_{contact}$ is the tip-substrate contact conductance, and $P_{tunnel}$ is the tunneling probability from the tip to the surface through a molecule. Each path is from a tip atom to the top of a molecule, then through that molecule to the substrate. The probability of tunneling along any path is the product of two probabilities,

$$P_{tunnel} = P_{gap}P_{film}. \tag{5.2}$$

The probability of tunneling through the gap depends on the path length through the gap $d_{gap}$ and the decay rate $\alpha$.

$$P_{gap} = e^{\alpha d_{gap}}. \tag{5.3}$$

The path length $d_{gap}$ is not necessarily perpendicular to the surface, it can be in any direction. This is a deviation from the Bumm model. The probability of tunneling through the film is constant for any homogeneous thin film, just like in the Bumm model. Rearranging a bit and pulling out the constant terms, we get the following equation:

$$\frac{G_{total}}{G_{contact}P_{film}} = S = \sum_{paths} e^{\alpha d_{gap}}. \tag{5.4}$$

We have defined $S$ as a unitless constant that combines the effects of $G_{total}$, $G_{contact}$ and $P_{film}$ on the model. $G_{contact}$ and $P_{film}$ are defined by the choice of sample, but $G_{total}$ is defined by the voltage and setpoint current of the STM. Tuning S in this model is analogous to changing the setpoint current of the STM by the same amount. This equation acts as a constraint that allows us to calculate a height $z$ above a thin film surface where the STM tip satisfies the tunneling conditions. By finding the set of $z$ for a grid of points, we can simulate an STM image.

In order to generate an STM image with our model, we start by defining the simulation parameters. The constants $S$ and $\alpha$ are chosen for the simulation, and locations of tip atoms are defined if multiple tip atoms are being considered. We generate a monolayer by defining molecule ends to tunnel to in a unit cell. The unit cell is tiled out to create a surface of the area to be simulated, with at least 5 nm of extra tiling on each edge to minimize edge effects. A set of ($x$, $y$) points to tunnel at are chosen. At each ($x$, $y$) point, we need to find the $z$ such that the tunneling condition is as close to being fulfilled as possible. A grid search with 100 points linearly spaced in

*z* is used to find the *z* where the tunneling probabilities sum to the setpoint. The closest one is selected, and the search is repeated with a finer grid several times to match the height as well as possible.

The software model we implemented has two modes of operation. In the STM simulation mode, high resolution unit cell images are simulated for direct comparison with experiment. This mode is useful for visualizing how changing the parameters affects STM images, e.g. differences between images with single and double tips. An example demonstrating the STM simulation mode can be seen in Figure 5.4. In the grid search mode, image corrugations are calculated with many different choices of setpoint and α to find which combinations give a certain corrugation. This

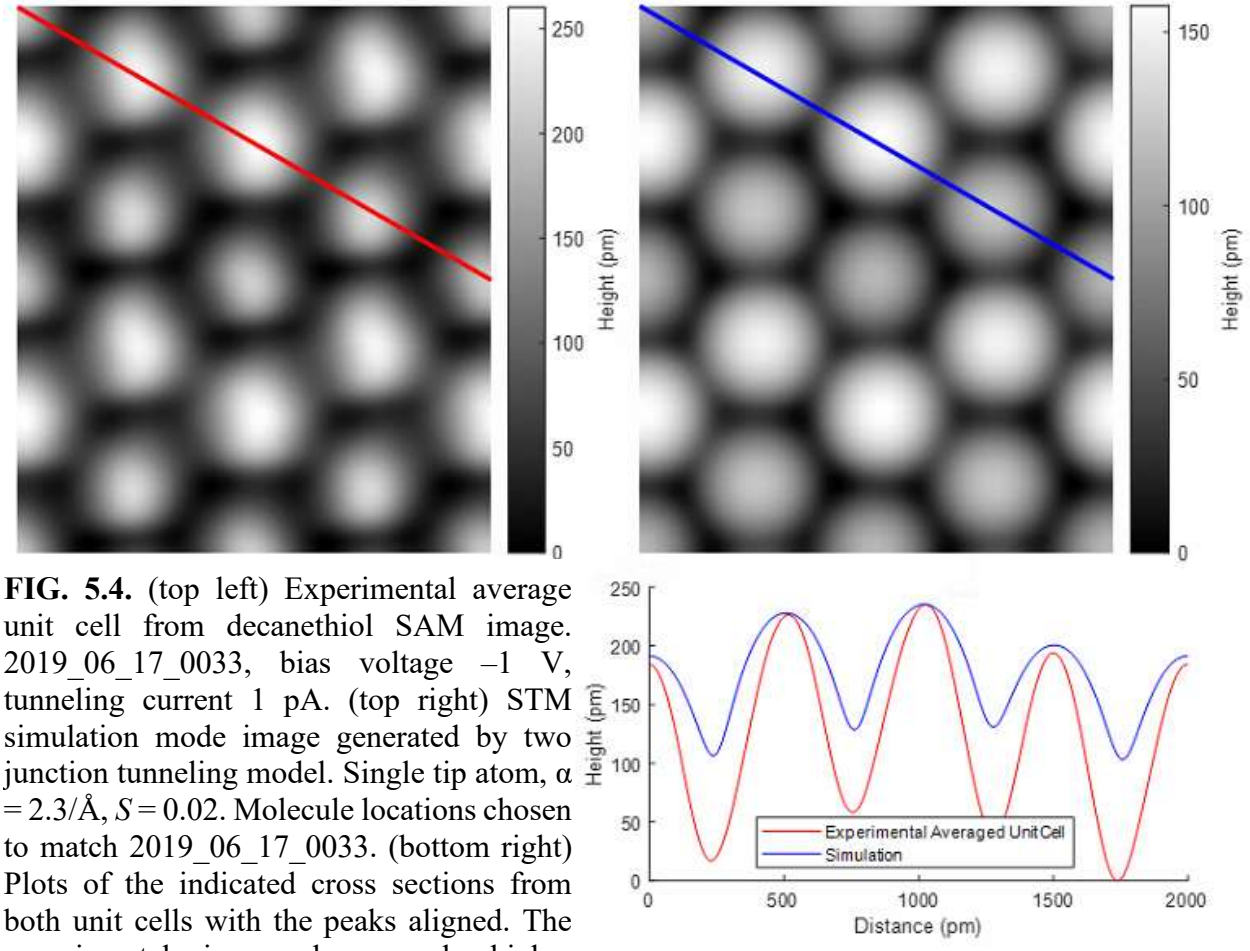


**FIG. 5.4.** (top left) Experimental average unit cell from decanethiol SAM image. 2019_06_17_0033, bias voltage –1 V, tunneling current 1 pA. (top right) STM simulation mode image generated by two junction tunneling model. Single tip atom, α = 2.3/Å, $S = 0.02$. Molecule locations chosen to match 2019_06_17_0033. (bottom right) Plots of the indicated cross sections from both unit cells with the peaks aligned. The experimental image has much higher corrugation.

mode is useful for finding simulation parameters that match experimental results. A corrugation phase space plot generated by this mode can be found in Figure 5.5

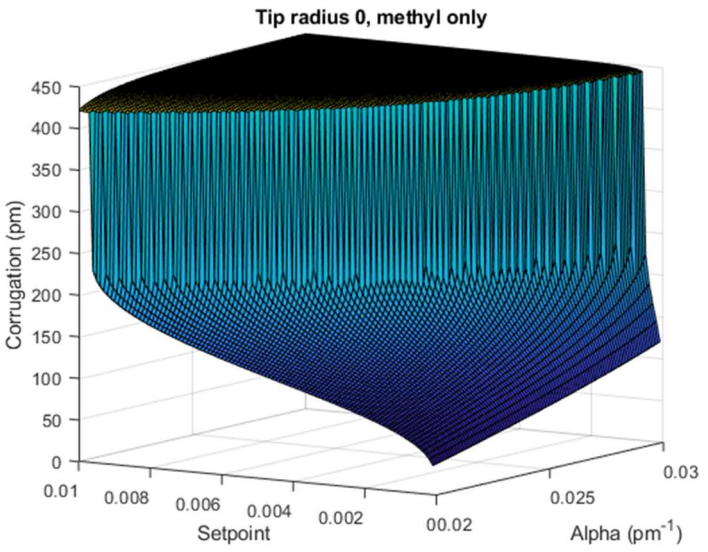


**FIG. 5.5.** Image corrugation phase space plot generated by the two layer tunnel junction model. Single tip atom. One-molecule-basis lattice's high symmetry points are calculated with varying setpoint and α to find sets of parameters that match a given image corrugation. The plateau at 425 nm is an artificial backstop included to capture the vertical asymptote that can be seen at its edge.

We designed a simple experiment to test that our model was working correctly. In most STM images of alkanethiols we acquire, the molecule ends appear higher than the spaces between them. This is explained by Bumm, et al. as a consequence of the lower decay constant for electrons tunneling through the film than the vacuum.[3] If the tunneling current is held constant, the STM height difference is related to the real height difference by the following equation:

$$\Delta h_{stm} = \left(1 - \frac{\beta}{\alpha}\right) \Delta d_{gap}. \tag{5.5}$$

Here, $\beta$ is the tunneling decay rate through the film. If we were to reduce $\alpha$ in our model to be lower than $\beta$, then we would expect $\Delta h_{stm}$ to be negative. We call this contrast inversion. We have occasionally observed inverted contrast in our experimental STM images, so reproducing this phenomenon would be a promising sign for our model.

A plot of image corrugation vs. $\alpha$ is shown in Figure 5.6 that shows contrast inversion in our model. Three $S$ were chosen to represent different tunneling parameter possibilities, with

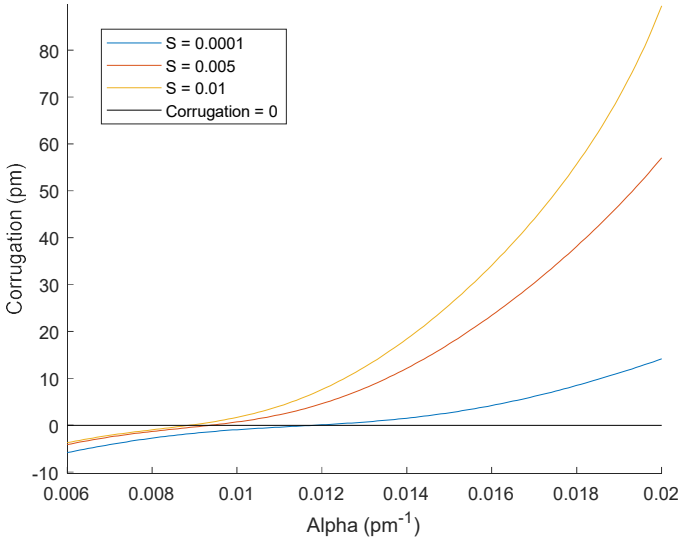


**FIG. 5.6.** Image corrugation phase space plot generated by the two-layer tunnel junction model. Single tip atom. Contrast inversion occurs for $\alpha$ from 0.009-0.012 pm$^{-1}$, depending only slightly on $S$.

magnitudes varied from $10^{-4}$ to $10^{-2}$. Negative corrugation indicative of contrast inversion occurs in Figure 5.6 for $\alpha$ less than 0.009 pm$^{-1}$ at $S$ = 0.01 and for $\alpha$ less than 0.012 pm$^{-1}$ at $S$ = 0.0001. $S$ includes a factor of $P_{film}^{-1}$, and $P_{film}$ depends on $\beta$. For a decanethiol film thickness of 1410 pm, increasing $S$ by a factor of 100 corresponds to decreasing $\beta$ by 0.0033 pm$^{-1}$. Equation 5.5 predicts an equal change in $\alpha$, which is in quite good agreement with our simulated change in $\alpha$ of around 0.003 pm$^{-1}$. If we consider our prediction of inverted contrast for $\alpha < \beta$ and Sachs, et al.'s measurement of $\beta$ through alkane chains[9] of 0.009 ± 0.001 pm$^{-1}$, we see that our model reproduces contrast inversion in accordance with our expectations.

We have recently begun the process of exploring this model to see what can be learned from it. As we originally suspected, the position of the top of the molecule and the molecule height difference in simulated averaged unit cell images agrees with the input molecule positions for all tested single-atom tips, and appears to be nearly independent of $\alpha$ and $S$. Multiple atom tips have not yet been thoroughly explored, but our results so far show that multiple atom tips can be designed to significantly modify the molecule height differences, or positions, or both. The image corrugation is quite sensitive to changes in $\alpha$ and $S$ for all tips. Since multiple atom tips can change the molecule height differences and positions, it is possible that the multiple structural phases

observed by STM studies of alkanethiol SAMs could be complicated by tip artifacts. More research must be done to know the extent of this effect. At one extreme, different tip artifacts on images of the one true alkanethiol SAM structure are the only source of the apparent phases reported in the literature. At the other extreme, this effect is a relatively insignificant source of noise that slightly complicates the measurement of the alkanethiol phases.

### 5.4. References

1. D. P. Fogarty, A. L. Deering, S. Guo, Z. Wei, N. A. Kautz and S. A. Kandel, Rev. Sci. Instrum. **77** (12), 126104-126103 (2006).
2. S. Rousset, V. Repain, G. Baudot, Y. Garreau and J. Lecoeur, J. Phys.: Condens. Matter **15** (47), S3363-S3392 (2003).
3. L. A. Bumm, J. J. Arnold, T. D. Dunbar, D. L. Allara and P. S. Weiss, J. Phys. Chem. B **103** (38), 8122-8127 (1999).
4. A. I. Guttentag, K. K. Barr, T.-B. Song, K. V. Bui, J. N. Fauman, L. F. Torres, D. D. Kes, A. Ciomaga, J. Gilles, N. F. Sullivan, Y. Yang, D. L. Allara, M. Zharnikov and P. S. Weiss, J. Am. Chem. Soc. **138** (48), 15580-15586 (2016).
5. W. Azzam and L. a. Al-Momani, Appl. Surf. Sci. **266** (0), 239-244 (2013).
6. F. Atamny, O. Spillecke and R. Schlögl, Phys. Chem. Chem. Phys. **1** (17), 4113-4118 (1999).
7. M. Baghbanzadeh, F. C. Simeone, C. M. Bowers, K.-C. Liao, M. Thuo, M. Baghbanzadeh, M. S. Miller, T. B. Carmichael and G. M. Whitesides, J. Am. Chem. Soc. **136** (48), 16919-16925 (2014).
8. Y. Qi, I. Ratera, J. Y. Park, P. D. Ashby, S. Y. Quek, J. B. Neaton and M. Salmeron, Langmuir (2008).
9. S. B. Sachs, S. P. Dudek, R. P. Hsung, L. R. Sita, J. F. Smalley, M. D. Newton, S. W. Feldberg and C. E. D. Chidsey, J. Am. Chem. Soc. **119** (43), 10563-10564 (1997).

# Chapter 6
# Structure and Noise Measurements

DHCT-corrected STM images are a promising foundation for research. Image distortions were previously one of the most common limits to the resolving power of the STM.[1, 2] We expected that after image corrections we would be limited by noise. If this was the case, we would be able to take advantage of digital signal processing techniques like time and spatial averaging to increase our signal-to-noise ratio.[2] Later in this section we measure the noise of STM images with spatial and time averaging to test the limits of measurement with STM. We are finding that tip artifacts are one of the largest barriers to STM image analysis after applying DHCT and spatial averaging. In another STM experiment, we are successfully measuring SAM tilt direction and twist configurations using a bi-component SAM.

Noise and imaging artifacts cannot be eliminated from STM images, but they can be reduced. Isolating the microscope from external noise to the greatest extent practical is important for any nanotechnology lab.[3, 4] The ability to precisely measure the fundamental noise in well-corrected, well-isolated STM images can reveal information about the substrate that we are attempting to uncover.

### 6.1. Noise in STM images

Noise in a signal is random variation of the signal about the expected or correct result. Most noise in digital images is well-described by Gaussian noise.[5] One major source of noise in STM images comes from the lab environment the STM operates in. We attempt to minimize this noise by isolating the STM from the lab environment. We explained in chapter 3 the effects of temperature changes on the STM, but ground vibrations, acoustic noise, and electromagnetic fields

can all couple into STM images as well. If the STM is in a room with an atmosphere and connected to the ground, then vibrations in the air or ground will be transferred to the STM during a scan. Differences in vibration coupling between the STM probe tip and sample cause them to vibrate at different rates. This changes the tip-sample distance over time, engaging the negative feedback loop to compensate for the vibration. The vibrations are encoded in the STM image as noise. Because the STM measures very low currents (as low as 1 pA in this work), induced current from electromagnetic interference can also introduce noise. This noise-induced current changes the STM response away from the intended measurement in a similar way. The electromagnetic noise changes the measured tunneling current, which causes the calculated tip-sample distance to be incorrect. The negative feedback loop compensates for the wrong tip-sample distance, encoding the difference as noise in the STM image.

Some sources of noise are inherent from the instrument design. One such noise source is the feedback loop system. The STM preamplifier is designed to maintain constant current using the negative feedback loop, but it can only respond to changes in current within its response bandwidth.[6] Our preamplifier has a bandwidth around 2 kHz; this noise can be minimized by keeping the STM's sampling rate at or below that frequency. The piezoelectric actuators that are used to position the tip operate at over 100 V, which we control with high-voltage amplifiers.[7] Voltage noise in this signal can cause unintended motion of the probe tip during a scan.

The STM's raster scan pattern is not exactly noisy, but the several orders of magnitude difference in acquisition times between perpendicular scan directions could cause both directions to couple to uncompensated time-dependent drift differently. At typical scan rates, the time between acquisition of two adjacent pixels along the fast-scan direction is on the order of 1 ms, while two adjacent pixels along the slow scan direction are separated on the order of 1 second.

"Noise" in the form of an uncompensated time-dependent thermal drift or piezoelectric actuator nonlinearity would change very little over 1 ms between adjacent fast scan pixels but would change up to 1000 times more over the 1 second delay between slow pixels. This is not really noise, because it is strongly correlated. In addition to appearing much stronger along the slow-scan direction, the position deviation would be strongly correlated with time. The earliest acquired features would skew strongly in one direction, while the latest acquired features would skew in exactly the opposite direction. Due to this effect, we should expect observations of significant additional noise along the STM slow scan direction to be an indicator of poor distortion correction rather than a noise measurement.

Sample noise is noise intrinsic to the sample. Objects that we think of as static for millimeter or micrometer length scales can have measurable motion at smaller length scales. Sample noise is quite sample dependent, so it is likely different for our two different types of samples. The largest source of sample noise for graphite at room temperature is its vibration due to thermal energy. The rigid bonds in graphite cause it to have a high resonance frequency and a low motion amplitude.[8, 9] Motion of alkanethiol SAMs is more complex. C-H bond vibrations of docosanethiol (C22) SAMs have been found to have wavenumbers between 2800 and 3000 $cm^{-1}$ with sum-frequency generation spectroscopy (SFG).[10] This motion is related to the bonds within the alkanethiol molecules. A potentially larger source of sample noise comes from interactions between molecules in the SAM. The structure and dynamics of SAMs can depend on their chain length[11, 12] and the surface of the alkanethiol SAM has occasionally been reported to transition between multiple different structures.[13] The magnitude of these effects has not yet been well studied.

We believe that we can obtain a good estimate of sample noise on alkanethiol SAMs with precise measurement of their position and accurate accounting of other sources of noise. We will be using the location confidence intervals from Chapter 4 as a measurement for overall noise. Our sample size for generating location confidence intervals is in the thousands or tens of thousands for all included images, which we are confident is enough to reach the noise floor for this measurement.

### 6.2. STM Imaging Artifacts

Imaging artifacts are features of the image which do not correspond to the object being imaged. The most commonly encountered imaging artifacts in STM are tip artifacts. Tip artifacts (double- or multiple-tip effects, or tip shape effects) in images are identified by unexpected patterns in the image, close in proximity to each other and caused by changes is tip height.[14] When present, tip artifacts are commonly seen at atomic step edges. One issue introduced with tip artifacts is selection bias. Tips with obvious tip artifacts can be noticed and rejected quickly, but it can be hard to tell the difference between subtle tip artifacts and no tip artifacts. The usual benchmark for sufficiently artifact-free imaging is the observation of atomic/molecular resolution in the image. Flat substrates commonly imaged with STM are also the most likely to hide tip artifacts due to their relatively low total height difference between high and low points. STM tips can be characterized using an image feature that causes a large change in height, like an atomic step or a sharp surface defect. When imaging clean metal surfaces in ultra-high vacuum, tips can be more easily characterized and modified by using the metal to reshape and characterize the tip.[15] Both characterization and modification are much more difficult on substrates covered in an adsorbate overlayer, like our images of alkanethiol SAMs. Other discussions of tip artifacts occur

only in the context of how to fix them, by using image filtering techniques like crystallographic image processing.[14, 16]

Our hope was that high-quality molecular resolution images would also minimize the effects of imaging artifacts, but our results so far indicate that this is not the case. We hope that the results shown in the later sections here will help us acquire and select images with fewer and less impactful artifacts.

### 6.3. Graphite Noise Measurement

We chose HOPG as the substrate to attempt to measure the STM's noise floor. Graphite is a stable and well-studied material, which makes it excellent to use as a test material. Any deviation of our measurements from the literature-reported values are likely to be issues with our microscope or experiment rather than new discoveries. We cannot observe the second carbon atom in the surface unit cell with STM,[17] and we rely on the literature to calibrate the size of the surface unit cell. We chose to measure the noise in the position of the imaged carbon atom and compare it to the expected sample noise. At room temperature, carbon atoms in the graphite lattice vibrate with a frequency near $10^{14}$ Hz, with a root-mean-square amplitude of 6.3 pm in plane and 10 pm out of plane.[8, 9] This vibration is much too fast to be measured by the 2 kHz bandwidth of our STM's current preamplifier, which will act to time average the carbon atom vibrations to the mean value. Since there will be effectively no sample noise, we predict that any observed variation of the carbon atoms from their lattice site is due to noise from the environment, noise introduced by our image analysis, or imaging artifacts.

Our best graphite image and its corresponding average unit cell and confidence intervals can be seen in Figure 6.1. This image was acquired with our lab's previous vibration isolation

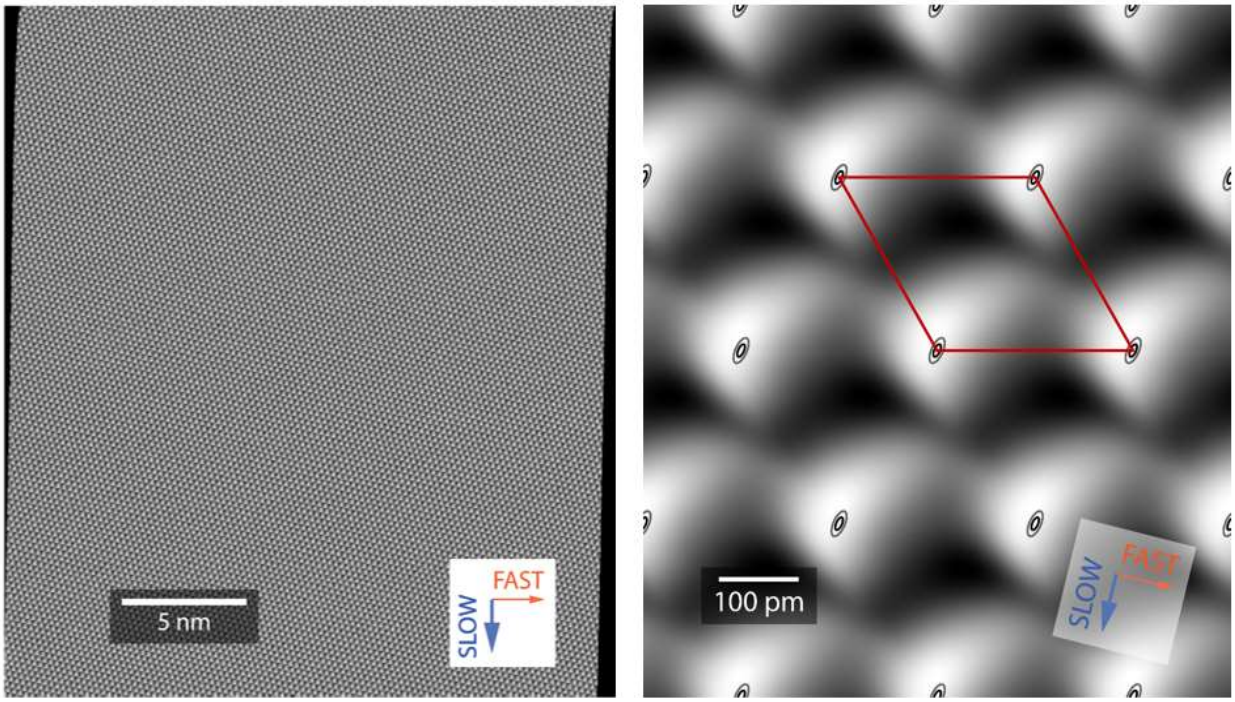


**FIG. 6.1.** (left) DHCT-corrected STM image 2015_11_30_0007, with fast and slow scan directions indicated. Bias voltage –60 mV, tunneling current 160 pA. Trace image. (right) Average unit cell and molecule location confidence interval for the left image.

platform. The ellipses in Figure 6.1 are longest a few degrees away from the slow scan direction, with a maximum uncertainty of ±8.4 pm in that direction and a minimum of ±3.5 pm in the perpendicular direction. This level of noise floor is adequate for performing alkanethiol SAM analysis, though we have still been looking for opportunities to improve it. The maximum amount of residual linear image distortion consistent with ±8.4 pm of noise in a 25 pm image is a scale error of 0.1%, which is strong evidence of successful distortion removal. The graphite surface's 3-fold rotational symmetry has not been preserved. The asymmetry is attributed to asymmetry of the STM tip, which is convolved with the carbon atoms from the graphite surface.

Based on the results so far, we conclude that the residual distortion after DHCT with lattice fitting is quite low, and that by taking advantage of spatial averaging we can estimate our STM system's noise floor to be in the 5-10 pm range. Our successful minimizations of distortion and noise have left the (relatively minor) STM tip artifacts as the largest source of error. In the future

we hope to perform a similar experiment with the new vibration isolation system to determine how effective it is at reducing noise compared to our previous system.

### 6.4. Alkanethiol SAM Structure and Noise Measurements

SAMs are an exciting platform for research due to their ability to modify surface properties of a material without changing its bulk properties. SAMs have potential applications of surface passivation without being modified.[18, 19] Alkanethiols with modified terminal groups allow a wide variety of functionalized surfaces, so long as the substituted alkanethiols still form monolayers and do not phase segregate. With the ability to controllably pattern SAMs, we could functionalize surfaces into templates for producing nanoscale devices.[20] Our understanding of the SAM structure is not deep enough to reproducibly design functionalized surfaces with the self-assembly process. High precision measurements of the alkanethiol SAM surface could help to put additional

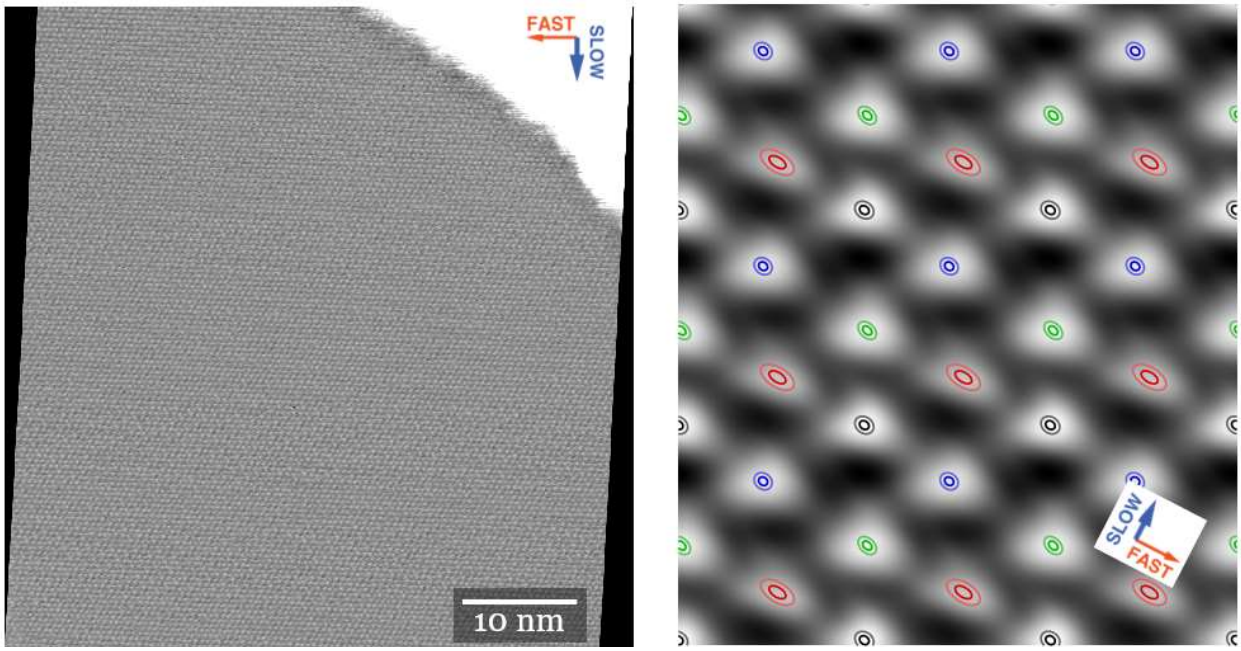


**FIG. 6.2.** (left) DHCT-corrected STM image 2015_04_23_0009, with fast and slow scan directions indicated. Contrast chosen for visibility of the large lower terrace. Bias voltage –1.00 V, tunneling current 1.0 pA. Retrace image. (right) Average unit cell and molecule location confidence interval for the large terrace in the left image.

constraints on models of its structure. More accurate knowledge of the structure allows us to develop models that accurately predict the SAM's behavior when we make changes to it.

Many structures of long-chain alkanethiol SAMs with slightly differing appearances that share the $\left(2\sqrt{3} \times 3\right)$rect. lattice structure have been identified with STM.[21-23] It is currently unknown whether the phases in the literature are fundamentally different from each other. Different appearances could be explained by variability in the STM tip, or a structure with multiple states that it is able to transition between. It is also possible that many similar-energy structures on the surface coexist and appear quite similar in STM images. We have chosen to investigate high-coverage phases of alkanethiol SAMs with STM to attempt to resolve this ambiguity.

### 6.4.1 Single Images

We start by analyzing an image with a single large domain of decanethiol SAM, shown in Figure 6.2. It is obvious from the location confidence intervals in Figure 6.2 that the 4-molecule-basis lattice describes the structure well—each different color of ellipse has its own distinct shape. The locations, heights, and uncertainties for each basis site deviate only slightly from a one-molecule-basis lattice, but the averaging process suppresses the noise well enough for it to be distinctive. Notably, the direction of maximum uncertainty does not appear to be correlated with the scan direction. This shows that our distortion correction works well for alkanethiol SAMs. If most of the noise in the graphite measurement is from our experimental setup, then we expect much of the additional noise in this measurement is caused by the conformational flexibility of the end of the SAMs. If we subtract ±5 pm (estimated noise floor) from ±25 pm (Approximate 1σ ellipse size for the molecules with black, blue and green ellipses), we estimate a contribution to the noise due to room-temperature motion of the SAM surface of ±20 pm. We commonly see

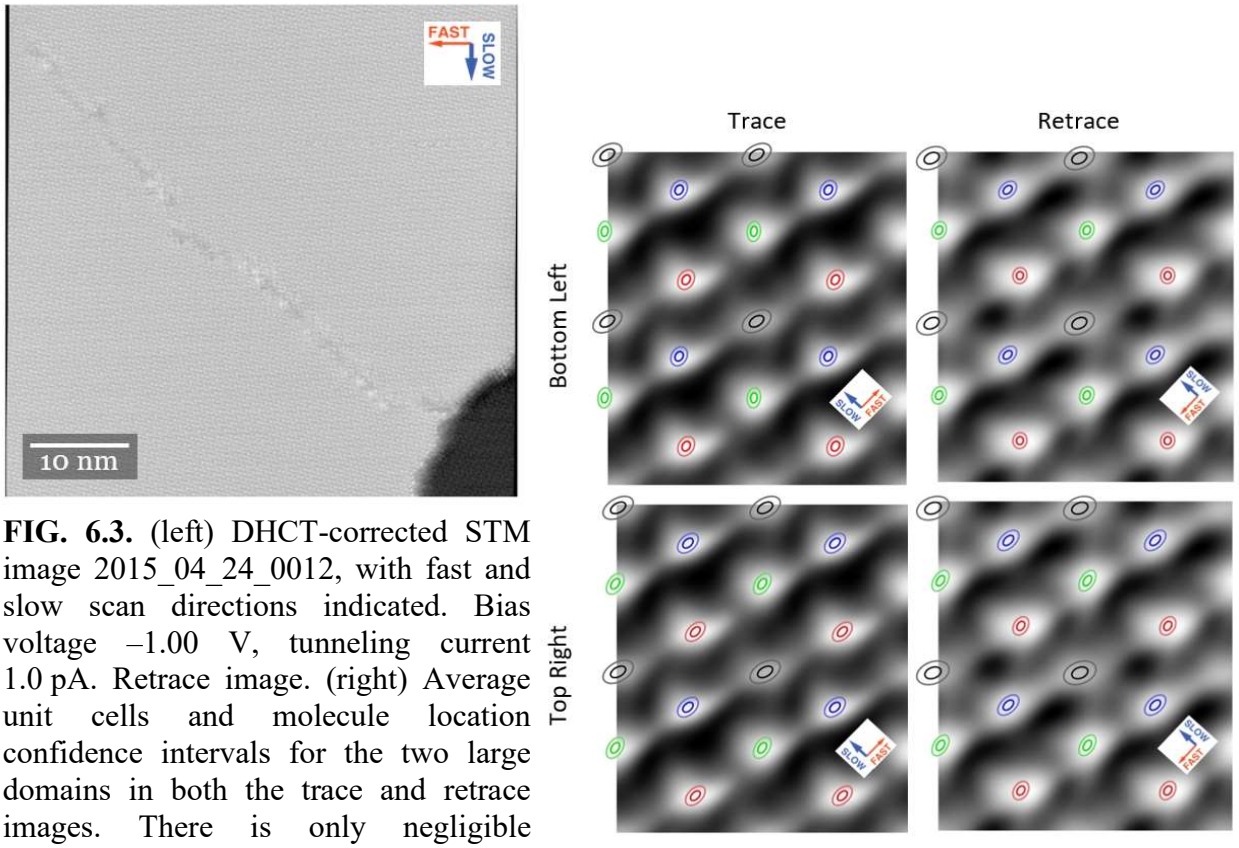


**FIG. 6.3.** (left) DHCT-corrected STM image 2015_04_24_0012, with fast and slow scan directions indicated. Bias voltage –1.00 V, tunneling current 1.0 pA. Retrace image. (right) Average unit cells and molecule location confidence intervals for the two large domains in both the trace and retrace images. There is only negligible difference between the domains, while the differences between the trace and retrace are noticeable but small.

larger location confidence ellipses in the molecule with the lowest height. In Figure 6.2, this would be the molecule with the red ellipse. We attribute the larger ellipse in this case to additional noise. It could be that the lowest feature is less well-resolved, and thus more difficult to locate using our feature location procedure. Another possibility is that the probe is more sensitive to noise when imaging a low feature surrounded by high features. In this image the low feature is only 12.5 pm lower than the highest feature, but imaging artifacts can be revealed even with relatively small changes in height. The repeated triangular shape of the image features appears to be an effect of the tip shape.

Some comparisons within a single decanethiol SAM image can be seen in Figure 6.3. Comparisons within an image are straightforward because they are guaranteed to be made with the

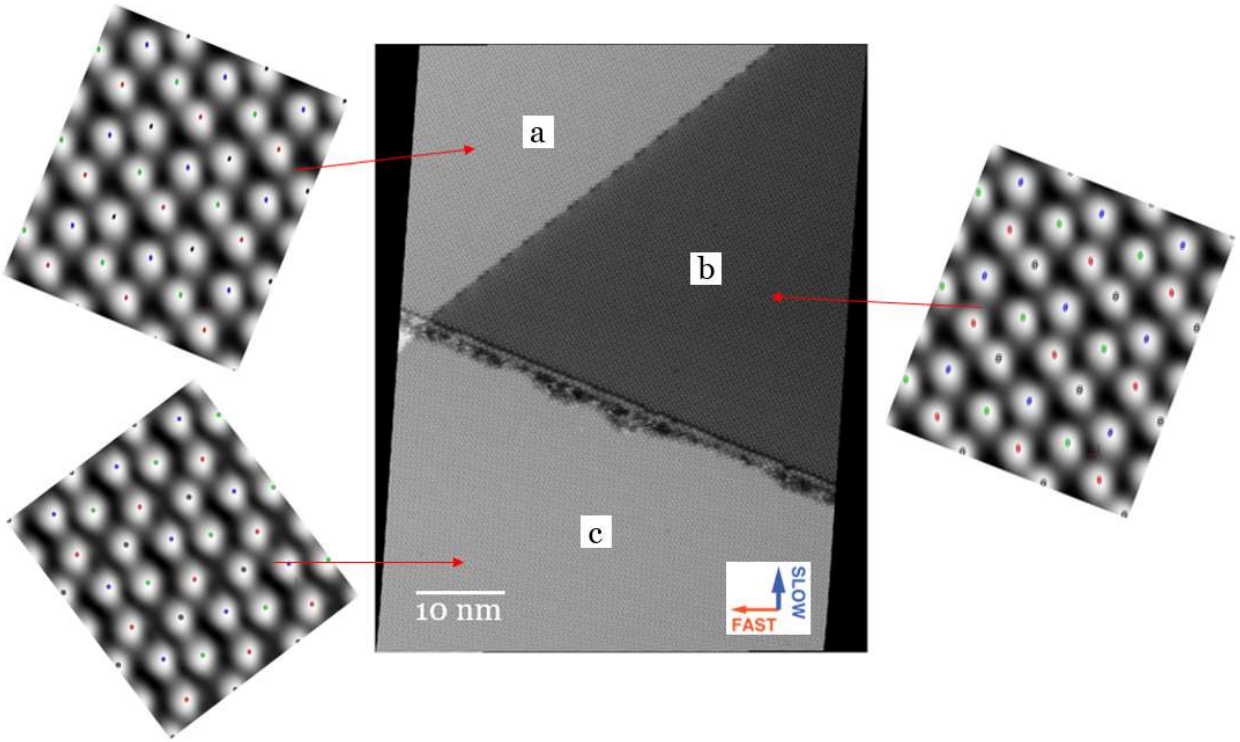


**FIG. 6.4.** (center) DHCT-corrected STM image LT C11 31-1 7-14-2018, with fast and slow scan directions indicated. Bias voltage –2.00 V, tunneling current 5.0 pA. Retrace image. (sides) Average unit cells and molecule location confidence intervals for the domains in the image.

same tip. Between the trace and retrace images, the location confidence ellipses are substantially similar, but the averaged unit cells look slightly different. The slight imaging differences do not seem to change the molecule locations, so combined analysis using both trace and retrace data on a single image is an obvious way to increase the amount of available data for averaging. This image also has a domain boundary separating the image into two large domains. The two domains have the same lattice vectors, so matching them requires only a translation. The ellipse sizes and shapes, as well as the averaged unit cell images, are effectively identical between the two regions. This is strong evidence that the structure is the same on both sides of the boundary.

Some further intra-image comparisons can be seen in Figure 6.4. Figure 6.4 contains an undecanethiol SAM, and it was acquired at 77 K on the Sykes group's LT-STM. It has 3 high quality domains of SAM crystal in two different orientations. The two domains that share lattice

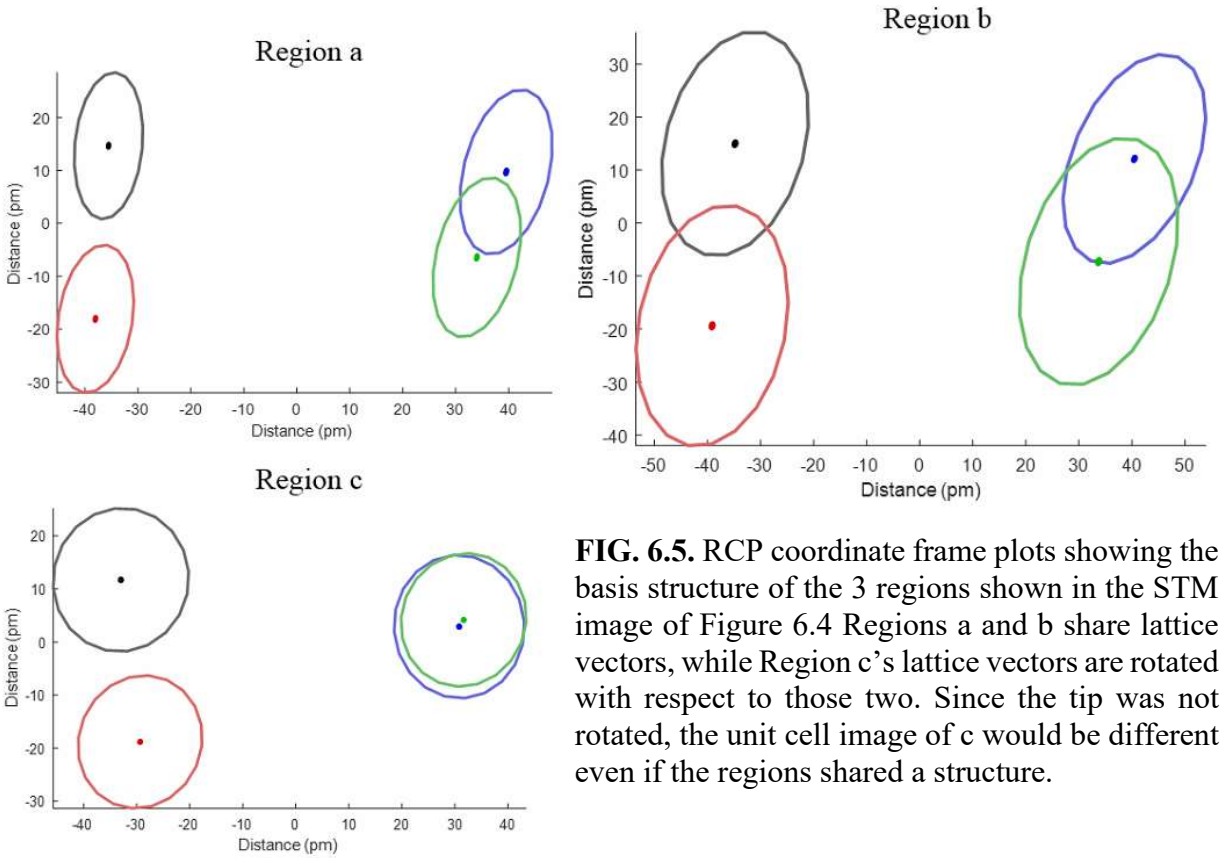


**FIG. 6.5.** RCP coordinate frame plots showing the basis structure of the 3 regions shown in the STM image of Figure 6.4 Regions a and b share lattice vectors, while Region c's lattice vectors are rotated with respect to those two. Since the tip was not rotated, the unit cell image of c would be different even if the regions shared a structure.

vectors (regions a and b in the figure) have very similar averaged unit cells, while region b has slightly larger confidence ellipses due to some deformation in the lattice near the boundaries with the other two regions. Region c's unit cell is distinct, but the appearance of individual features appears similar when all the unit cells are rotated so the tip is in the same orientation. RCP coordinate frame plots for the image in Figure 6.4 can be found in Figure 6.5. While the RCP coordinate frame plot for region c is distinct from the other two, each of the features falls within the location confidence ellipses from regions a and b. We suspect that the structures are the same despite these small differences, and that the difference between the structures is caused by tip artifacts.

### 6.4.2. Multiple Similar Images

Figure 6.6 shows the results from an analysis of a series of 8 images taken on the same region, on the same day with the same tip. We observed an unintentional tip change during the image acquisition, after the first five images were acquired but before the last three. The RCP

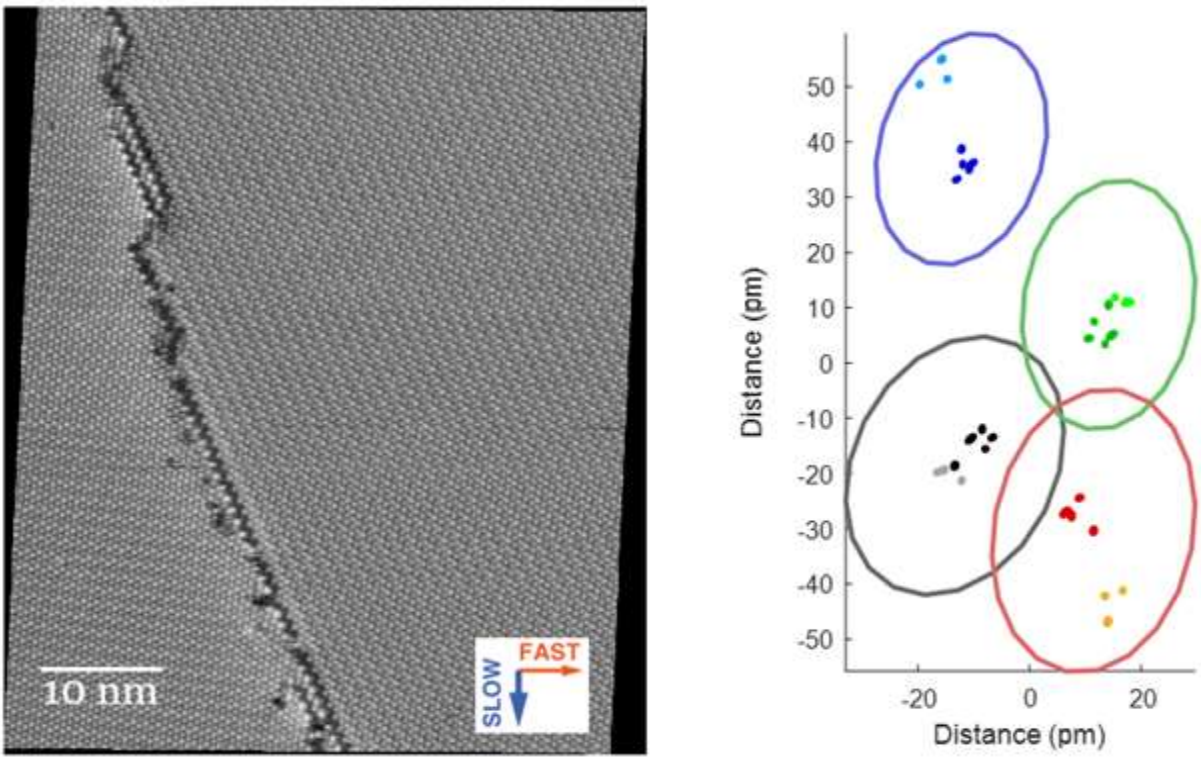


**FIG. 6.6.** (left) DHCT-corrected STM image 2019_06_17_0024, with fast and slow scan directions indicated. Bias voltage –1.00 V, tunneling current 1.0 pA. Trace image. (right) RCP coordinate frame plot showing σ (0019 only) and $\sigma_m$ for each basis site of the large domain in 8 images from one day: 2019_06_17_0013, 0014, 0015, 0017, 0019, 0023, 0024, 0025. The first five images have darker ellipses, while the last three images have brighter ones. 2019_06_17_0022 contains an unintended tip modification.

coordinate frame plot for the surface unit cell structure in these images are all within 1σ of each other, but not within 1$\sigma_m$. This indicates some additional systematic uncertainty in comparisons between images not accounted for by the probability confidence ellipses. Our measurement of the mean location

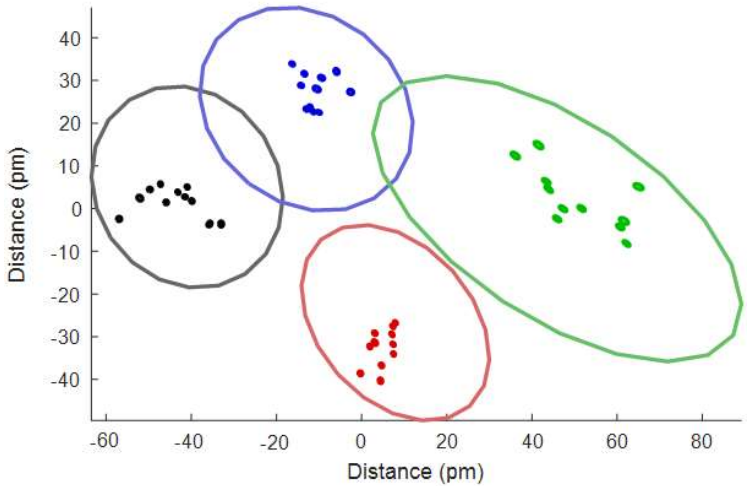


**FIG. 6.7.** RCP coordinate frame plot showing σ (0009 only) and $\sigma_m$ for each basis site of the large domain in 13 images from one day: 2015_04_23_0003 through 0013. The corrected STM image for 2015_04_23_0009 can be seen in Figure 6.2.

of the molecules in the unit cell has statistical uncertainty ±0.5 pm from the plotted $\sigma_m$. Using the first five images to estimate our systematic uncertainty for stable tips, we get ±5 pm. Figure 6.7 shows a similar analysis from an older image series taken on our older vibration isolation system. The systematic uncertainty in these images is closer to ±10 pm. It is promising for our technique that we seem to be limited by instrument noise rather than analysis precision. It also appears that our new vibration isolation system is an improvement over our previous one. We would have liked to do a similar analysis for images acquired on the Sykes group's LT-STM, but we did not acquire any sequences of several high-quality images in a row in the limited amount of time we had on their microscope.

The result from Figure 6.6 also shows how sensitive this measurement is to the STM tip. The 3 lighter $\sigma_m$ ellipses of each color were acquired after an unintended tip modification— the images both before and after the unintended tip modification were still of excellent quality. Despite the high quality of the two sets of images, the mean location of the lattice sites within the unit cell varies by as much as 20 pm between the image sets. Since the image sets were taken sequentially while being constantly monitored by the STM, we suspect that this difference is due to the unintended tip modification we observed. It seems that even small perturbations of the tip, like an unintended tip modification that leaves the STM with excellent quality images, could significantly affect our measurement of the ($x$, $y$) coordinates of the molecule ends.

This limitation prevented us from supplementing our data by comparing between different days. Figure 6.8 shows RCP coordinate frame plots taken from images of 7 different regions, with 7 different tips on 6 different days. All of these images were taken on our microscope at 300 K with a decanethiol SAM at –1.00 V and 1.0 pA, so they should be directly comparable. These

measurements were not as strongly correlated as we expected. Due to the very low correlation of structures shown here, we have failed to prove that any the structures shown here are the same. This does not allow us to draw strong conclusions about the data. One possible conclusion is that there is more than one alkanethiol SAM structure. Another possibility is that the variation of results caused by different tip shapes introduced too much error in our measurements. Yet another possibility is that both are true. If we imaged 7 different structures in our 7 best alkanethiol images, then the probability that there are more than 7 different structures is quite high. We need to rethink our experimental design if we want to continue with this direction.

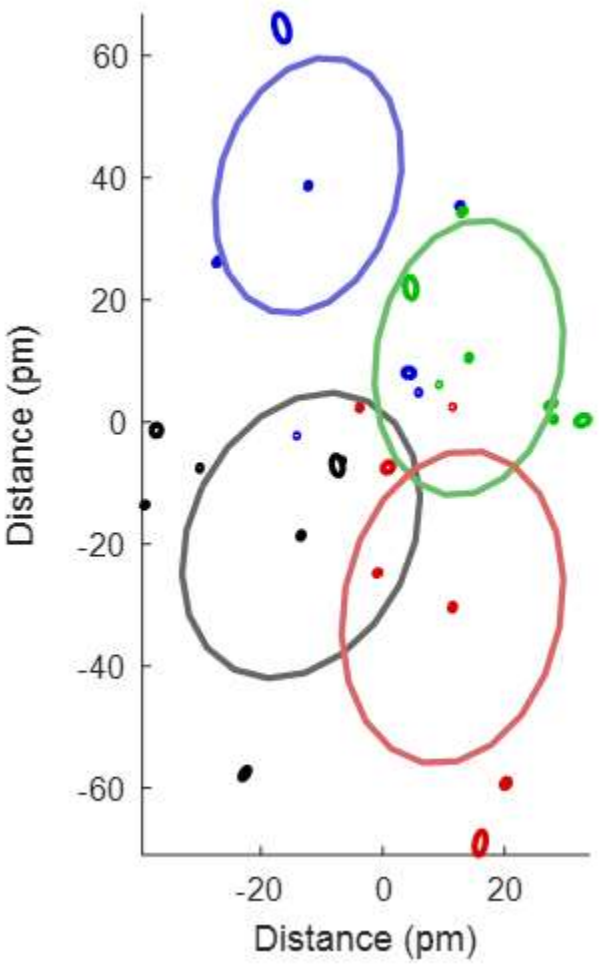


**FIG. 6.8.** RCP coordinate frame plot showing σ (2019_06_17_0019 only) and $\sigma_m$ for each basis site of the largest single domain in 7 images with 7 different tips from 6 different days: 2019_06_17_0019, 2019_06_17_0033, 2019_06_12_0015, 2018_04_02_0012, 2015_04_15_0035, 2015_04_23_0009, and 2015_03_03_0074.

### 6.4.3. Comparing Different Images

We acquired alkanethiol SAM images at different temperatures (300 K, 77 K and 4 K) to study temperature dependent effects, as well as images with different chain lengths (C10 and C11) to test the odd-even effect often discussed in the literature. So far, we have found that differences between STM tips detract from our ability to compare images acquired with different tips. We are

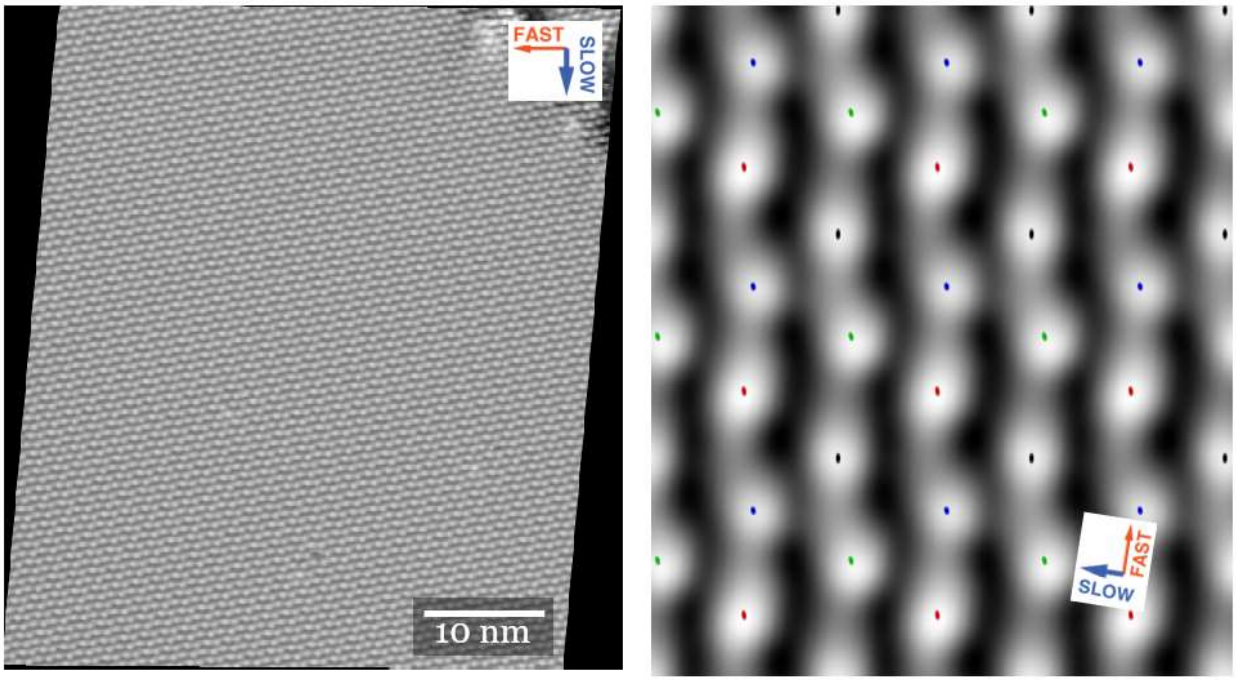


**FIG. 6.9.** (left) DHCT-corrected STM image LT C10 20-1 7-12-2018, with fast and slow scan directions indicated. Bias voltage –1.70 V, tunneling current 10 pA. Retrace image. Acquired at 77 K. (right) Average unit cell and molecule location confidence interval for the large terrace in the left image.

not yet able to make a robust comparison of temperature effects or odd-even effects on the structure. We are still able to compare between the results of our single-image analyses to see what we can find. Figure 6.9 shows a LT-STM image of decanethiol acquired at 77 K, and Figure 6.10 shows a LT-STM image of decanethiol acquired at 4 K. We will compare these results with the decanethiol SAM at room temperature from Figure 6.2. The room temperature ellipses from Figure 6.2 show an uncertainty of ±25 pm. The ellipses from the 77 K image seen in Figure 6.8 are much smaller, at only ±10 pm. The ellipses from the 4 K image are slightly larger, at ±15 pm. We suspect most of the difference between the room temperature and 77 K images is due to freezing out the thermal motion of the SAMs, but the microscope, tip, and vacuum system are different between these two experiments as well. While the 77 K and 4 K images should be more directly comparable due to being acquired on the same instrument, the 4 K image is complicated by $H_2$ adsorbed to the SAM from the UHV chamber background gas.

Alkanethiol SAMs have occasionally had odd-even effects reported in the literature.[24-27] These measurements are usually limited to wettability and charge transport measurements, and if odd-even effects are found they are quite small. We hoped that we could find a structural difference between surfaces of SAMs with odd and even chain lengths to lend support to the odd-even effect measurements. This is complicated by the limitations we discovered comparing images acquired by different probe tips. We can compare the image analysis results from Figure 6.9 (77 K C10) with Figure 6.4 (77 K C11) to check for obvious odd-even effects. A comparison of their RCP coordinate frame plots can be found in Figure 6.11. Their ellipse sizes and shapes seem to be about the same. The locations of the ellipses are different, but these were acquired on different samples, with a modified tip. We do not know how significant this structure measurement is, since we have only one good image each. We don't have a measurement of the statistical uncertainty of the LT-STM instrument or a measurement of the difference between the tips of these two images.

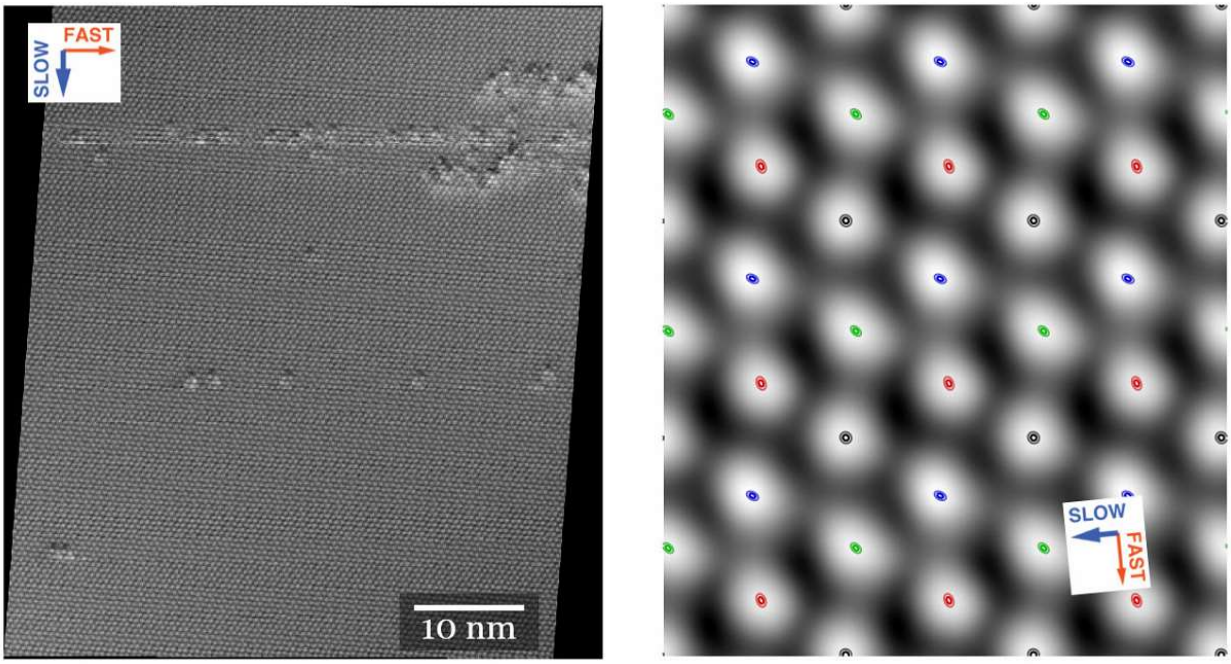


**FIG. 6.10.** (left) DHCT-corrected STM image LT C10 7-1 7-12-2018, with fast and slow scan directions indicated. Bias voltage –1.50 V, tunneling current 3.0 pA. Retrace image. Acquired at 4 K. The image contains some unexpected surface defects. (right) Average unit cell and molecule location confidence interval for the defect-free regions of the left image.

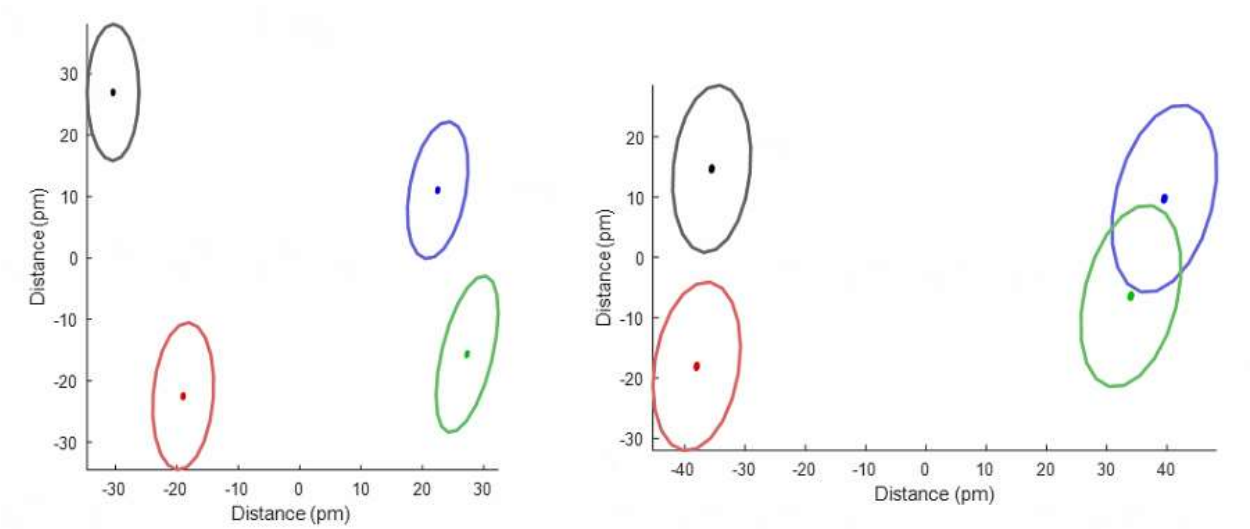


**FIG. 6.11.** (left) RCP coordinate frame plot for LT C10 20-1 7-12-2018. Acquired at 4 K. (right) RCP coordinate frame plot for LT C11 31-1 7-14-2018. Acquired at 77 K.

### 6.5. Measuring Internal SAM Structure

We designed an experiment to measure the internal structure of the SAM by imaging bi-component SAMs. In this experiment we chose to use alkanethiol chains that differed in length by 1 and 2 methylene units. We hoped that similar-length alkanethiol chains would minimize disorder of the emerging tail of the longer chain. C10 was chosen as the host SAM with C11 and C12 guests because we were confident in our ability to resolve the C10 SAM with STM. If the disorder in the part of the chains emerging from the SAMs is small, the terminal groups will continue their all-trans configuration from the part embedded in the monolayer. In order to compare the guest molecules to the host monolayer, we also need the two components to form a single mixed SAM rather than phase separate. Multiple alkanethiol chain lengths are known to create mixed monolayers rather than phase separate, so long as they have similar chain lengths.[28] Laibinis, et al. found that their mixed solutions of C12 and C22 formed a bi-component SAM, where the carbons that do not extend above the surface of the shorter molecule's SAM formed a neat SAM and the remaining terminal group appears disordered. For a guest two methylene units longer than its host,

the total extension of two carbon atoms offsets the molecule end along the molecular backbone, which we know is tilted 30° from the surface normal.[29] This measurement would give us a way to probe the alkanethiol chain tilt using STM. For a guest inserted into a host that was only one carbon atom shorter, the extension would depend on the twist of the molecule due to the zig-zagging structure of the all-trans molecule. This would not allow us to measure the twist directly, but molecules offset in different directions could be identified as having different twists.

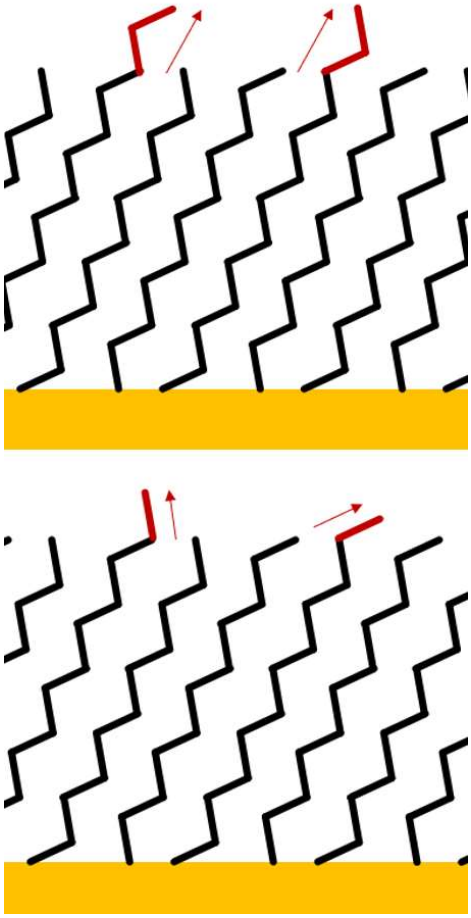

**FIG. 6.12.** Schematic diagram of experimental design for bi-component SAM system. (top) C12 guest molecules in a C10 host SAM extend along the molecular backbone direction independently of twist. (bottom) Extensions of C11 guest molecules in a C10 host SAM depend on the molecular twist angle.

Han, et al. claimed to be able to measure the interface structure by recording a local barrier height measurement along with their STM topography measurement, which they claimed was measuring the topgraphy of the Au-S interface.[30] They used a similar technique to the one we are using, but their distortion correction methods were much less sophisticated. In addition, their choice of shorter guests instead of longer ones both makes it much harder to resolve the guest molecules and distinguish whether tip artifacts are present. This technique could be used to reproduce their results with higher precision.

A bi-component alkanethiol image composed of 5% C12 and 95% C10 can be seen in Figure 6.13. The locations of the guest molecules inserted into the surface are consistently offset

from the host monolayer's lattice sites. The offset distance depends on basis, but the offset varies between 50 and 115 pm and are consistently offset towards the right side of the unit cell, or the top left corner of the image. We believe this is a successful measurement of the SAM's tilt direction. If the longer C12 guest molecules stayed in their all-trans configuration, we would expect them to extend another 250 pm from the host C10 monolayer surface at a tilt of 30°. This would cause the ends of the guest molecules to be 216 pm higher and offset 125 pm in plane. If we allow the molecules to relax, then the measurement will be somewhat less. Based on an average

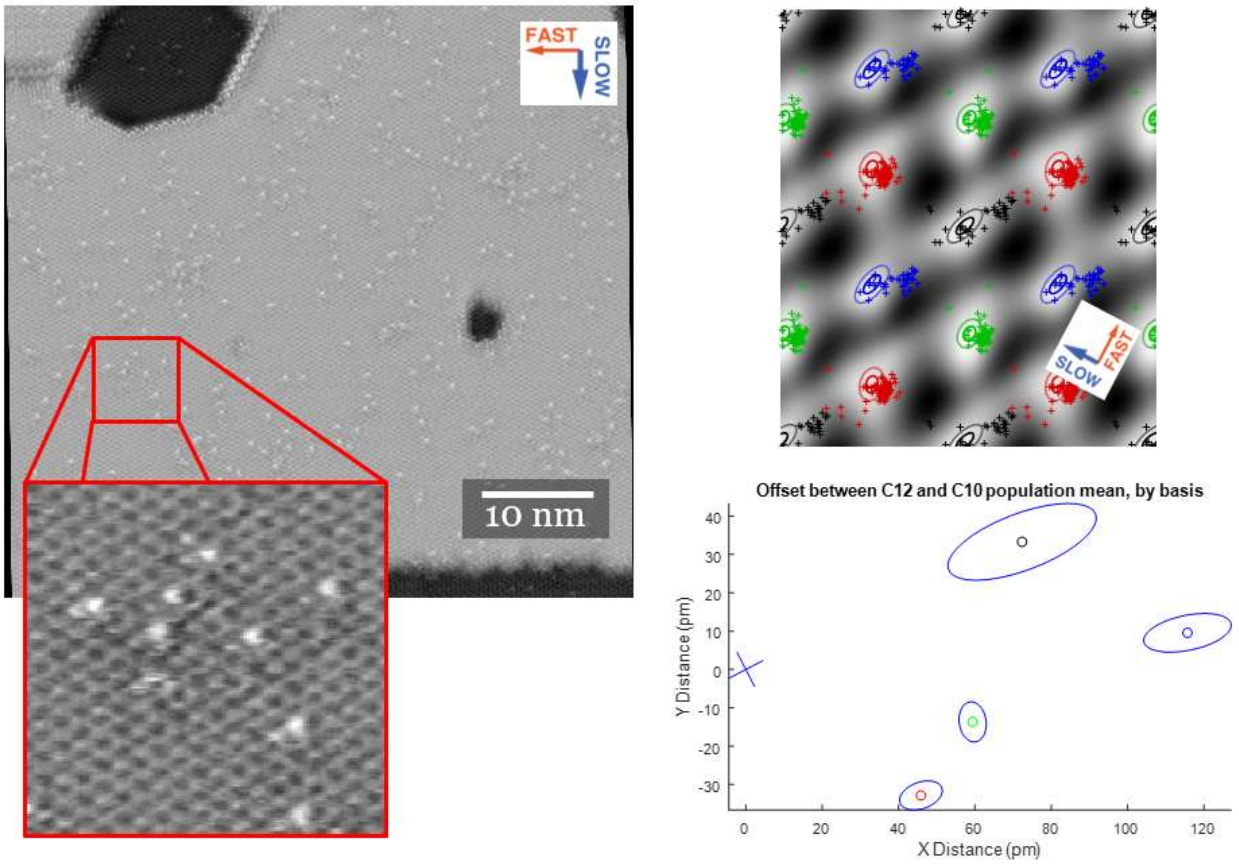


**FIG. 6.13.** (left) DHCT-corrected STM image 2015_06_22_0015, with fast and slow scan directions indicated. Bias voltage –1.00 V, tunneling current 1.0 pA. Retrace image. (top right) Average unit cell and molecule location confidence interval for the C10 (short) molecules in the large terrace in the left image. Each + indicates the location of a C12 (long) molecule. (bottom right) Plot showing the expected value and $1\sigma_m$ uncertainty of the difference between the mean location of the short and long molecules.

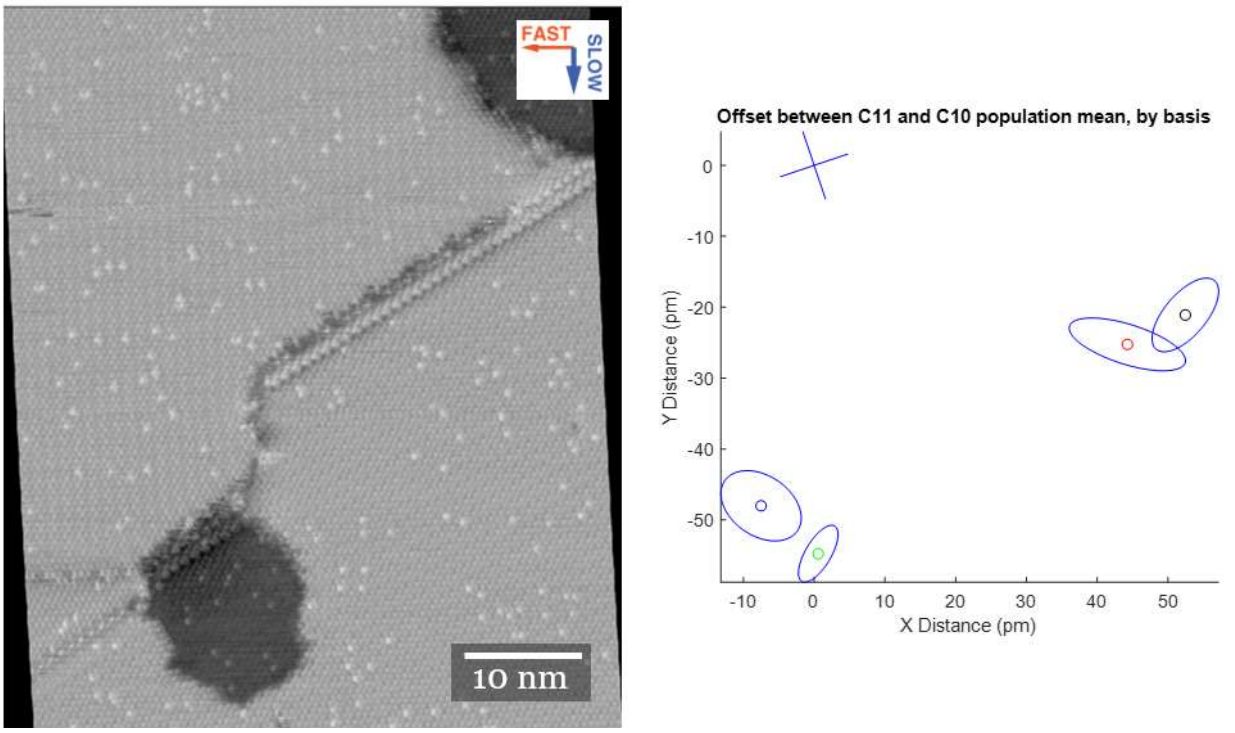


**FIG. 6.14.** (left) DHCT-corrected STM image 2018_06_11_0007, with fast and slow scan directions indicated. Bias voltage –1.00 V, tunneling current 1.0 pA. Retrace image. (right) Plot showing the expected value and $1\sigma_m$ uncertainty of the difference between the mean location of the short (C10) and long (C11) molecules.

height difference between the guest and host features of 110 pm and the in-plane offsets of 50-115 pm, the data seem to fit with our model of the bi-component SAMs.

An analysis of an image with C11 guest molecules in a C10 host can be seen in Figure 6.14. If these molecules are offset from the host remaining in their all-trans configuration in accordance with our model, their offset should depend on the molecular twist, since the difference in length of the chains is odd. The C11 guest offsets appear to group into two pairs, with about the same total offset but in different directions. If our model is correct, this result means that the 4-molecule-basis structure is composed of two pairs of distinctly different twists that form zigzag rows on the surface, where each row has its own twist. Distinctly different twists agrees with the nearly-perpendicular twists measured by infrared spectroscopy.[31] This is the first measurement of the arrangement of the molecular twists within the surface unit cell for this system.

While these results are promising, we have had trouble reproducing these results on other images. Guest molecules have a large variability in their appearance between images taken with different tips. Even among images where guests can be separated from the host, images where the guests are less obvious than the examples shown above show smaller offsets. We again suspect that this is a tip artifact caused by the condition of the tip. At least for these samples, well-resolved guest molecules are a good indication of an image relatively free of tip artifacts.

An example of the lower total offset can be seen in Figure 6.15. This image was acquired as one frame of an image sequence, whose goal was to take advantage of time averaging's improvement of the signal-to-noise ratio. This image sequence is composed of 22 images of C12 guest molecules in a C10 host. Unfortunately, these images did not reproduce our result from earlier, possibly due to a strange tip shape effect that reduces the prominence of the guest molecules. The guest molecules in these images were not as well resolved as they were in the single image with the same composition shown in Figure 6.13. These guest molecules were both

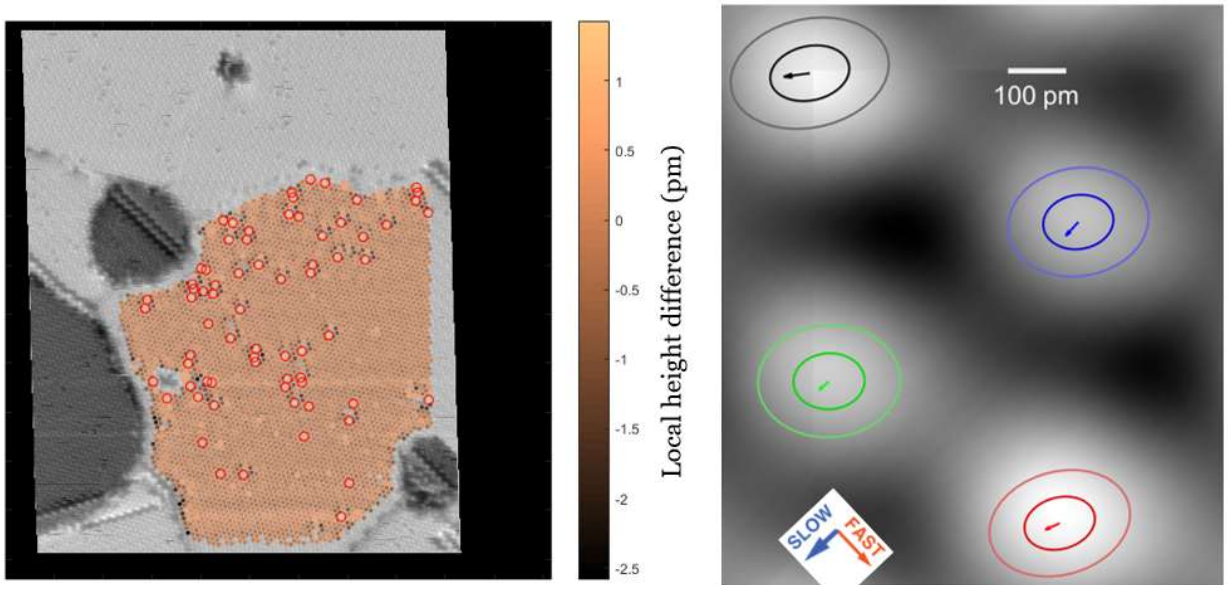


**FIG. 6.15.** (left) DHCT-corrected STM image 2017_08_14_0020. Bias voltage –1.00 V, tunneling current 1.0 pA. Retrace image. Plotted on the image is the difference in height between each feature and its nearest neighbors. (right) Averaged unit cell and molecule location confidence intervals for all the C10s in the large region in all 22 frames of the movie, and the offset from the C10 to C12 positions within the unit cell.

more difficult to identify in the host monolayer and appeared to be less offset from the host lattice (only 20-50 pm offset instead of 50-115 pm).

### 6.6. Conclusions

The main conclusion of our research so far is the much higher than expected sensitivity of image feature positions within the unit cell to the condition of the STM probe tip. At the outset, we expected that probe tips that gave high-quality images would give measurements of unit cell structure that were consistent with each other, but our data do not agree with that expectation. While tip artifacts have been an unexpected setback, the research that didn't involve comparing STM images taken with different probe tips has been quite promising. DHCT allows accurate measurements to be made on STM images, and our measurements so far of SAMs and bi-component SAMs have showed promising results. With appropriately high quality STM images, we suspect that the methodologies outlined here could be used to further measure alkanethiol SAM surface structure, molecular tilt and molecular twist. We hope these promising research directions can be achieved in the future.

### 6.7. References


1. B. S. Salmons, D. R. Katz and M. L. Trawick, Ultramicroscopy **110** (4), 339-349 (2010).
2. L. Jones, S. Wang, X. Hu, S. ur Rahman and M. R. Castell, Adv. Struct. Chem. Imag. **4** (1), 7 (2018).
3. E. Lörtscher, D. Widmer and B. Gotsmann, Nanoscale **5** (21), 10542-10549 (2013).
4. K. Iwaya, R. Shimizu, T. Hashizume and T. Hitosugi, Rev. Sci. Instrum. **82** (8), 083702 (2011).
5. K. R. Castleman, *Digital Image Processing*. (Prentice Hall, Toronto, 1996).
6. M. Carlà, L. Lanzi, E. Pallecchi and G. Aloisi, Rev. Sci. Instrum. **75** (2), 497-501 (2004).
7. J. Peng and X. Chen, Mod. Mech. Eng. **3** (1), 1-20 (2013).
8. B. T. Kelly, J. Nucl. Mater. **24** (2), 210-214 (1967).
9. B. T. Kelly, J. Nucl. Mater. **34** (2), 189-192 (1970).
10. M. Himmelhaus, F. Eisert, M. Buck and M. Grunze, J. Phys. Chem. B **104** (3), 576-584 (2000).
11. P. Carro, E. Pensa, C. Vericat and R. C. Salvarezza, J. Phys. Chem. C **117** (5), 2160-2165 (2013).
12. E. Torres, A. T. Blumenau and P. U. Biedermann, ChemPhysChem **12** (5), 999-1009 (2011).
13. F. Li, L. Tang, W. Zhou and Q. Guo, Phys. Chem. Chem. Phys. **13** (25), 11958-11964 (2011).
14. J. C. Straton, T. T. Bilyeu, B. Moon and P. Moeck, Cryst. Res. Technol. **49** (9), 663-680 (2014).
15. S. Tewari, K. M. Bastiaans, M. P. Allan and J. M. van Ruitenbeek, Beilstein J. Nanotechnol. **8**, 2389-2395 (2017).
16. P. Moeck, in *Microscopy: Science, Technology, Applications and Education*, edited by A. Méndez-Vilas and J. Díaz (FORMATEX, Badajoz, Spain 2010), Vol. 3, pp. 1952-1962.
17. S. Hembacher, F. J. Giessibl, J. Mannhart and C. F. Quate, Proc. Natl. Acad. Sci. **100** (22), 12539-12542 (2003).
18. P. E. Laibinis and G. M. Whitesides, J. Am. Chem. Soc. **114** (23), 9022-9028 (1992).
19. C. D. Bain, E. B. Troughton, Y. T. Tao, J. Evall, G. M. Whitesides and R. G. Nuzzo, J. Am. Chem. Soc. **111** (1), 321-335 (1989).
20. W. Mizutani, Jpn. J. Appl. Phys. **38** (12B), 7260-7263 (1999).
21. B. Lussem, L. Muller-Meskamp, S. Karthauser and R. Waser, Langmuir **21** (12), 5256-5258 (2005).
22. G. E. Poirier and M. J. Tarlov, Langmuir **10** (9), 2853-2856 (1994).
23. E. Delamarche, B. Michel, C. Gerber, D. Anselmetti, H. J. Guentherodt, H. Wolf and H. Ringsdorf, Langmuir **10** (9), 2869-2871 (1994).
24. M. Baghbanzadeh, F. C. Simeone, C. M. Bowers, K.-C. Liao, M. Thuo, M. Baghbanzadeh, M. S. Miller, T. B. Carmichael and G. M. Whitesides, J. Am. Chem. Soc. **136** (48), 16919-16925 (2014).
25. Z. Wang, J. Chen, S. Oyola-Reynoso and M. Thuo, Coatings **5** (4), 1034-1055 (2015).
26. P. Srivastava, W. G. Chapman and P. E. Laibinis, Langmuir **21** (26), 12171-12178 (2005).
27. M. M. Walczak, C. Chung, S. M. Stole, C. A. Widrig and M. D. Porter, J. Am. Chem. Soc. **113** (7), 2370-2378 (1991).

28. P. E. Laibinis, R. G. Nuzzo and G. M. Whitesides, J. Phys. Chem. **96** (12), 5097-5105 (1992).
29. R. G. Nuzzo, L. H. Dubois and D. L. Allara, J. Am. Chem. Soc. **112** (2), 558-569 (1990).
30. P. Han, A. R. Kurland, A. N. Giordano, S. U. Nanayakkara, M. M. Blake, C. M. Pochas and P. S. Weiss, ACS Nano **3** (10), 3115-3121 (2009).
31. R. G. Nuzzo, E. M. Korenic and L. H. Dubois, J. Chem. Phys. **93** (1), 767-773 (1990).

# Appendix A: STM Image Analysis User Manual

This set of Image Analysis tools has been developed specifically to correct STM images. Users wanting to adapt the scripts described here to other types of images with linear and non-linear distortions may be able to do so. Such an application would require careful scrutiny of assumptions for each script described here.

## A.1. How to Use this Manual

This appendix provides a general overview on how to run the Bumm group's STM image correction software. It includes descriptions of which data and scripts you will need, how to run the scripts, and it includes an example that you can use as a tutorial when following this manual for the first time. You will need access to a Matlab installation with the Parallel Processing toolbox in order to follow this appendix. This manual was generated using Matlab 2019a on a PC running Windows 7.

This section describes how to find the scripts, the script hierarchy and a workflow of how the highest-level scripts come together to accomplish specific tasks. Each of the remaining sections explores the details of one of the major sections of code, explaining its inputs, outputs and function. The goal of this document is to make the user familiar enough with the scripts to be able to apply them as needed to analyze an image.

### A.1.1. Finding the Scripts

The scripts described in this document can be found in a folder on the LAB group's U: drive, in U:/Image Analysis Software/. DHCT, the code described in section 2, has been publicly released and can be found on Github.

A .SM4 file to practice with, 2015_04_23_0009.SM4, is provided in the same folder. This is an STM image of a decanethiol SAM, acquired at -1.0 V and 1.0 pA. Other .SM4 files can be found in U:/STM_DATA/.

### A.1.2. Script Hierarchy

An indented script indicates that the previous less-indented script depends on this script.

Histofit.m
    Histofit.fig
    SMread.m
        SM3read.m
        SM4read.m
MaskDraw.m
    MaskDraw.fig
SimplexfiltShell.m
    psfit.m
    xfilt.m
DHCT.m
    data_mask_select.m
        find_nearest_neighbors.m
        position_analysis.m
    feat_position.m
    fitresult_modify.m
        drift_models.m
    find_molecules.m
    fmgaussfit_reduced.m
    ImCoords.m
        drift_models.m
    ImReshape.m
    molecule_local_distortion.m
        drift_models.m
    time_assign.m

DHCT_4nn.m
    get_guess.m
        feat_position.m
        data_mask_select.m
            find_nearest_neighbors.m
            position_analysis.m
    gather_4nn.m
    molecule_local_distortion.m
        drift_models.m
    ImCoords.m
        drift_models.m
    ImReshape.m
    fitresult_modify.m
        drift_models.m
c4x2_add.m
    ImReshape.m
    fitresult_modify.m
        drift_models.m
    image_offset.m
    get_guess.m
        feat_position.m
        data_mask_select.m
            find_nearest_neighbors.m
            position_analysis.m
    cell_assign.m
    lattice_pair_fit.m
        fun_image.m
    cell_unassign.m
lattice_pair_fit_r.m
    fun_image_r.m
poly_trans.m
data_filter.m
unitcell3_single.m
    get_mol_list.m
prob_contour_3.m
basis_remix.m
plot_basis_offset.m
get_frame_data.m
movie_setup_2.m
correlation_plot_2d.m
local_height.m
MoleculeClick.m
    MoleculeClick.fig
offset_ellipse_2.m
model_simulate.m
    cell_parameters.m

### A.1.3. Script Workflow

Main thread: Load .sm4 file with Histofit. Run MaskDraw and SimplexfiltShell on Histofit output. Run DHCT using output of Histofit, MaskDraw and SimplexfiltShell to correct the image. Run DHCT_4nn on output of DHCT to improve the image correction for alkanethiol SAMs, or skip this step for graphite. Run c4x2_add on image correction output to generate a best-fit lattice. Run lattice_pair_fit_r on the data structure with lattice fitting to perform a lattice enforcement that improves image lattice registration. Run data_filter on the lattice-fit or lattice-enforced data structure to filter out basis sites with too many features.

Side thread 1: after running the main thread, run unitcell3_single on the filtered dataset to generate a lattice-averaged unit cell image for an alkanethiol SAM. Run prob_contour_3 after generating a unit cell image to plot molecule location confidence intervals on that cell.

Side thread 2: After running side thread 1, follow section A.6.1. to align images for comparison or generate molecule location confidence plots.

Side thread 3: After running the main thread once for each image in an image series and saving each result, follow section A.6.2. to generate an aligned image set movie.

Side thread 4: After running the main thread, follow section A.6.3. to generate a 2D correlation plot.

Side thread 5: After running the main thread on a bi-component SAM image, follow section A.6.4. to calculate the offset between the guest and host alkanethiols.

Side thread 6: Run model_simulate after defining model parameters in cell_parameters. This does not depend on the main thread.

### A.2. Setup

In order to use this manual, you must first setup your image in Matlab. This manual will describe the setup requirements for any image and lead you through in detail how to setup a .SM4 image of an alkanethiol SAM on Au{111}. Setup requires several steps. The steps are importing the image into Matlab, image plane subtraction, and image cleanup/filtering.

#### A.2.1. Setup Requirements

Setup is complete when you are ready to run DHCT. DHCT requires these inputs:

XScale: The size in meters of one side of one of the pixels in your image as reported by the STM scan controller. DHCT has only been tested on images with the same pixel scale along both X and Y, so YScale is assumed to be equal to XScale. Since DHCT does independent scale correction, this does not need to be particularly accurate, within 10% of the true value should be fine.

Period: The time in seconds it takes to acquire one pixel in your image. This is a soft requirement; the code should produce the same final image no matter what value you put in for the period. Including the correct period will make each plot that depends on time have accurate axis labels.

SlowScanDir, FastScanDir: String(s) describing the slow and fast scan directions of the input image. Valid strings are ‘Right’, ‘Left’, ‘Up’ and ‘Down’. SlowScanDir requires one of these strings, FastScanDir requires a cell array of these strings. Slow and Fast scan direction must be

orthogonal. If you are analyzing a trace and retrace image simultaneously, FastScanDir should have two of these strings in a 1x2 cell array.

Spacing: The distance in meters between nearest neighbor features on your trigonal lattice. This should be sourced as accurately as possible from a different experiment, since DHCT uses this as a reference to correct the image scale. If you are analyzing images of an alkanethiol SAM, the distance is 2.88e-10*sqrt(3).

Image(s): DHCT supports either a single image or a trace-retrace pair. Each of the images imported into DHCT should be Matlab double-precision 2D arrays. Each image should be plane subtracted, and Fourier fast scan line noise filtering is usually required. Other filtering or image scaling can be done as well to improve results. These variables are named Img1 and Img2 when loaded in from Histofit.

Mask(s): These are optional. Including logical mask(s) the same size as your input image(s) will use only the features in the logical true area of the mask(s) for analysis. If using masks, I recommend naming them Mask1, Mask2, etc.

Once you have these inputs in Matlab, you have completed the setup.

### A.2.2. Setup Walkthrough

This walkthrough describes how to reach the setup condition described in the previous section from a .SM4 file with the provided scripts. If your data is not in a .SM4 file, you will have to develop your own setup procedure.

Start by running Histofit in Matlab. Histofit.m requires the Histofit.fig file, and also depends on SMread, SM4read (for SM4 files), and SM3read (for SM3 files). It can be run in the console with this command:

```
Histofit;
```

Histofit should open a GUI for hybrid manual/automatic plane subtraction of .SM4 STM images and Matlab import. The GUI is shown on the next page. Click ‘Browse”, then navigate using the file browser to your desired .SM4 file or Histofit saved data file for that .SM4 file, load it, then click “Analyze’. This runs SM4read on the selected file and loads the file information into the GUI. Your first goal is to flatten the image. You can use the Z vs X and Z vs Y plots to gauge

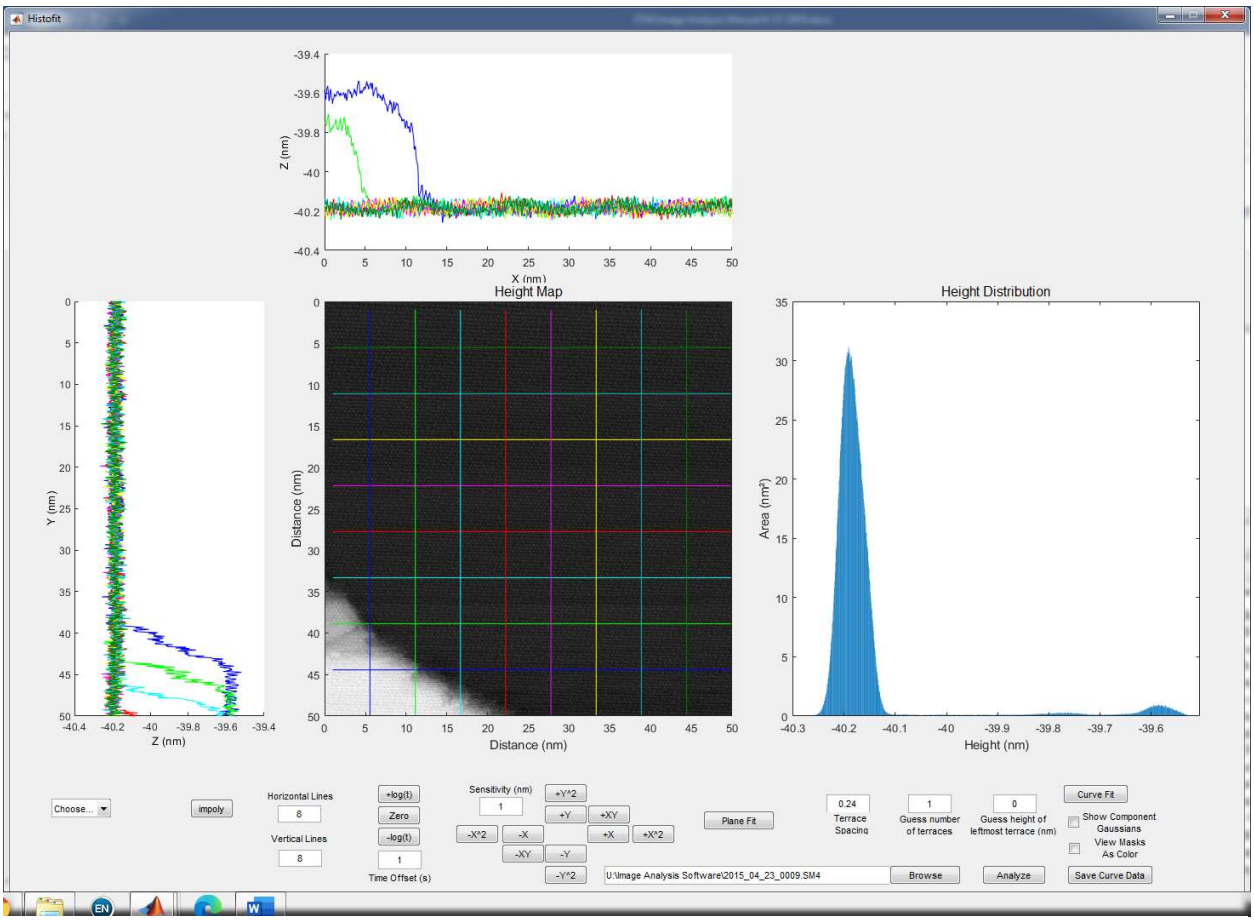


**FIG. A.1.** Screenshot of the Histofit GUI. The STM image is featured in the center, with its height histogram to the right, surrounded by plane subtraction controls.

the flatness of your image and use the manual and automatic plane and parabola tools to flatten the image. You can also include a logarithmic time-dependent subtraction, but this is not recommended. All of the manual flattening controls are multiplied by the sensitivity, which you can increase or reduce to make your manual flattening more sensitive. There is also an automatic plane fitting tool, which applies itself to the whole image automatically when you load an image using Histofit. It is better to only use the plane fitting tool on planar regions of the image, which you can do with the Plane Fit button. Click the button and then use your mouse cursor to draw a shape containing as much of the planar region of your image as possible. See figure A.2. for reference – note that only the flat region of the image was selected for plane fitting. Once you release your left mouse button, it will automatically determine the best fit plane subtraction to that region and apply it to your image. You may tweak the automatic plane subtraction using the manual controls if you like. Once you are happy with your plane subtraction, use the height histogram in the figure on the right of the Histofit window to determine the average height of the lowest gold terrace in the image (Read off the X coordinate of the leftmost peak in the histogram), the spacing between gold terraces (Spacing between histogram peaks), and count the number of gold atomic terraces (One for no gold atomic steps, two for one gold atomic step, and so on). Use these numbers determined from that height histogram to fill out the boxes in the Curve Fit section,

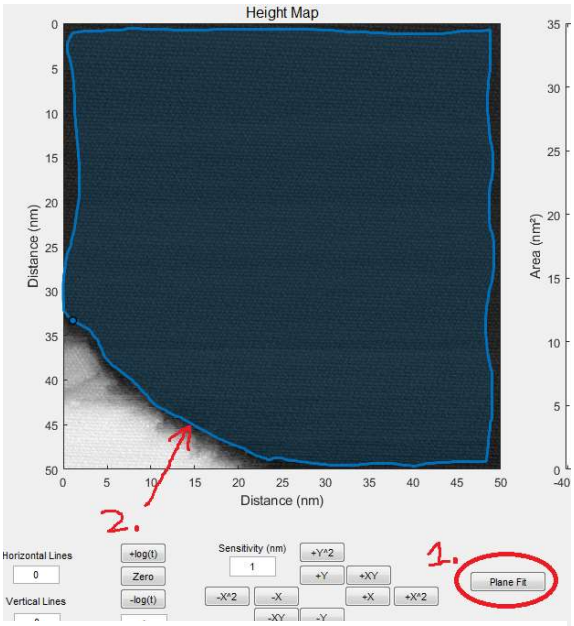


**FIG. A.2.** how to use the plane fit in Histofit. 1. Click the Plane fit button. 2. Click and drag on the STM image to select a flat region of the surface. Histofit will calculate the best-fit plane subtraction to your selection.

which automatically generates terrace masks. Clicking the Curve Fit button will determine the height thresholds for the terrace masks. You can view the masks and the fitting function for the height histogram using the checkboxes. Clicking the save button will save the image data in a file named 'Results.mat' in the active folder and a file named similarly to your file in the Histofit Saved Data folder. You can now close Histofit. Loading the saved file into the Matlab workspace completes this stage of the setup for your image.

The file Results.mat loaded in by Histofit contains the following variables:

Filename: The name of the file you loaded to generate these results, including its file path.

Img1, Img2: Double-precision arrays containing the STM topographic images after plane subtraction. Img1 is trace, Img2 is retrace.

OtherData: Cell array of other STM data channels. Refer to the STM notebook(s) in the lab to determine what these channels were being used for when your image was acquired if you need them.

XScale: The distance in meters of the horizontal side of one pixel.

YScale: The distance in meters of the vertical side of one pixel. This is usually the same as XScale.

ZScale: The height difference in meters between two heights that differ by a single DAC unit.

Period: The time between adjacent pixels in seconds.

Bins, n: The data from the height histogram that was displayed as you saved in Histofit. "bins" contains the location of the bins, while "n" contains the counts within each bin.

SlowScan, FastScan: Integers from 0-3 describing the scan direction. 0 is Right, 1 is Left, 2 is Up, 3 is Down. SlowScan is a single integer, FastScan is a 1x2 vector of integers. The first is the information for the trace, the second is for the retrace.

SlowScanDirection, FastScanDirection: Exactly the same as SlowScan and FastScan, but using words instead of numbers for ease of comprehension.

LowestTerraceHeight, TerraceSpacing, Amplitude, Sigma: Parameters for the best-fit curve to the histogram in Histofit.

Xtilt, Ytilt, Xdeform, Ydeform, XYdeform: The coefficients of the planes and/or parabolas that were used to plane subtract the image. Xtilt is the amount of horizontal tilt, Ytilt is the amount of vertical tilt, Xdeform is the horizontal parabola, Ydeform is the vertical parabola, and XYdeform is the cross term that removes saddling.

HystAmt, TimeOffset: These contain the parameters of your logarithmic time-dependent subtraction if you used one.

TerraceMask: A structure containing height-threshold masks for each terrace, based on the number of terraces in the image. It has several fields. TerraceMask.NumMasks tells you how many masks it contains. TerraceMask.Mask1 contains the lowest mask, TerraceMask.Mask2 has the next lowest mask, and so on.

EdgeMask: A data structure containing NumMasks – 1 masks (minimum 1), with each mask being the height threshold region between two subsequent masks. If NumMasks is 1, EdgeMask.Mask1 is instead entirely zero.

Many images at this point will require noise filtering of fast scan-aligned scan line noise. The easiest way to do this is by running the SimplexfiltShell script on each image. SimplexfiltShell requires region masks, which are slightly different from the terrace masks you already have. You can draw your own terrace masks using MaskDraw.m.

```
MaskDraw(Img1);
```

MaskDraw requires MaskDraw.m and MaskDraw.fig and has no dependencies. Use the drop down menu to select either Striped or Normal (It doesn't matter which, the names are irrelevant), then press Draw Masks and click and drag on the image to generate a mask, much like the automatic plane subtraction from Histofit. Your goal is to select only a single flat crystalline domain. You will need one of these masks for each domain on your image. Striped Mask regions of the image will be colored red, and Normal Mask regions will be colored green. You can also remove parts from your already drawn masks by drawing a mask with Subtract selected from the drop-down menu. When you hit the 'Save' button, MaskDraw saves the masks you drew in a file called Masks.mat as a set of Boolean arrays with the same dimensions as the input image array. Loading this file into the Matlab workspace will give you a StripedMask and a NormalMask Boolean array, each one being true for the region(s)

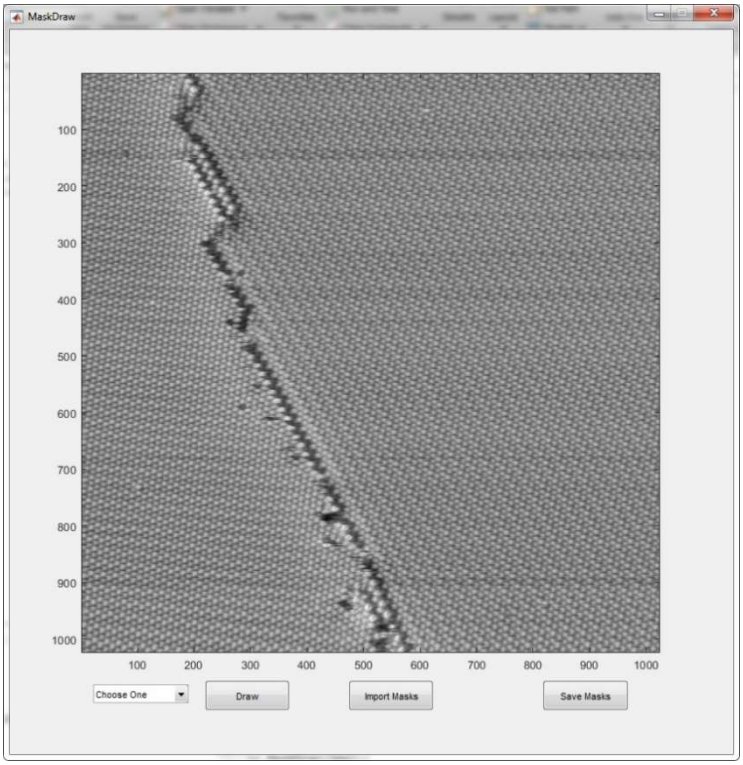


**FIG. A.3.** Screenshot of the MaskDraw GUI. Select a mask type, click "Draw", then click and drag on the image to select a region to assign to that mask type.

selected by MaskDraw. Rename the mask(s) you drew in MaskDraw to match the image you drew it on. For example, if you drew a Striped Mask and a Normal Mask on Img1 to select two regions, you could use:

```
Mask1a = StripedMask;
Mask1b = NormalMask;
```

Keep doing this until you have masks for each region of your image. If your trace and retrace images are similar enough, you can use the same masks for both Img1 and Img2. Otherwise, you'll have to use MaskDraw again on Img2. Now that you have the masks, you can use SimplexfiltShell.

```
Img1_c = SimplexfiltShell(Img1, {Mask1a, Mask1b});
```

The output of this script Img1_c (or Img2_c) is the noise-filtered image. SimplexfiltShell requires Simplexfiltshell.m and depends on psfit.m and xfilt.m. Make sure you run SimplexfiltShell on both Img1 and Img2. SimplexfiltShell handles any number of masks as long as you have at least one, and automatically removes scan line noise from the images. If you want to know more about how this software works, refer to the paper by Fogarty, et al.

D. P. Fogarty, A. L. Deering, S. Guo, Z. Wei, N. A. Kautz and S. A. Kandel, Rev. Sci. Instrum. 77 (12), 126104 - 126104-3 (2006).

SimplexfiltShell is simply a shell script that runs both psfit and xfilt in sequence. The scripts are unchanged from their published form.

While SimplexfiltShell needs one mask for each surface region, DHCT needs one mask total per image. You can compose your single region masks so these masks can be used for DHCT as well. For example, if you have two masks, you can combine them like this.

```
Mask1 = or(Mask1a, Mask1b);
```

Once you have your filtered, plane subtracted image and your composed masks, you are ready to run DHCT.

### A.3. DHCT and DHCT Multiple Passes

To run DHCT, you can use this example setup:

```
Data = DHCT(XScale, Period, SlowScanDirection, FastScanDirection, 2.88e-10*sqrt(3), Img1_c, Img2_c, Mask1, Mask2);
```

If you don't know what these variables are, refer to the setup description in Section 2. If you followed the walkthrough from section 2, you should have all of these variables in your Matlab workspace already.

DHCT has a readme file, the most current version of it as of the writing of this sentence can be found in U:/Image Analysis Software/DHCT/readme.txt, and it can also be found with the public release of DHCT on GitHub.

DHCT assumes a one-molecule-basis structure. Since the alkanethiol SAMs we are studying have a 4-molecule-basis structure, the correction will be more accurate if that is taken into account. To do this, use the second-pass DHCT script DHCT_4nn:

```
Data = DHCT_4nn(Data, XScale, Period, SlowScanDirection, FastScanDirection, 2.88e-10*sqrt(3), {Img1_c, Img2_c});
```

The first input 'Data' is the output of the first pass of DHCT. The other inputs are the same ones as in the first pass DHCT. This script uses the better correction of the first pass to identify the molecule that is exactly 4 nearest neighbor distances away from the central molecule

in each of the six nearest neighbor directions for each feature of the image. This set of molecules is guaranteed to represent the 4 molecule basis of the alkanethiol SAM for any rotation, so using them in the DHCT correction algorithm gives a more accurate correction. After identifying the 4xNN molecules, it uses the same scripts as DHCT.

The scripts required for DHCT_4nn that are not included in DHCT are DHCT_4nn, get_guess, and gather_4nn.

If you need more information about the data structure of DHCT, refer to the data structure description text file in the main DHCT folder.

### A.4. Lattice Fitting and Polynomial Lattice Corrections

c4x2_add is a script that takes the output data structure from DHCT or DHCT_4nn and does a lattice fit to the molecule positions. The script is poorly named. While the script is called c4x2_add, it actually fits a $(\sqrt{3} \times \sqrt{3})R30°$ lattice to the data. Single image lattice fitting is not implemented, you must currently use a trace-retrace image pair for lattice fitting. Workarounds for single images may be possible but are completely untested. In addition to the files that DHCT depends on, c4x2_add depends on image_offset, get_guess, cell_assign, cell_unassign, fun_image, and lattice_pair_fit. To run c4x2_add, use this example command:

```
Data_c = c4x2_add(Data, XScale, Period, SlowScanDirection,
FastScanDirection, 2.88e-10*sqrt(3), Img1_c, Img2_c, Mask1, Mask2);
```

Data is the output of DHCT or DHCT_4nn, and the other input arguments are inputs of DHCT. Determining the best fit lattice for things that aren't perfect lattices is remarkably hard, so lattice_pair_fit frequently fails without manual intervention. You should use a troubleshooting breakpoint and use the plots to tweak the lattice fitting variables. Set up the troubleshooting

breakpoint in the lattice_pair_fit file on the line indicated by the comments (currently line 77). Sf is a constant horizontal scaling factor, ys is a constant vertical scaling factor, dir is the rotation angle, and x0 and y0 are constant x and y offsets. These are initially calculated from whole-image measurements using the script get_guess. If the lattice fit isn't improving with multiple steps, you'll have to tweak those parameters yourself to get closer to the right parameters. Change them by typing new values for them into the Matlab command window, for example:

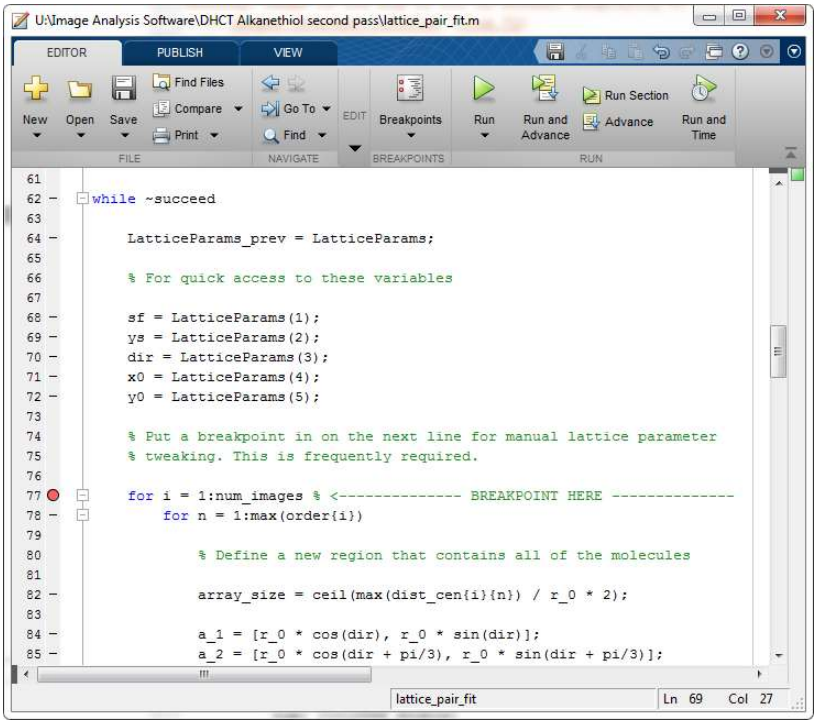


**FIG. A.4.** The location of the troubleshooting breakpoint in lattice_pair_fit.m to troubleshoot in the way described here.

```
Sf = 1.01;
```

Don't literally use that example, though! Use the figures generated by the code package to tweak the parameters to get the lattice closer to fitting. The code will not run past the breakpoint until the lattice fit stops changing, so test the starting assumptions by running past the breakpoint a few times. Blue molecules are well-fit to the lattice, and red ones are poorly fit. A good lattice fit will end with no red regions, and the colors should be continuous across each domain. The software package is very good at optimizing the lattice if it doesn't have a moiré pattern to the blue and red molecules. In Figure A.5. the left image has a noticeable moiré pattern and will not converge. The middle image had its parameters tweaked enough that it will eventually converge –

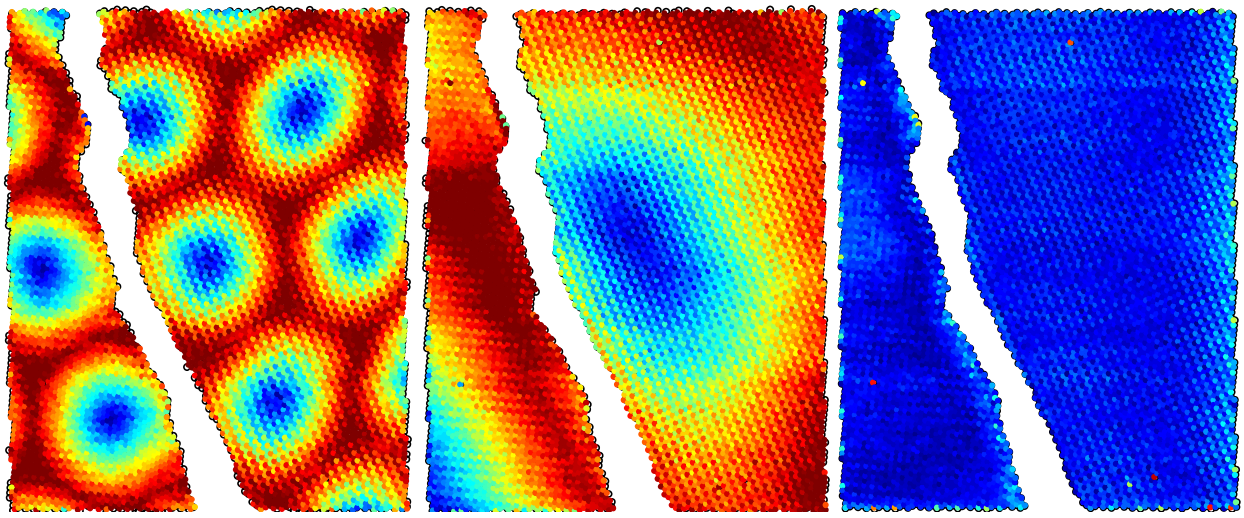

**FIG. A.5.** Plots showing the quality of the lattice fit. Left: Moiré pattern, the lattice fit will not converge. Center: No moiré pattern, this fit eventually converges. Right: Cener plot after convergence.

note that it does not feature a moiré pattern. The right image is a few iterations of the loop after the middle image, showing a successful convergence. With the breakpoint set, you can see the current value of the important fitting variables by hovering your mouse cursor over the variable names in the script. The software is very sensitive to the dir, but the guess for dir is usually pretty good. Changing x0 and y0 only matters up to the distance between molecules in nm, since the lattice is periodic. sf (vertical scale) and ys (horizontal scale) are most frequently in need of tuning.

Once you're certain the lattice will converge, let it run until the loop exits. When you have one lattice fit done correctly, run the second pass of lattice fitting that does polynomial lattice corrections.

```
Data_o = lattice_pair_fit_r(Data_c, XScale, 2.88e-10*sqrt(3),
{Img1_c, Img2_c});
```

This script depends on fun_image_r and poly_trans. This one does not need troubleshooting, but it won't work well unless your first lattice fit was good.

Now that you're done with your lattice fit, you'll want to filter the remaining data structure. This filtering step identifies lattice sites with more than one molecule assigned to them and flags them so that we can exclude them from our plots. Applying the filter is easy:

```
Data_o = data_filter(Data_o);
```

This script does not have any dependencies.

### A.5. Generating Plots: Averaged Unit Cell and Location Confidence

All of the plotting scripts depend on the most up to date averaged unit cell script, unitcell3_single. Here's an example of how to run that script:

```
[mean_cell, stdev_cell, XScale_cell, num_cells, ~, n_type,
in_cell_list, tform] = unitcell3_single(Data_o, XScale, mat_ab, 2.88e-
10*sqrt(3), imnum, region, cellpos, fp);
```

Data_o is the output of lattice_pair_fit_r after being filtered with data_filter. If you need to know how to generate this, refer to section 4. XScale and 2.88e-10*sqrt(3) are the same as from the input to DHCT. There are five new arguments here.

mat_ab: This is a 2x2 matrix that transforms the $(\sqrt{3} \times \sqrt{3})R30°$ unit cell lattice vectors into the $(2\sqrt{3} \times 3)$rect. unit cell lattice vectors. This is where the orientation of the surface unit cell is defined. One of these three matrices is guaranteed to give the correct orientation:

```
mat_ab = [-1, 2; -2, 0].';
mat_ab = [-2, 1; 0, -2].';
mat_ab = [1, 1; -2, 2].';
```

The matrix that you want is the one that returns the 4 molecule basis in the averaged unit cell. Pick one of these to test and use the plots generated by the script to check it. The easiest way

to check is by letting the script complete and confirming the average unit cell image it generates has 4 different looking molecules in it. If the molecules look exactly the same, then that likely means that the mat_ab you chose did not give the correct lattice vectors. If you have some experience in identifying SAM structures already, you may already know what orientation your cell should be. The script generates a plot relatively quickly showing the orientation of one unit cell on the image. If the orientation here is wrong, you can stop the script early using Ctrl-C and use a different mat_ab.

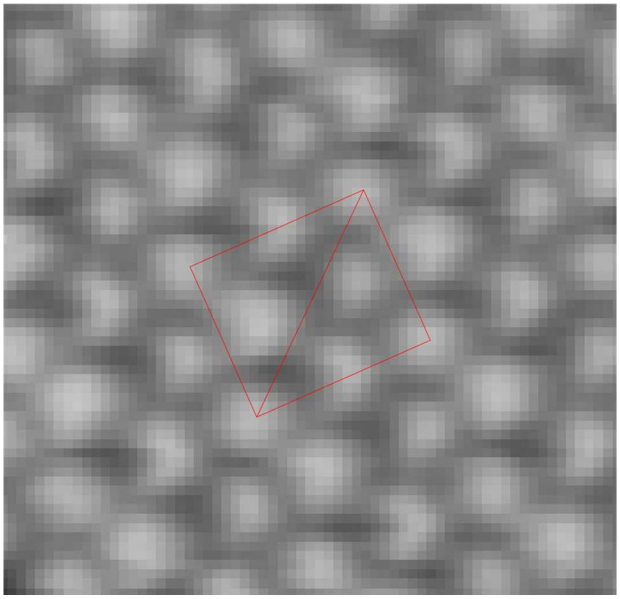

**FIG. A.6.** The first unit cell selected for averaging by unitcell3_single. If its orientation is correct, then it will generate a lattice averaged unit cell.

imnum: This selects the image that the script will generate the averaged unit cell from. 1 is the trace image, 2 is the retrace image.

region: This selects the domain in the image that the script will generate the averaged unit cell from. If the image has only one domain, region would be 1. Since the domains are assigned automatically, the easiest way to check which domain is which is to just try them all using this script. Generally, the domain with the leftmost image feature is domain 1, the domain with the next-leftmost image feature is domain 2, and so on.

cellpos: This is a string that describes where the unit cell boundaries are drawn. If cellpos is the string ‘centered’, then it will draw unit cells centered on one basis site. If cellpos is the string ‘corner’, or any other string, it will draw cells with all 4 corners on that basis site.

fp: fp is a symmetry fingerprint. fp is a number from 0 to 15 that is a binary encoding of which symmetry operators you want to apply to the unit cell. 1s place is a vertical mirror plane, 2s is a 180 degree rotation, 4s is one of the (√3 × √3)R30° unit cell lattice vectors, and 8s is the other (√3 × √3)R30° unit cell lattice vector. On your first pass of unitcell3_single, it's likely that you want a 0 here.

Here is a description of the outputs:

mean_cell: This is the main output of unitcell3_single, the lattice averaged unit cell.

stdev_cell: This is the standard deviation of each pixel of the lattice averaged unit cell.

XScale_cell: This is the size in meters of one side of a pixel in the unit cell image.

num_cells: This is the number of unit cells that were used to generate the lattice averaged cell.

**FIG. A.7.** An averaged unit cell image generated by unitcell3_single.

offset: This is a 2x1 vector that stores the (x, y) distance between the reference lattice site and the corner of the unit cell, for each unit cell. If you're using cellpos 'corner', this is always [0, 0]. This is not currently very useful, so I don't save it. This variable is replaced with a ~ in the example, which tells Matlab not to save this variable.

n_type: This is the basis type assigned to each molecule.

in_cell_list: This is a list of the molecules that were included in the mean unit cell.

tform: This is an affine transform that you apply to get the right unit cell shape if your unit cell is not a rectangle. Since the (2√3 × 3)rect. unit cell is rectangular, this should be the identity matrix.

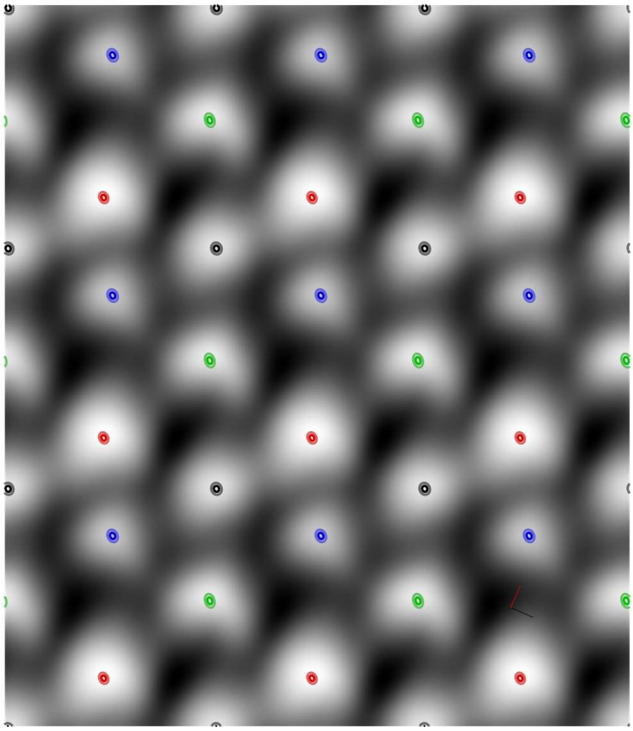

**FIG. A.8.** An averaged unit cell with molecule location confidence ellipses plotted on it by prob_contour_3.

Once you've run unitcell3_single, the other plotting scripts are available. The most common visualization I do is plot the molecule location confidence ellipses on the average unit cell. The script that does this is called prob_contour_3.

```
[stdev, meanloc] =
prob_contour_3(Data_o, XScale, XScale_cell, mat_ab, mean_cell, n_type,
SlowScanDirection, FastScanDirection, 2.88e-10*sqrt(3), imnum, region,
in_cell_list, fp);
```

Data_o, XScale, mat_ab, 2.88e-10*sqrt(3), imnum, region, and fp are inputs of unitcell3_single. SlowScanDirection and FastScanDirection are inputs from DHCT. XScale_cell, mean_cell, n_type and in_cell_list are outputs of unitcell3_single. prob_contour_3 generates the location confidence ellipse figure and has 2 outputs:

stdev: a 4x3 matrix of the major axis, minor axis and Z standard deviations of the ellipses from the 4 basis sites.

meanloc: a 4x3 matrix of the x and y coordinates (in unit cell fractions) and z coordinates (In whatever units your Z from the image is, If you're using Histofit it's nanometers) of the mean locations of the basis sites within the unit cell.

For both data sets, the correspondence of the columns with the colors from the figure from the top of the matrix down is black, then blue, then green, then red.

### A.6. Other Plot Generation Scripts

In general, displaying data well is more nuanced than the batch processing approach shown in the previous steps. The plot-generating scripts used in our work are documented here. These scripts are provided as a jumping off point for future users.

#### A.6.1. Reduced Close Packed Coordinate Frame Analysis

These scripts require running the previously described scripts up to and including prob_contour_3. This set of scripts attempts to enable comparing images to each other rather than only being able to analyze one image at a time. The script that does this comparison is called basis_remix.

```
fp = Basis_remix(meanloc_ref, meanloc);
```

Basis_remix does not have any dependencies. Its output fp is a symmetry fingerprint, an integer from 0 to 15 that describes a near-miss symmetry transformation that could cause two images of the same structure to be misaligned. meanloc is generated by running prob_contour_3 on your image. It is recommended that you get the meanloc from running prob_contur_3 and unitcell3_single with the fingerprint "0". It has the mean locations in x, y, z of the 4 basis molecules in the $(2\sqrt{3} \times 3)$rect. unit cell. meanloc_ref is the meanloc generated by running prob_contour_3

on your other image. References for C10 and C11 are provided as an example, meanloc_ref_c10.mat and meanloc_ref_c11.mat containing these references can be found in the same directory as basis_remix.m. fp is the symmetry fingerprint that minimizes the rms in-plane distance of the basis molecule locations. The goal is that if you compare the reference image using fingerprint 0 with your image using fingerprint fp, that the structure is the same so that direct comparisons can be made.

Once you have your fingerprint, you will want to generate your unit cell and probability ellipse plot again by running unitcell3_single and prob_contour_3 again using fp from Basis_remix instead of the default fingerprint of 0.

If you have generated the unit cell with fp, you can make a basis offset plot using plot_basis_offset.

```
plot_basis_offset(Data_o, XScale, mat_ab, n_type, imnum, region, fp);
```

plot_basis_offset does not have any dependencies. It generates a basis xy offset plot and a basis height bar graph that that you can compare with the plots from your reference image.

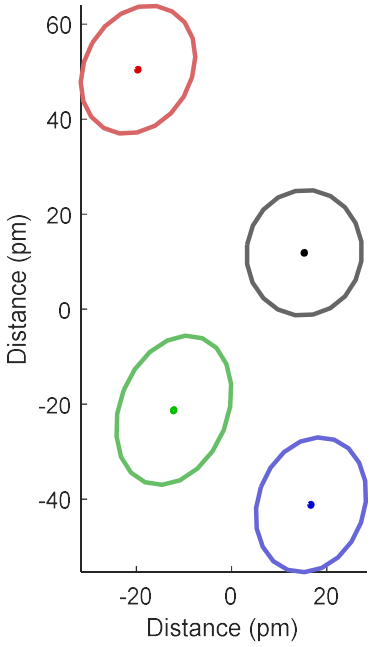


**FIG. A.9.** A reduced close-packed coordinate frame plot generated by plot_basis_offset.

### A.6.2. Aligned Image Set Movie

Image alignment requires multiple completely corrected images of the same area. Before starting this, you should do a complete image correction and lattice fitting of each of the images you would like to align (Sections 2-4 of this document), save a .mat file of the Matlab workspace for each one, and put all of those .mat files in a single folder. The .mat files should have at least the data structure Data_o,

the pre-processed images Img1_c and Img2_c, and XScale, but saving the entire workspace will work fine. Once you have a folder with the .mat files you want to analyze, navigate the current Matlab directory to that folder and run

```
get_frame_data;
```

It will create a new .mat file that scrapes only the data needed to generate the movie from the other .mat files in the folder. That file will be named Series.mat. You can generate the movie by loading that file into your Matlab workspace and running movie_setup_2

```
out = movie_setup_2(Series, 2.88e-10*sqrt(3));
```

The main output is not the data structure out, but the file Movie.avi that the script generates in the current directory. out has some data in it, but the data was mostly used for debugging. No scripts currently depend on the output of movie_setup_2. The movie file has the images aligned to one another, so that each image feature is in the same location over the whole movie. An example movie file can be found at U:/Image analysis software/Aligned image set/Movie.avi

### A.6.3. 2D Correlation Plots

Correlation plots show the 4 molecule basis of an alkanethiol SAM in a unique way. The correlation plot is a 2D histogram of molecule offsets from one molecule type. Since each basis site is different, the 4 different colors form 4

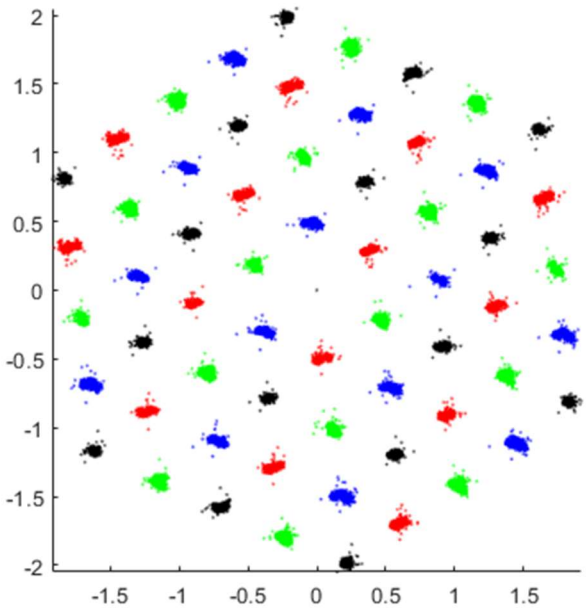


**FIG. A.10.** A 2D correlation plot generated by correlation_plot_2d

different cloud shapes in the 2D correlation plot. To generate the plot, run the following script:

```
correlation_plot_2d(Data_o, n_type, XScale);
```

It has no outputs other than the plot that it generates.

### A.6.4. Guest Molecule Analysis

If you have a bi-component SAM and want to analyze the guests separately, this section will guide you through that. First run local_height on your data.

```
Data_o = local_height(Data_o, n_type, 1, mat_ab);
```

local_height adds a new field to Data_o that contains the height difference of each feature from the average height of other nearby features in the same basis location. You should attempt to separate the guests from the host by using a height threshold on the local height.

```
guest_set = (Data_o.lh{1}.local_height >= threshold);
```

If you are unable to choose a threshold that gives a satisfying separation, you can do the separation manually using MoleculeClick.

```
guest_set = MoleculeClick(Data_o.ReshapedImage{1},
Data_o.drift_data{1}.X, Data_o.drift_data{1}.Y);
```

Both approaches give you a Boolean array, with True values on the indices where your guests are. In MoleculeClick, the true molecules are the molecules you click and turn green. You could use MoleculeClick to segment image features manually for other purposes as well.

With your guests separated, you can plot the difference of the mean location for each basis site between the guests and hosts using offset_ellipse_2.

```
xy_mean = offset_ellipse_2(Data_o.lh{1}.meanx,
Data_o.lh{1}.meany, Data_o.lh{1}.ntm, Data_o.lh{1}.guest_set, theta,
mat_ab, XScale);
```

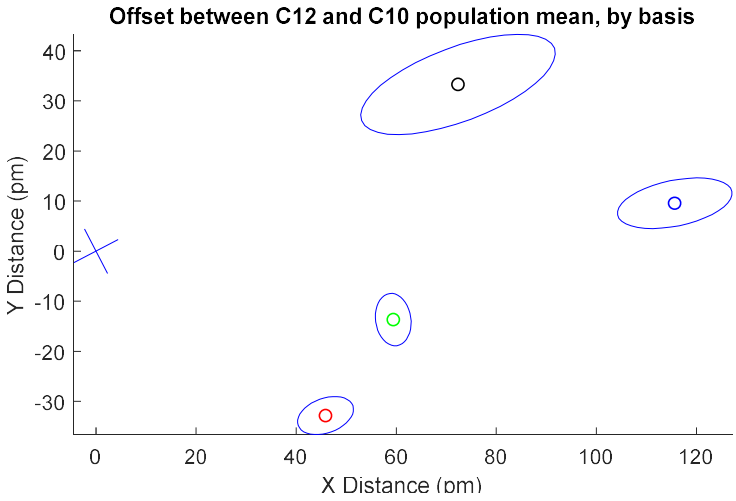


**FIG. A.11.** The mean and $\sigma_m$ of the distance between the host and guest molecules in a bi-component alkanethiol SAM, plotted by offset_ellipse_2.

All of the Data_o.lh variables are added to the data structure by local_height. Guest_set is the Boolean array we defined with a threshold or with MoleculeClick. Theta rotates the plot, so that the lattice vectors or the scan directions can be aligned with the axis direction of the plot. mat_ab and XScale are as they were defined previously.

### A.7. Two-Junction Tunneling Model

The two-junction tunneling model script we developed is slightly different from the other set of scripts described in this document. It generates STM images or corrugation surface plots from a model and a set of parameters, without requiring experimental STM images at all. The script has many parameters, so to modify them you will have to open the script. Including all of the parameters in the function arguments would be too unwieldy. Running the script varies slightly based on the operation mode selected in the script. To run it with image simulation mode selected, run the script

```
Imz = model_simulate;
```

In corrugation search mode, omit the imz.

```
model_simulate;
```

imz is the simulated STM image in image simulation mode. To access the many parameters that the simulation depends on, edit the file cell_parameters.m, which model_simulate runs to determine parameters for the model. I've tried to put the model parameters that you would consider changing into that script.

Mode: "Image" gives image simulation mode, "search" gives corrugation search mode. This defines which way you run the script as well.

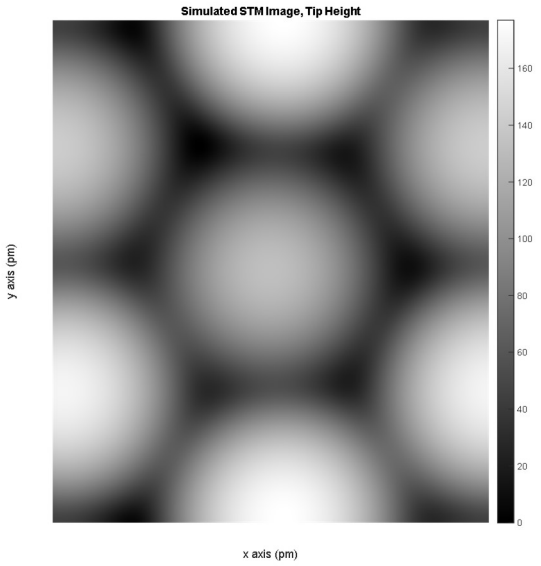


**FIG. A.12.** A simulated unit cell image generated by model_simulate.

Basis: The (x, y, z) coordinates in pm of the molecules that compose the surface you're tunneling to. The 4-molecule basis needs 4 molecules defined, but you may want to include extra molecules significantly further back to prevent the tip from breaching the surface.

Basis_methylene: Lets you tune molecular conductances independently, for considering the final methylenes along with the terminal methyl groups, for example. Should be a 1 by x vector, where x is the number of basis molecules. 0 is terminal methyl, -1 is the methylene bonded to the terminal methyl, -2 is the next methylene back, and so on.

Num_cells: Chooses the size of the imaging area by using a constant number of unit cells in each direction within the imaging area. Additional cells will be generated to avoid edge effects.

Num_neighbors: Number of neighbors to tunnel to in tunneling simulation. Higher numbers are more accurate but have diminishing returns and have a drastic effect on simulation time. We found about 2 nearest neighbor distances worth of molecules to be quite good.

Num_tips: The number of STM tips you want to tunnel from. You could use two to explore a double tip, or multiple to explore different tip shapes, or a single tip to consider the most ideal version of the model.

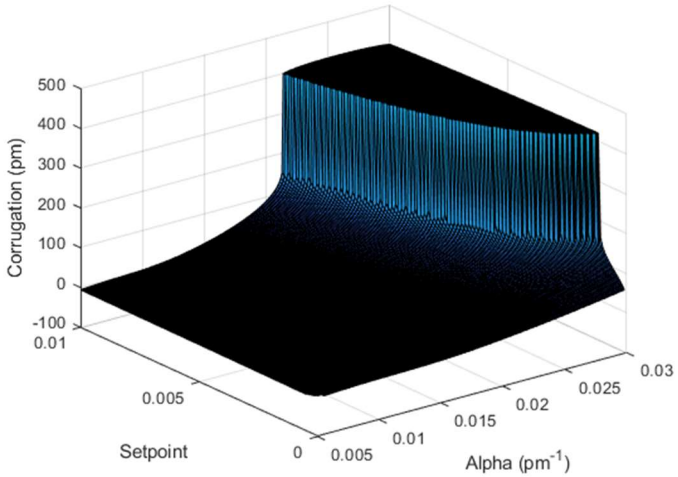


**FIG. A.13.** A corrugation search surface plot generated by the search mode of model_simulate.

Tip_x, Tip_y, Tip_z: The (x, y, z) coordinates of each of the tips in pm.

Search_radius: The distance in pm to look in for the num_neighbors features to tunnel to. Make sure this is big enough but not too big.

A_pixels, B_pixels: The size of the output image, in 8 pixel by 8 pixel chunks.

Imgmode: Only affects the image in Image mode. If set to precision, each pixel in the image has its height calculated independently. If set to speed, instead the image is segmented into 8 pixel by 8 pixel chunks, reducing the number of simulations by a factor of 64. Each chunk has its height calculated independently, then the pixel heights are estimated by scaling the image of the chunk heights by a factor of 8.

Tip_rad: Radius of each of the tip atoms, in pm. Based on testing, 0 seems to make the most sense.

Decay: Tunneling decay constant through the vacuum, in inverse pm.

Setpoint: Unitless constant that depends on the tunneling conductance, contact conductance, and tunneling decay rate through the film. 0.002 seems to work well for 1 V, 1 pA alkanethiol SAMs.

Use_phi_dependence: Very experimental, thoroughly untested option that modulates the tunneling current to depend on the angle between the surface normal and the tunneling path through the vacuum.